Interaction of Sulfite Reductase with Ferredoxin and its Relation to Enzymatic Activity

フェレドキシンと亜硫酸還元酵素間の分子間相互作用と酵素活性の関係性に関する研究

A Doctoral Thesis

Ju Yaen Kim

Department of Biology
Graduate School of Science

Laboratory of Regulation of Biological Reactions
Institute for Protein Research, Osaka University

2016

Acknowledgement

This research is a result of great circumstances of the Institute for Protein Research, Osaka University. There is a long list of people whom I deeply convey my sincere appreciation for their precious contributions and supports throughout my graduate school career.

First of all, I wish to express my deepest and sincere gratitude to my supervisor and mentor, Professor Toshiharu Hase for providing me an opportunity to do my research. His enthusiastic attitude toward the research is contagious and motivates me all the time. He enlightened me what is scientific passion and how to think about a phenomenon or experimental results from scientific knowledge. I deeply appreciate all his contributions of time, ideas, support and guidance.

Great thanks should go to Associate Professor Young-Ho Lee (Osaka University) for giving me numerous comments all the time. I also learned a lot of practical skills and theories on NMR and ITC.

In regards to the structural part of my study, I deeply appreciate to Professor Genji Kurisu (Osaka University) and Dr. Masato Nakayama. Concerning ITC part, I also deeply appreciate Professor Yuji Goto (Osaka University). Besides, I would like to thank Professor Takahisa Ikegami (Yokohama City University), Dr. Satoshi Kume (RIKEN), Mr. Misaki Kinoshita (Osaka University) for their valuable comments on my study.

I feel so blessed to have met and spent the several years with the members of Laboratory of Biological Reactions. I could learn a lot about various subjects through laboratory seminar. Especially valuable comments from Associate professor Masato Nakai and Assistant professor Yoko Kimata-Ariga improved me a lot. Dr. Shingo Kikuchi, Dr. Yukari Asakura, Natsuha Yoshida, and Widhi are always nice and kind to me.

I should give my sincere appreciation to Japan Society for the Promotion Science, JSPS, for selecting me as a research fellow (DC1) during my whole doctoral course. Their financial supports and Grant-in-Aid for Scientific Research **are extremely helpful in concentrating my research and widening my scientific knowledge.**

Finally, yet importantly, I would like to express my heartfelt thanks to my loving family for their blessings, understanding and endless love through the duration of my studies. Mingo, my little friend, brings me smile and great happiness all the time. Most of all for my loving, supportive and devoted husband, Young-Ho, I can never say thank you enough.

Ju Yaen Kim

Feburary, 2016

Table of contents

Acknowledgement……i

Table of contents……iii

Abbreviation……1

Chapter I: General introduction……..……..3

Chapter II: Structural and mutational studies of an electron transfer complex of maize sulfite reductase and ferredoxin……8

Abstract……9

Introduction……10

Materials and Methods

Site-directed mutagenesis of SiR……11

Expression of SiR in E. coli cells……11

Preparation of SiR and Fd……13

Assay of SiR activity……13

Size exclusion chromatography……16

Results

X-ray crystal structure of Fd:SiR complex……18

Mutagenesis of basic and non-charged residues of SiR located at the interface of the complex……18

Kinetic analysis of mutant SiRs with Fd……22

Fd and SiR interactions analyzed by gel filtration chromatography……...25

Discussion……30

Chapter III: Interfacial mutagenesis of sulfite reductase influences its activity and interaction with ferredoxin and substrates……..32

Abstract……33

Introduction……34

Materials and Methods

Analysis of substrate preference using Fd-dependent SiR activity assay…..…..36

Measurements of isothermal titration calorimetry……..…...36

NMR measurements……37

Results

Fd-dependent SiR activity with site-directed mutagenesis……..……..38

Interprotein affinity and binding energetics between Fd and SiRs examined by isothermal titration calorimetry……38

Residue-based solution-state NMR investigation on interprotein interactions between ferredoxin and sulfite reductase……..……39

Substrate type-dependent SiR activity monitored by NADPH oxidation…..……41

Discussion……52

Chapter IV: Noncovalent forces finely tune the electron transfer complex between ferredoxin and sulfite reductase to optimize enzymatic activity……..……54

Abstract……..……55

Introduction……56

Materials and Methods

Enzymatic activity assay……59

Isothermal titration calorimetry……59

Circular dichroism measurements……60

NMR measurements……61

Principal component analysis of chemical shift perturbation……61

Results

NaCl concentration-dependent changes in SiR activity……62

Thermodynamic investigation of interprotein interactions between Fd and SiR by isothermal titration calorimetry……63

Changes in static structures and global dynamics of SiR at various NaCl concentrations examined by far-UV CD spectroscopy……66

Residue-based investigation of NaCl concentration-dependent interprotein interactions by solution-state NMR spectroscopy……67

Discussion

Interprotein interaction-governed Fd-dependent SiR activity over the intrinsic activity power of SiR……78

Intermolecular non-covalent forces thermodynamically control Fd:SiR complex formation……79

Optimization of SiR activity by fine-tuning of the interprotein interaction with Fd under physiological conditions……81

Chapter V: General conclusion……86

References……89

Abbreviations

APS: adenosine 5'-phosphosulfate

C*c*P: cytochrome *c* peroxidase

CD: circular dichroism

CSase: cysteine synthase

CSD (or CSP): chemical shift difference (or chemical shift perturbation)

Cyt*c*: cytochrome *c*

EDTA: ethylenediaminetetraacetic acid

FAD: flavin adenine dinucleotide

Fd: ferredoxin

FNR: ferredoxin-$NADP^+$ reductase

FTR: ferredoxin thioredoxin reductase

GSH: glutathione

HSQC: heteronuclear single quantum coherence

IPTG: isopropyl-β-D-thiogalactopyranoside

ITC: isothermal titration calorimetry

k_{cat}: turnover number.

K_d: dissociation constant

K_m: Michaelis constant

MV: methyl viologen

NiR: nitrite reductase

NMR: nuclear magnetic resonance

OAS: O-acetyl serine

PC: phytochelatine

PC: plastocyanin

PCA: principal component analysis

PMSF: phenylmethylsulfonyl fluoride

SiR: sulfite reductase

ST: sulfate transporter

TCA: trichloroacetic acid

T_m: melting temperature

v_{max}: maximal velocity

$\Delta C_{p,bind}$: change in heat capacity for binding

$\Delta C_{p,global}$: change in heat capacity for global unfolding

ΔG_{bind}: Gibbs free energy for binding

ΔH_{bind}: change in enthalpy for binding

ΔH_{global}: change in enthalpy for global unfolding

ΔS_{bind}: change in entropy for binding;

Chapter I

General introduction

Introduction

In plants and microorganisms, reductive assimilation of sufate to sulfide is an essential process for the synthesis of various sulfur containing amino acids, sulfolipids, and coenzymes (1). Sulfate is first activated with ATP by ATP sulfurylase to form adenosine 5′-phosphosulfate (APS). APS reductase catalyzes a direct reduction of APS to sulfite, and resulting sulfite is further reduced to sulfide. Sulfite reductase (SiR) catalyzes this six-electron reduction of sulfite (SO_3^{2-}) to sulfide (S^{2-}) (1-4). As cysteine is synthesized from sulfide and *O*-acetylserine (OAS) in most organisms, SiR is a key enzyme for this metabolic pathway (Fig. 1-1A). SiR is a soluble monomeric protein with a molecular mass of around 65 kDa and contains a single siroheme and a [4Fe-4S] cluster as a prosthetic group (2,3,5). This enzyme receives electrons from a physiological electron donor, ferredoxin (Fd). An electron carrier protein, Fd has a [2Fe-2S] cluster, and electrons are transferred from [2Fe-2S] cluster of Fd to [4Fe-4S] cluster of SiR intermolecularly and then from [4Fe-4S] to siroheme intramolecularly (Fig. 1-1B). The stromal concentrations of SiR and Fd were estimated at 1.2 and 37 μM, respectively (6). In higher plants, SiR is located both in roots (7) and in stromal space of chloroplast (3). The root and leaf sulfite reductases are encoded by a single gene, which is expressed in both photosynthetic and non-photosynthetic tissues (8,9). In both chloroplasts and root plastids, Fd reduced by Photosystem I and ferredoxin $NADP^+$ reductase (FNR) respectively transfers electrons for SiR reduction (3,10-13).

In the case of Fd-dependent chloroplast enzymes, such as Fd:$NADP^+$ oxidoreductase (FNR), nitrite reductase (NiR) and Fd:thioredoxin reductase (FTR) including SiR form an electrostatically stabilized complex with Fd (2,14). The complex formation is essential for efficient intermolecular electron transfer between Fd and Fd-dependent enzymes. For example a complex structure of Fd:FNR has been determined by x-ray analysis. Five salt bridges are present on the interface of Fd:FNR and contribute in determination of the right orientation of two prosthetic groups, the [2Fe-2S] cluster of Fd and FAD of FNR respectively, for a productive electron transfer (11).

To understand mechanisms of the electron transfer process between Fd and SiR, 3D structure of Fd-bound SiR by x-ray crystallography gives a piece of essential information. From this high resolution crystal structure and the accumulated knowledge of Fd-dependent

chloroplast enzyme interactions, this specific interaction between SiR and Fd is considered to be crucial for efficient electron transfer (2,3). From the electron transfer complex structure several charged residues, basic residues from SiR and acidic residues from Fd, are present at the interface of SiR and Fd, indicative of an involvement of the electrostatic interaction for stabilization of the Fd:SiR complex. Various basic residues such as arginine and lysine of maize SiR located at or near the interface were neutralized to glutamine or asparagine by site-directed mutagenesis (15). Resulting mutants were analyzed by biochemical and biophysical methods such as assay of Fd and redox dye dependent enzyme activity, size exclusion chromatography and isothermal titration calorimetry. These mutational analyses of SiR based on the crystal structure allow me to get the concrete image and a new hypothesis of the electron transfer process between SiR and Fd.

Outline of thesis

In chapter II, I performed the structural analyses on the X-ray crystal structures of the Fd:SiR complex. All of the three complex structures showed similar binding modes without no appreciable structural changes. Positive electrostatic potentials surrounded binding interfaces of SiR for Fd and the central region consisted of the hydrophobic patch. Thus, complementary attractive electrostatic interactions of SiR with negatively charged Fd at interfaces was confirmed. Deletion of positive charges of SiR at interface lowered significantly SiR activity and binding ability for Fd, indicating that interfacial electrostatic interactions are crucial for the productive electron transfer complex between Fd and SiR. Meanwhile, decreases in hydrophobicity at the central regions of interfaces did not affect SiR activity and interprotein binding affinity, implying that electron may flow directly from Fd to SiR.

In chapter III, I address mutagenic effects of SiR on activity of SiR and binding ability of SiR for Fd in more detail using the mutagenic analysis in combination to SiR activity assays, isothermal titration calorimetry (ITC), and solution-state NMR spectroscopy. In-depth SiR activity assays revealed clearly that disruption of interprotein electrostatic interactions influences greatly SiR activity without no remarkable substrate preference. ITC and NMR results showed abolishment of binding ability of a SiR mutant, which positive charges at interface were neutralized, for Fd. On the one hand, SiR mutants, which hydrophobicity

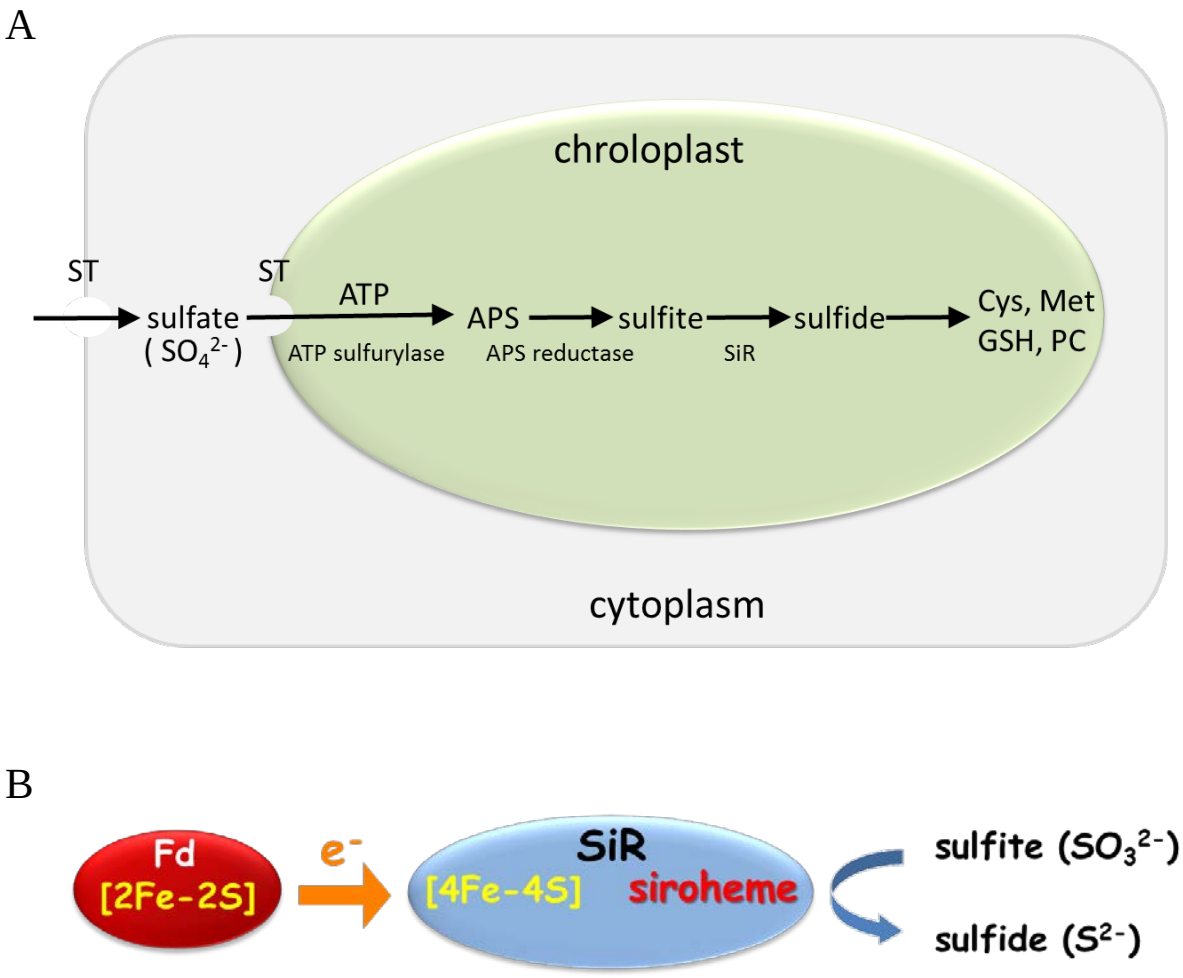

Fig. 1-1. Sulfur assimilation in plants and reduction of sulfite by SiR.

(A) Schematic representation of reductive sulfur assimilation in plants is shown. Sulfate is first activated with ATP by ATP sulfurylase to form adenosine 5'-phosphosulfate (APS). APS reductase catalyzes a direct reduction of APS to sulfite, and resulting sulfite is further reduced to sulfide. Sulfite reductase (SiR) catalyzes the reduction of sulfite to sulfide. Cysteine is synthesized from sulfide and *O*-acetylserine (ST: sulfate transporter, GSH: glutathione, PC: phytochelatine, SiR: sulfite reductase). (B) Intermolecular electron transfer from Fd via SiR for reduction of sulfite to sulfide is illustrated. An electron carrier protein, Fd has a [2Fe-2S] cluster, and electrons are transferred from [2Fe-2S] cluster of Fd to [4Fe-4S] cluster of SiR intermolecularly and then from [4Fe-4S] to siroheme intramolecularly.

decreased, showed distinct changes in activity depending on the type of substrates. ITC results showed that thermodynamic parameters of the formation of the complex were similar to those of wild type. Although binding of wild type SiR and mutant SiR showed common interfaces on ^{15}N-labeled Fd, binding modes were different to some extent based on the distinct chemical shift difference and direction of NMR peak shifts. Taken together, intermolecular electrostatic interactions are critical for SiR activity with making productive electron transfer complexes. I suggest that hydrophobic interactions play an important role for substrate preference using subtle binding modes.

In chapter IV, I set out to understand non-covalent interactions between Fd and SiR and their relations to SiR activity at the various concentration of NaCl as a physiological perturbation. Fd-dependent SiR activity assays and Michaelis-Menten kinetics revealed a bell-shaped activity curve with a maximum around 40-70 mM NaCl and a reverse bell-shaped dependence of affinity. Meanwhile, intrinsic SiR activity, as measured in a methyl viologen-dependent assay, exhibited saturation above 100 mM NaCl. Thus, two assays suggested that interprotein interaction is crucial in controlling Fd-dependent SiR activity.

ITC analyses showed the monotonic increase in the dissociation constant on increasing NaCl concentrations, distinguished from the biphasic change in the Michaelis constant. The results further revealed that Fd:SiR complex formation and interprotein affinity were thermodynamically adjusted by both enthalpy and entropy through electrostatic and non-electrostatic interactions. A residue-based NMR investigation on addition of SiR to ^{15}N-labeled Fd also demonstrated that a combination of both non-covalent forces stabilized the complex with similar interfaces and modulated binding affinity and mode depending on NaCl concentrations. I suggested that non-electrostatic forces are also essential for complex formation and modulation and that a complex configuration optimized for maximum enzymatic activity near physiological conditions is achieved by structural rearrangement through controlled non-covalent interprotein interactions.

Finally, in chapter V, I summarize of my research described in chapter II, III, and IV with future perspectives.

Chapter II

Structural and mutational studies of an electron transfer complex of maize sulfite reductase and ferredoxin

Abstract

The structure of the complex of maize sulfite reductase (SiR) and ferredoxin (Fd) has been determined by X-ray crystallography. Co-crystals of the two proteins prepared under different conditions were used for the diffraction analysis and three possible structures of the complex were dissolved. Although topological relationship of SiR and Fd varied in each of the structures, common characteristics were found both in the electrostatic intermolecular interactions and the positional arrangements of the redox centers; several negative residues of Fd are close to distinctive areas within the positive electrostatic surface of SiR, and positions of [2Fe-2S] cluster of Fd and [4Fe-4S] cluster of SiR are in a close proximity with the shortest distance around 12 Å. This indicated that the three complexes would be functionally competent.

Mutational analysis of a total of seven basic residues of SiR distributed widely at the interfaces of the three structures showed their importance for Fd-dependent SiR activity and contribution for a strong affinity of SiR with Fd. Based on these combined results, I suggest that the electron transfer complex of SiR and Fd could be formed though multi-intermolecular interaction processes. This implication is discussed in terms of the multi-functionality of Fd in various redox metabolisms.

Introduction

Intermolecular interactions among biomolecules and/or small ligands are one of the most fundamental processes in life phenomena such as electron transfer, signal transduction, and protein homeostasis (16-21). Intermolecular interactions proceed to a stable state in an energetically favorable way. These intermolecular forces largely comprise of the two terms, electrostatic (i.e., charge-charge) and hydrophobic (i.e., van der Waals) interactions (22). Surfaces of folded active proteins are generally consist of both charged/polar hydrophilic and apolar hydrophobic residues (23). Proteins have evolved to use these physicochemical properties adequately for efficient functions in soluble states (24).

A lot of redox proteins have shown biased local electrostatic patches of positive (i.e., basic) or negative (i.e., acidic) residues on their binding surfaces for partner molecules (11,25-39). Cytochrome *c* uses the highly positive electrostatic patches to interact with acidic residues of the subunit II of cytochrome *c* oxidase for electron transfer (31). Similarly, positive residues of cytochrome *f* interact with negative residues of plastocyanin (29). In chloroplast, ferredoxin (Fd) which possesses the clusters of acidic regions acts as a multiple electron donor for various redox proteins. A lot of biochemical and biophysical studies have suggested that various Fd-dependent enzymes such as nitrite reductase (NiR), sulfite reductase (SiR), and ferredoxin-$NADP^+$ reductase (FNR) mainly interact with Fd using their positive residues on surfaces (2-4,11,13,14).

SiR is an important enzyme for sulfur assimilation and reduces sulfite to sulfide using six electrons transferred from Fd which is a physiological electron donor (2-4). Electrons are transferred from a [2Fe-2S] cluster of Fd to a [4Fe-4S] cluster of SiR intermolecularly and then flow from a [4Fe-4S] to siroheme intramolecularly. Linked sequential catalytic reactions with other enzymes produce amino acid residues such as methionine and cysteine using sulfide.

Up to now, limited information on the contribution of Fd:SiR interactions to SiR activity (3,4,40). Although intermolecular electrostatic interactions have been shown to play a key role in forming the Fd:SiR complex, much still remains to be elucidated for obtaining detailed intermolecular interactions in the complex for SiR activity and for a pathway of electron transfer. In this regard, in order to address these issues, I performed that in-depth analyses on the crystal structure of the Fd:SiR complex and characterized orientation of two proteins in the complex, the distance between two iron-sulfur centers, physicochemical features of interfaces.

Materials and Methods

Site-directed mutagenesis of SiR

We used an expression plasmid of maize SiR previously constructed for site-directed mutagenesis in this study (3,41). The mature region of SiR cDNA was inserted into pTrc99A expression vector together with *E. coli* Cys G gene, which is necessary for siroheme biosynthesis. Amino acid substitutions targeted in this study, K66Q, R111Q, R114Q, R111Q/R114Q, R117Q, R324Q, K582Q, K584Q, K582Q/K584Q, A493G, L499G, P501G, L502A, A503G, Q504G, P541G and each mutation was introduced by use of quick change XL site-directed mutagenesis kit (Stratagene, USA). The list of mutants generated in this study and synthetic oligonucleotides used for the mutagenesis is shown in Table 2-1.

Expression of SiR in E. coli cells

E. coli JM109 cells were transformed with the expression vector carrying mutant SiR cDNA. Each mutant including wild type was grown overnight at 37 ºC in Lurial-Bertani

Table 2-1. A list of PCR primers used for mutagenesis of maize SiR.

*Mutant	Oligonucleotide
K66Q	5’TCTGAAGTTAAGCGAAGCCAGGTTGAGATAATCAAGGAA3’
	3’AGACTTCAATTCGCTTCGGTCCAACTCTATTAGTTCCTT5’
R111Q	5’GCTACCAGCAAACTGACCAGGATGTCCGTGGGCAGAAG3’
	3’CGATGGTCGTTTGACTGGTCCTACAGGCACCCGTCTTC5’
R114Q	5’CTGACCGAGATGTCCAGGGGCAGAAGAATTAC3’
	3’GACTGGCTCTACAGGTCCCCGTCTTCTTAATG5’
R111Q/R114Q	5’AGCTACCAGCAAACTGACCAGGATGTCCAGGGGCAGAAGAATTACTCG3’
	3’TCGATGGTCGTTTGACTGGTCCTACAGGTCCCCGTCTTCTTAATGAGC5’
K117Q	5’CGAGATGTCCGTGGGCAGCAGAATTACTCGTTTATGCTC3’
	3’GCTCTACAGGCACCCGTCGTCTTAATGAGCAAATACGAG5’
R324Q	5’GGCATGGGAAGGACACACCAGGTGGAAACTACATTCCCT3’
	3’CCGTACCCTTCCTGTGTGGTCCACCTTTGATGTAAGGGA5’

K582Q	5’CATTTATGGACCAAGTGAAGCTTGATGACATCGAG3’
	3’GTAAATACCTGGTTCACTTCGAACTACTGTAGCTC5’
K584Q	5’CATTTATGGACAAGGTGCAGCTTGATGACATCGAG3’
	3’GTAAATACCTGTTCCACGTCGAACTACTGTAGCTC5’
K582Q/K584Q	5’CGCTAGCAGAATCATTTATGGACCAAGTGCAGCTTGATGACATCGAGAAGG3’
	3’GCGATCGTCTTAGTAAATACCTGGTTCACGTCGAACTACTGTAGCTCTTCC5’

**Mutant	Oligonucleotide
A493G	5’CCTTGAATTTAACTGCCATGGGTTGCCCTGCCTTGCCACTGTGC3’
	3’GGAACTTAAATTGACGGTACCCAACGGGACGGAACGGTGACACG5’
L499G	5’GCATGCCCTGCCTTGCCACGTTGCCCTTTGGCACAAAC3’
	3’CGTACGGGACGGAACGGTGCAACGGGAAACCGTGTTTG5’
P501G	5’CCTGCCTTGCCACTGTGCCGTTTGGCACAAACAGAAGC3’
	3’GGACGGAACGGTGACACGGCAAACCGTGTTTGTCTTCG5’
L502A	5’GCCTTGCCACTGTGCCCTTCTGCACAAACAGAAGCTGAA3’
	3’CGGAACGGTGACACGGGAAGACGTGTTTGTCTTCGACTT5’
A503G	5’CCTTGCCACTGTGCCCTTTGGGTCAAACAGAAGCTGAACGG3’
	3’GGAACGGTGACACGGGAAACCCAGTTTGTCTTCGACTTGCC5’
Q504G	5’CCACTGTGCCCTTTGGCACGTACAGAAGCTGAACGGGGG3’
	3’GGTGACACGGGAAACCGTGCATGTCTTCGACTTGCCCCC5’
P541G	5’GGATAACTGGATGCCCTGATGGATGCGCTAGACC3’
	3’CCTATTGACCTACGGGACTACCTACGCGATCTGG5’

*electrostatic mutant, **non electrostatic mutant

medium containing 50 μg/ml ampicillin. The seed culture was inoculated to 8 L of the same medium. The cells were grown with vigorous aeration at 37 ºC for 3 hours. Then culture temperature was lowered to 27 ºC and isopropyl-β-D-thiogalactopyranoside (IPTG) was added to a final concentration of 0.5 mM. After further cultivation for overnight, the cells were collected by centrifugation at 6,000 rpm for 10 min and stored at -30 ºC. About 40 g of bacterial cells were obtained in each culture (per 8 L).

Preparation of SiR and Fd

The frozen cells were suspended in 50 mM Tris-HCl, pH 7.5 containing 150 mM NaCl, 1 mM $MgCl_2$, 1 mM EDTA and 0.1% β-mercaptoethanol. After adding PMSF at a final concentration of 0.5 mM, the cell suspensions were disrupted by sonication on ice. The broken cell suspension was centrifuged at 10,000 rpm for 15 min and supernatant was passed through DE-52 resin. SiR was recovered from the flow-through fraction and fractionated by salting out with ammonium sulfate concentrations between 35% and 60%. The precipitated proteins were dialyzed against 25 mM Tris-HCl buffer (pH 7.5) overnight at 4 ºC. The dialyzed proteins were applied on a DEAE-Toyopearl column and chromatographed with a linear gradient with NaCl from 0 to 200 mM in 50 mM Tris-HCl buffer (pH 7.5). SiR fraction was added with ammonium sulfate to a final concentration of 30%, applied on a phenylsepharose column, and eluted with a reverse linear gradient of ammonium sulfate from 40% to 0% in 50 mM Tris-HCl buffer (pH 7.5). The purification procedure is shown in Fig. 2-1.

Wild type maize Fd was expressed in *E. coli* strain JM109 cells and purified as described previously (42). The detailed purification procedure is show in Fig. 2-2. ^{15}N-labeled Fds were obtained by culturing the bacterial cells in an M9 minimum medium containing $^{15}NH_4Cl$ as the sole nitrogen source.

Assay of SiR activity

Fd- and methyl viologen (MV)- dependent activity of wild type and mutant SiRs was assayed with a reconstituted electron transfer system by converting sulfide to cysteine with cysteine synthase (CSase) shown in Fig. 2-3. The reaction mixture included Fd (0-40 μM) or methyl viologen (1 mM), SiR (200 nM), sodium sulfite (2 mM), O-acetyl serine (10 mM) and CSase (0.4 U) in 50 mM Tris-HCl buffer (pH 7.5) containing 100 mM NaCl at 30 °C. Sulfite reduction was initiated by adding $Na_2S_2O_4$ which reduces Fd and sulfide produced was sequentially converted to cysteine by coupling with CSase in the presence of OAS. Reaction was stopped by adding 25% of trichloroacetic acid (TCA) to a final concentration of 20%. After heating at 95 °C for 10 min, 450 μl ethanol was added to the ninhydrine solution. The solution was centrifuged at 15,000 rpm for 3 min to remove insoluble materials, 150 μl acetic acid, and 150 μl acid-ninhydrine reagent was added to the supernatant (150 μl). After production of cysteine was monitored by increases in absorption intensity at 546 nm. MV was used instead

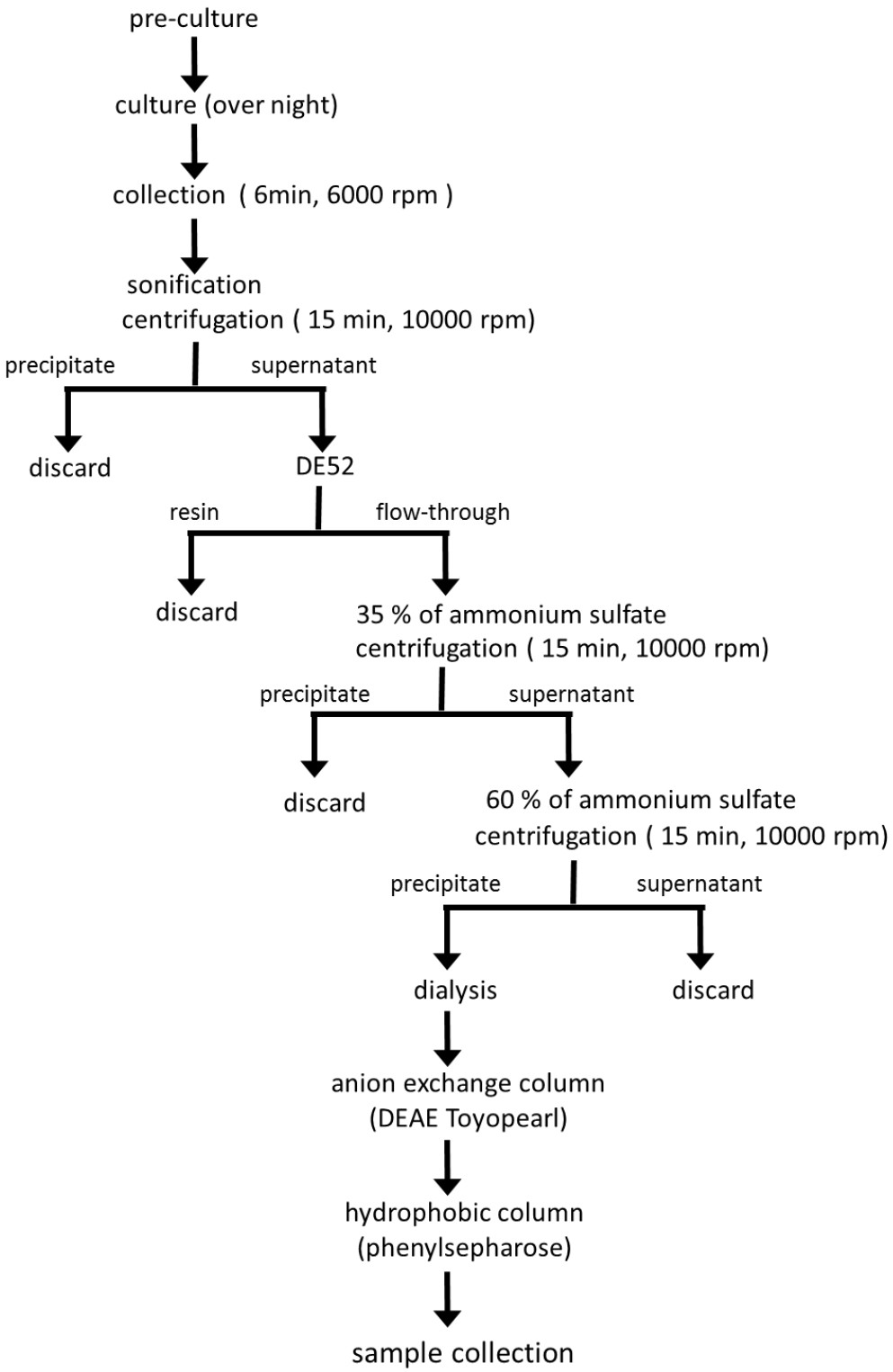

Fig. 2-1. Schematic representation of the purification procedure of wild type and mutant SiRs.

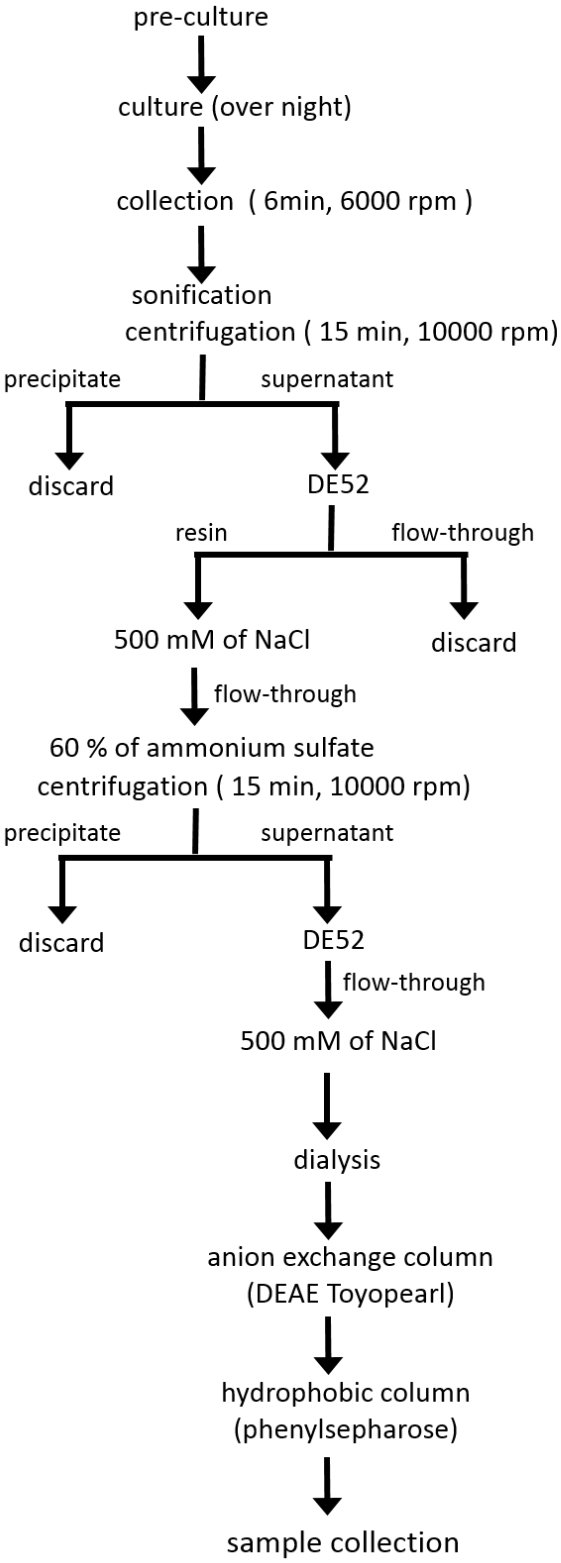

Fig. 2-2. Schematic representation of the purification procedure of Fd.

of Fd for confirming activity of SiR mutants driven by a redox dye. Kinetic measurements were conducted by changing the concentration of Fd from 0 to 40 μM. Measurements were repeated at least three times for each protein sample.

Size exclusion chromatography

Complex formation of Fd with wild type and mutant SiRs was analyzed by gel filtration chromatography using an ÄKTA purifier (Amersham Pharmacia Biotech, USA). A mixture of Fd and SiR was loaded on a Superdex 75 gel filtration column (PC3.2/30; Amersham Pharmacia Biotech, USA) pre-equilibrated by 50 mM Tris-HCl buffer (pH 7.5) containing 25 mM NaCl and eluted using the same buffer (for (pre-)equilibration) at a flow rate of 0.5 ml/min at 25 °C. Fd and SiR were monitored by the absorbance at 330 nm derived from the prosthetic groups of the proteins.

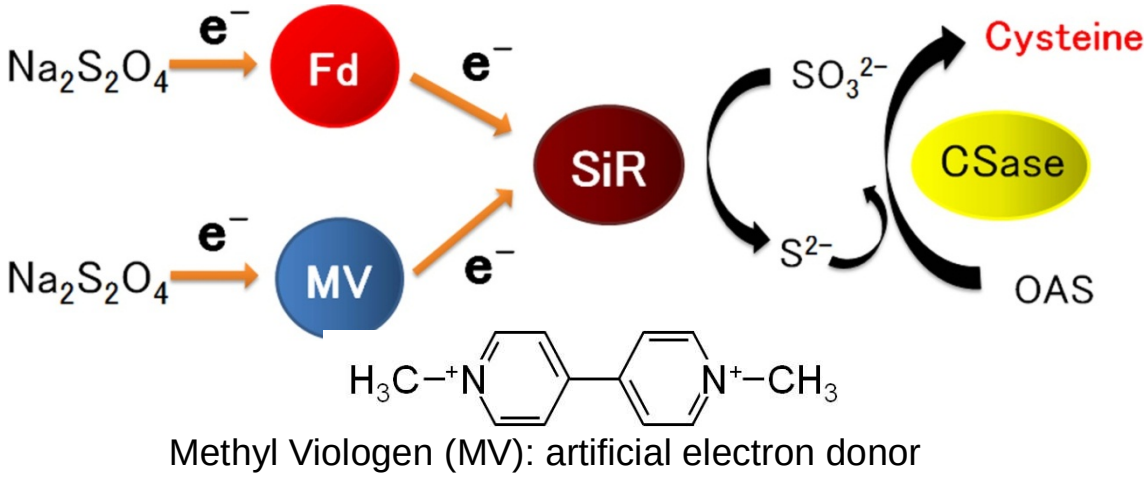

Fig. 2-3. Scheme of assay for Fd- and MV-dependent sulfite reduction by SiR.

Two SiR activity assays, which are distinguished by the type of an electron donor, Fd or methyl viologen (MV), are schematically represented. Sulfide (S^{2-}) produced by SiR is converted to cysteine in the presence of an excess amount of o-acetyl serine (OAS) and cysteine synthase (CSase). The production of cysteine is monitored by increases in absorbance at 546 nm resulting with treatment of acid-ninhydrin reagent. The chemical structure of MV is also shown.

Results

X-ray crystal structure of Fd:SiR complex

I utilized previously obtained x-ray crystal structure of Fd:SiR complex for analysis (crystallization by Dr. Nakayama Masato (Osaka University) and Prof. Genji Kurisu (Osaka University)). Two different types of crystals were prepared from a mixture of Fd and SiR co-existed with one to one molar ratio. In a unit cell of the crystal 1, one Fd molecule and two SiR molecules were observed. In crystal 2, there were two Fd molecules and four SiR molecules. Based on the relative spatial arrangement of Fd and SiR, three possible complex structures of Fd and SiR (Complex AC, Complex BF, and Complex AE) were found in the crystals (Fig. 2-4). In all three complexes the distance between the two iron-sulfur clusters, a [2Fe-2S] cluster from Fd and a [4Fe-4S] cluster from SiR, was about 12 ~13 Å and the two redox clusters were facing each other (Fig. 2-5). These indicate that intermolecular electron transfers are likely to occur in all complexes. However relative orientations of the two proteins in individual Fd-SiR complexes are different meaning that amino acid residues involved in intermolecular interactions at each complex would be distinct. In order to examine interacting residues in each complex, I introduced the results previously obtained by solution-state NMR spectroscopy (4), which provides information on important residues of Fd for intermolecular interactions with SiR. The residues obtained from NMR data were well located in intermolecular surfaces in all complexes in Fig. 2-6.

Mutagenesis of basic and non-charged residues of SiR located at the interface of the complex

Three structures of the complex of SiR and Fd determined in this study gave important pieces of information on the physicochemical characteristics of the protein-protein interaction. The surface of SiR at the interface was surrounded by a wide area of positive electrostatic potential and the center region of the interface, where the [4Fe-4S] cluster was located, was covered by a small non-charged area as shown in Fig. 2-7. In order to examine whether restricted area or all of the positively charged surface of SiR is crucial for an efficient electron acceptance from Fd, I performed mutagenic investigation in combination to enzyme activity assay.

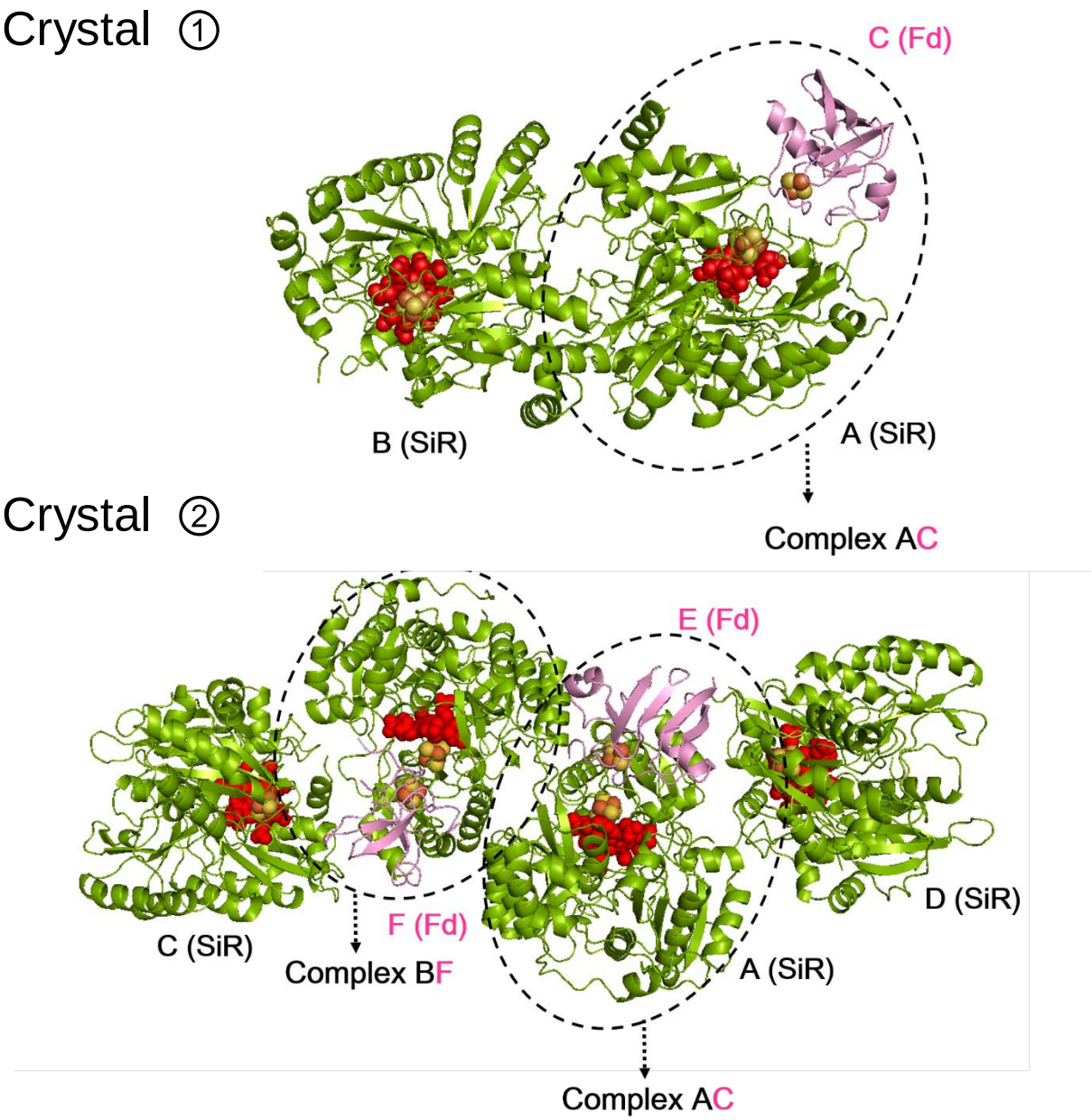

Fig. 2-4. Three dimensional structure of Fd and SiR.

Fd and SiR in crystal 1 (upper) and crystal 2 (lower) are shown in pink and green, respectively. The [2Fe-2S] cluster in Fd and the [4Fe-4S] cluster and siroheme in SiR are also colored with the space-filling model. Each Fd:SiR complex is highlighted with broken circles and labeled.

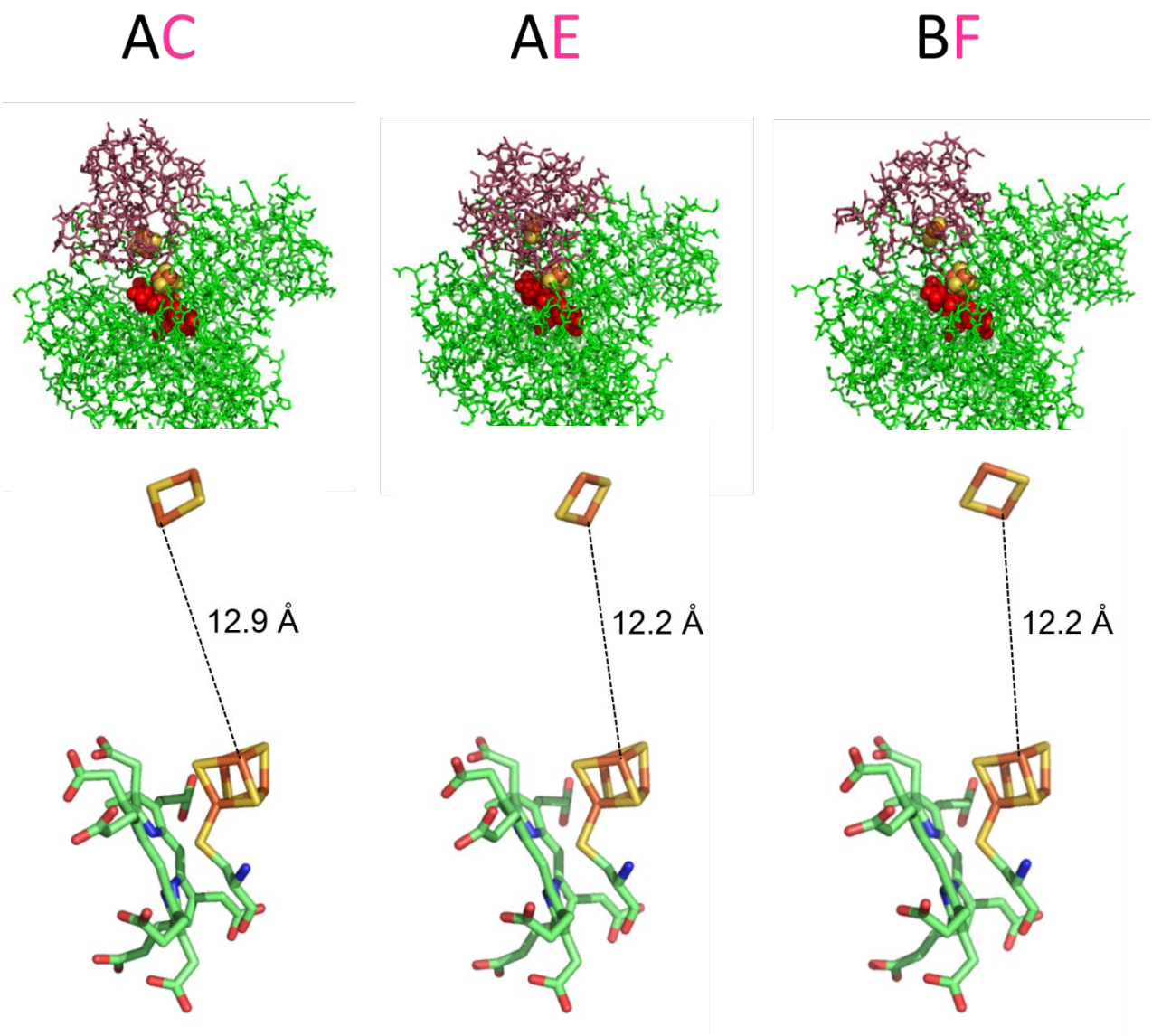

Fig. 2-5. Structures of three possible Fd:SiR complexes.

Three Fd:SiR complexes (complex AC, BF, and AE) in crystals 1 and 2 are shown. Fd and SiR are colored in magenta and green, respectively (upper). Redox centers are displayed with the color code and space filling model. (Lower) The distance between the two iron-sulfur clusters, a [2Fe-2S] cluster from Fd and a [4Fe-4S] cluster from SiR, is guided by the dotted line and shown in angstrom (12 ~13 Å). Siroheme next to the [4Fe-4S] cluster is shown with the stick model.

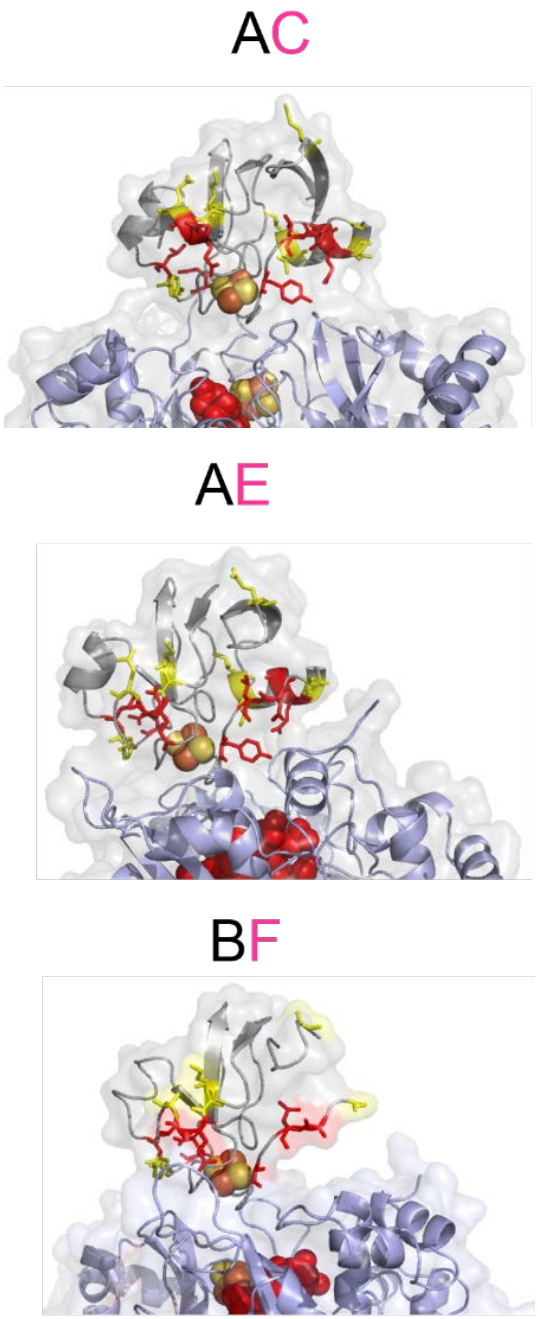

Fig. 2-6. Mapping of NMR results onto Fd in the three possible complex structures. Chemical shift difference (CSD) of Fd (4) on binding with SiR was mapped on to each Fd in three complexes (AC, BF, and AE). Residues with the high (CSD > 0.08) and relatively high CSD values (0.08 > CSD > 0.06) are shown with their side chains and colored in red and yellow, respectively.

Seven basic residues of SiR, Lys66, Arg111, Arg114, Lys117, Arg324, Lys582, and Lys584, which are distributed at the various region of the interface of the complex, were substituted point by point to Gln and mutagenic effects on the activity of SiR were examined (Fig. 2-7A). The mutant SiRs were purified and showed absorption spectra comparable with a wild type enzyme (Fig. 2-8), indicating that mutation did not affect structures of redox centers. All mutants showed a remarkably lowered activity when Fd was used as an electron donor, although mutations at Lys66 and Arg114 retained the activity to a certain extent. In a sharp contrast, no such significant decrease was observed in the MV-dependent activity. This data clearly showed that the almost all of the basic residues is attributed to an efficient electron acceptance from reduced Fd, but not for enzyme activity itself.

Next, seven non-charged residues with a large side chains at the center region of the interface were substituted to glycine or alanine (Fig. 2-7) and resulting mutants were assayed as above (Fig. 2-7B). The results revealed that the mutations gave no significant effects on either Fd-dependent or MV-dependent activity, indicating that the non-charged residues located between the redox centers of the two proteins is dispensable at least with a level of single residue mutation.

Kinetic analysis of mutant SiRs with Fd

Fd-dependent activity of wild type and mutant SiRs was kinetically assessed by measuring formation of cysteine by CSase from sulfide produced by SiR. SiR mutants, whose basic residues of Lys and Arg, located at or near the interaction site for Fd, were neutralized to Gln, were characterized for evaluating effects of these positive charges on Fd-dependent activity (Fig. 2-9).

In order to investigate the integrity of mutations for catalytic reaction capability, MV-dependent activity of SiRs was also assayed with comparison of Fd-dependent activity. Activity of SiRs at a 3-min reaction time was plotted against Fd concentrations ranged from 0 to 40 μM in the assay mixture (Fig. 2-9A and 2-9C). All the mutants showed MV-dependent activity comparable to the wild type whereas Fd-dependent activity of the mutants was lowered in all mutant SiRs.

The representative activity results of mutants are shown in Fig. 2-9A and 2-9C. The double mutants, R111Q/R114Q and K582Q/K584Q, and the single mutants, R111Q, R117Q,

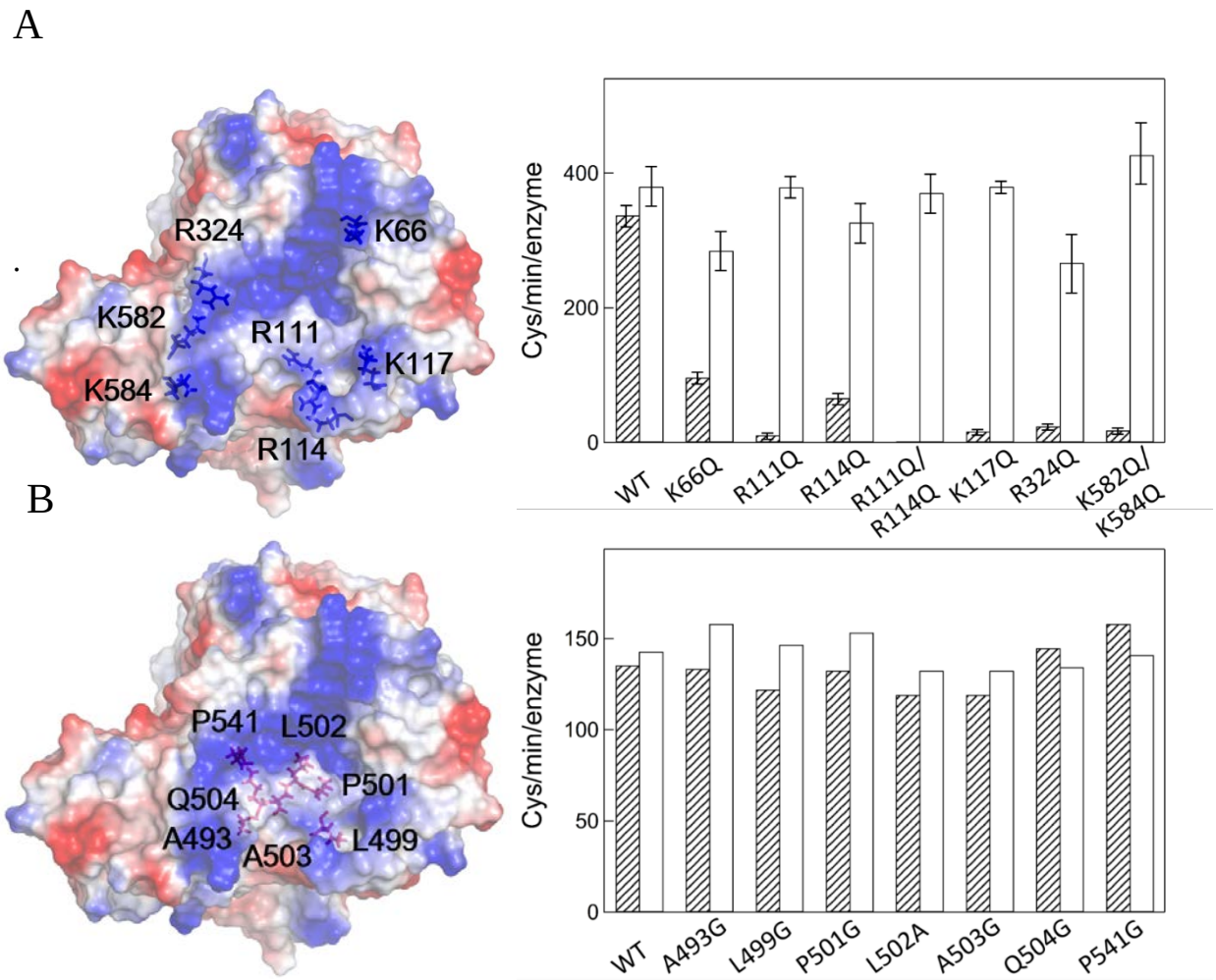

Fig. 2-7. Location of mutation and activity of wild type and mutant SiRs.

(A, B) Residues subjected to electrostatic (A) and non-electrostatic mutation (B) are shown on the crystal structure of SiR (left) and activity of wild type and mutant SiRs obtained by Fd- (hatched bar) and MV-dependent SiR activity assay (open bar) is also shown (right).

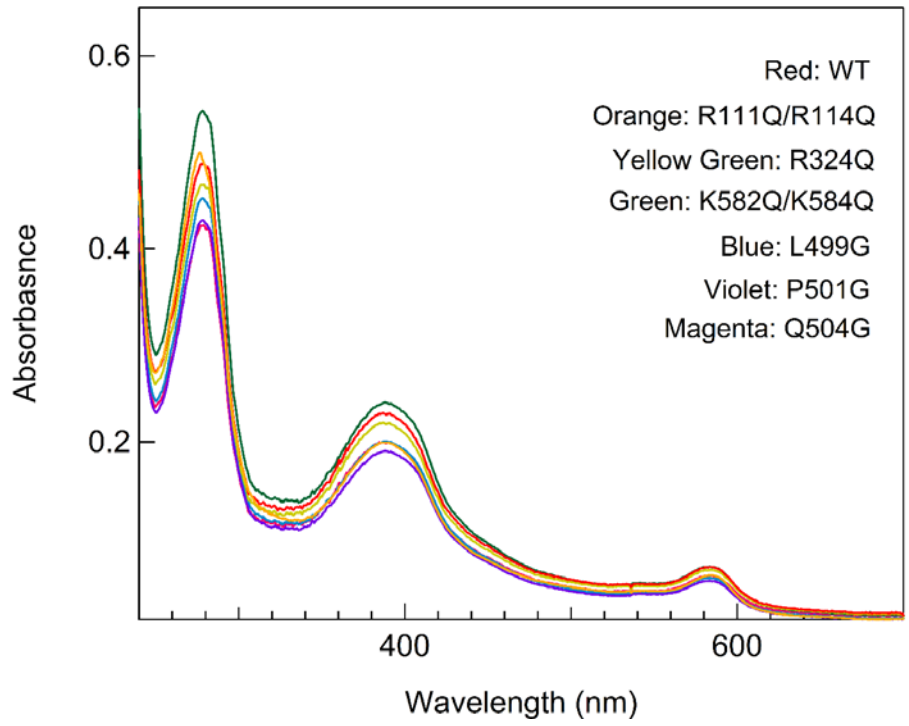

Fig 2-8. Absorption spectra of wild type and mutant SiRs.

UV-vis spectra of wild type and mutant SiRs are shown with color codes.

and R324, exhibited considerably low activity (Fig. 2-9A and 2-9C). On the other hand, R114Q, K582Q, and K584Q decreased activity to some extent compared to wild type. Extents of the activity drop varied among the mutant SiRs, indicative of variable contributions of the basic residues of SiR to the interaction with Fd.

Fd and SiR interactions analyzed by gel filtration chromatography

Complex formation of Fd with wild type and mutant SiR was investigated using size exclusion chromatography. Fd and SiR were separately loaded on a column of Superdex 75 and it was observed that SiR was eluted earlier than Fd as a single peak (Fig. 2-10A). When a mixture of Fd and wild type SiR in a molar ratio of 1:1 was loaded, a single peak corresponding to Fd:SiR complex was detected at a retention time earlier than that of free SiR, (Fig. 2-10B). Adding more Fd excess to the 1:1 mixture, the peak area of the free Fd became larger, further confirming that the earlier peak is due to Fd:SiR complex formed by a saturation of bound Fd.

In order to examine roles of basic residues on the interfaces of SiR for Fd binding, a series of SiR mutants, whose positive charges were neutralized, were respectively loaded with Fd. As indicated in Fig. 2-10C, a mixture of R111Q and Fd showed the two separated peaks corresponding to the elution peaks of free SiR and Fd, indicating no complex formation. Further addition of Fd becomes only the peak of Fd greater. However, mutants in the interface part, K582Q, K584Q, and K582Q/K584Q displayed complex behaviors (Fig. 2-10D). The peak positions of K582Q/K584Q:Fd mixture were consistent with those of free proteins, indicative of no interaction between the two proteins. The elution time of Fd:SiR mutant complex was subtly different in the order K584Q > K582Q > K582Q/K584Q, which coincides with the order of decreases in activity (Fig. 2-9C).

The other mutants on binding interfaces, R111Q/R114, R117Q, and R324Q not capable of carrying significant activity, exhibited similar pattern of free Fd and SiR (Fig. 2-11A, B and C). A mixture of Fd and K66Q, not located on the interface, and used for a control. Unexpectedly, however, elution time close to those of Fd:SiR was observed, suggesting weak Fd:SiR complex formation, which would be also involved in residual activity. From the previous research addition of 100 mM NaCl to the elution buffer (2), Fd and SiR in the mixture were separately eluted, indicating that Fd and SiR complexation was mainly by electrostatic interaction.

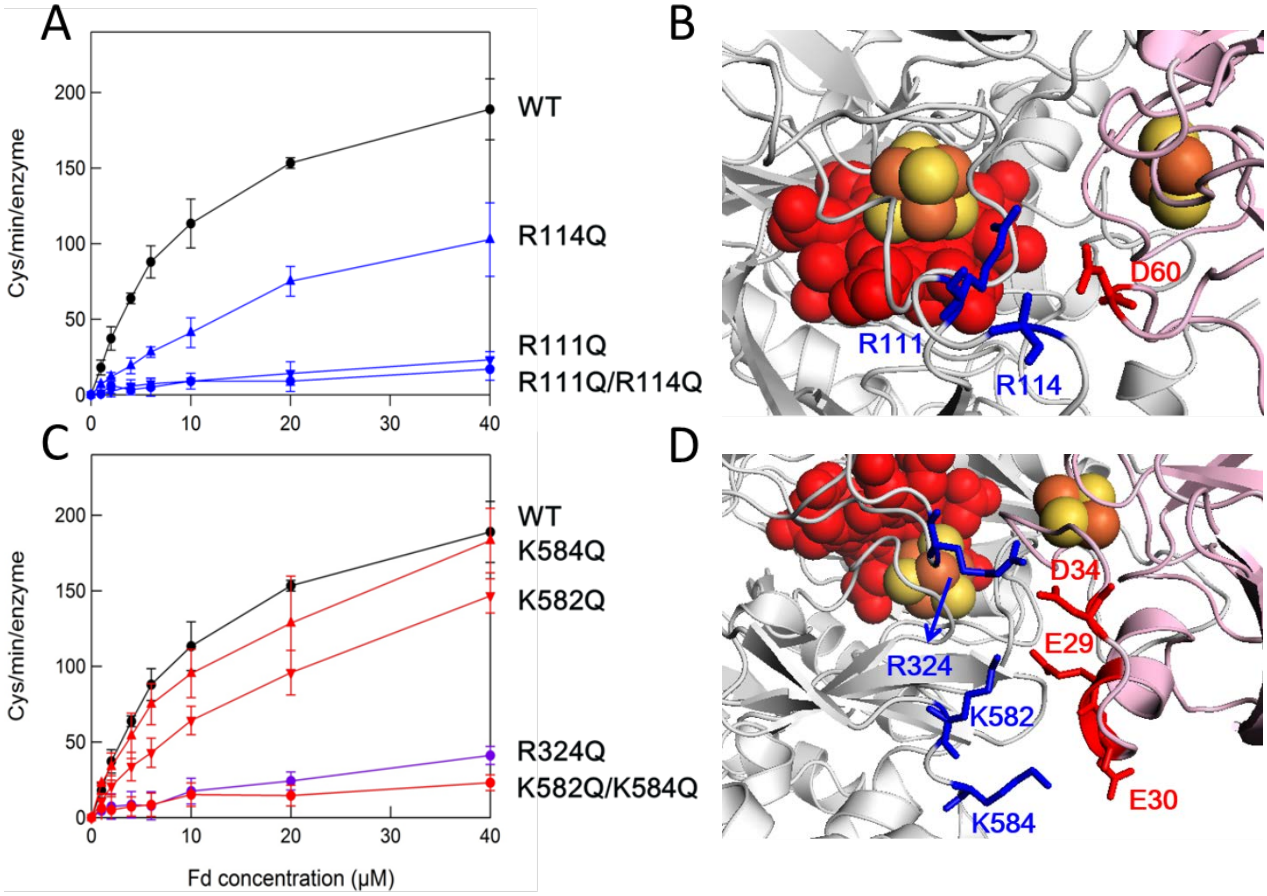

Fig. 2-9. Kinetics of Fd-dependent activity of SiR mutants.

(A, C) Fd-dependent activity of mutant SiRs was plotted against the concentration of Fd. (B, D) Representation of side chains at interface. Basic residues in SiR and acidic residues in Fd are represented. Clusters of red spheres indicate siroheme and the two iron-sulfur clusters are also shown with the space-filling model.

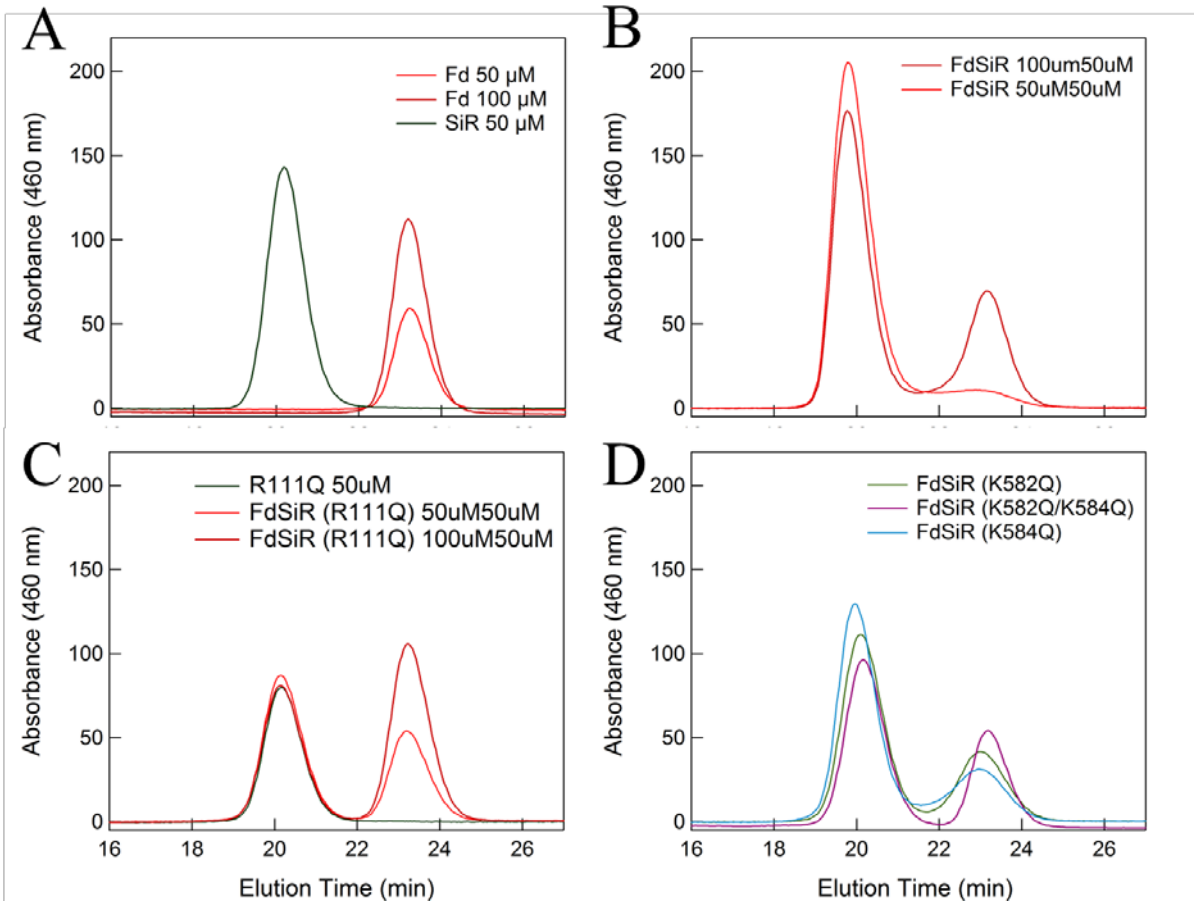

Fig. 2-10. Size exclusion chromatographic analysis on the interaction between Fd and SiR. (A-D) Elution profiles of solutions containing Fd or SiR (A), Fd and wild type SiR (B), Fd and R111Q SiR or R11Q SiR alone (C), and Fd and either K582Q SiR, K582Q/K584Q, or K584Q (D) are shown.

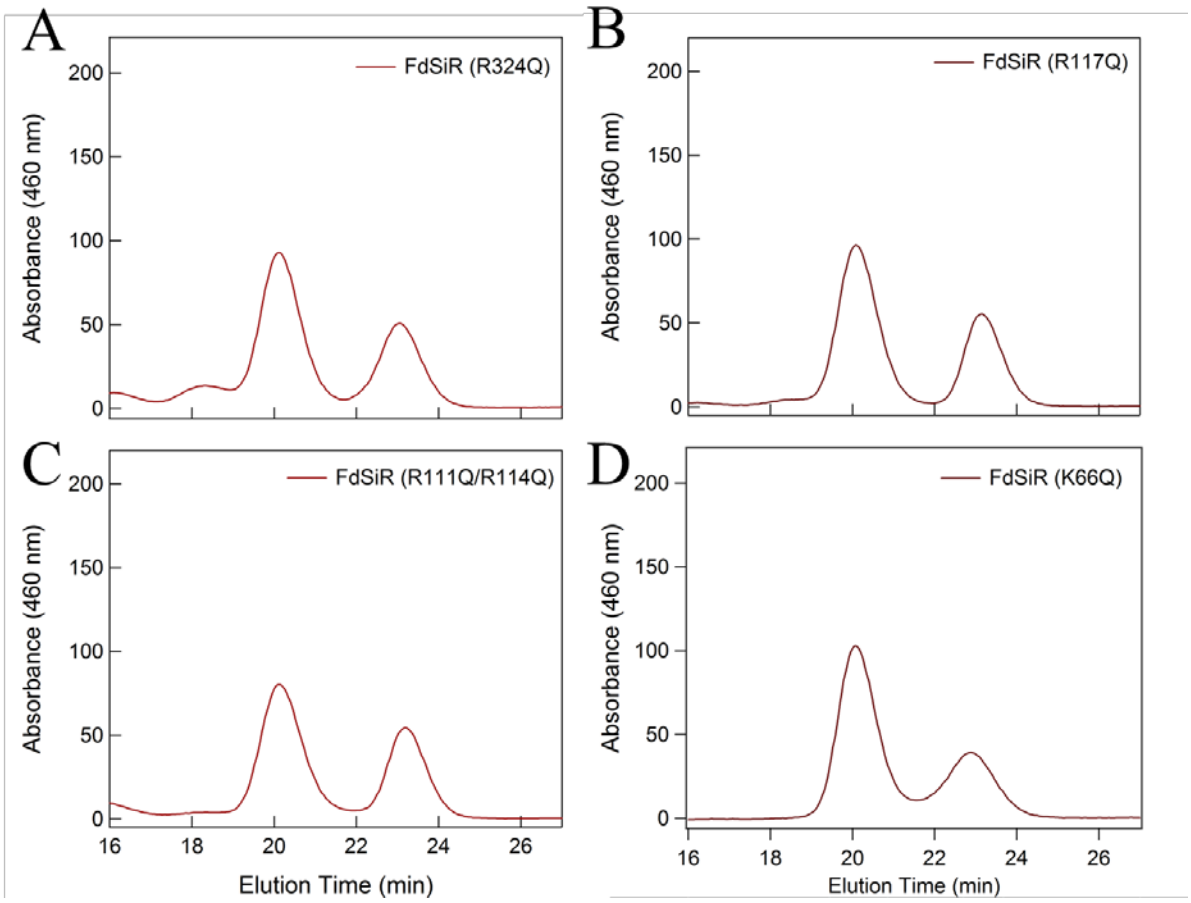

Fig. 2-11. Size exclusion chromatographic analysis on the interaction between Fd and SiR. (A-D) Elution profiles of solutions containing Fd and R324Q SiR (A), Fd and R117Q SiR (B), Fd and R111Q/R114Q SiR (C), and Fd and K66Q SiR (D) are shown.

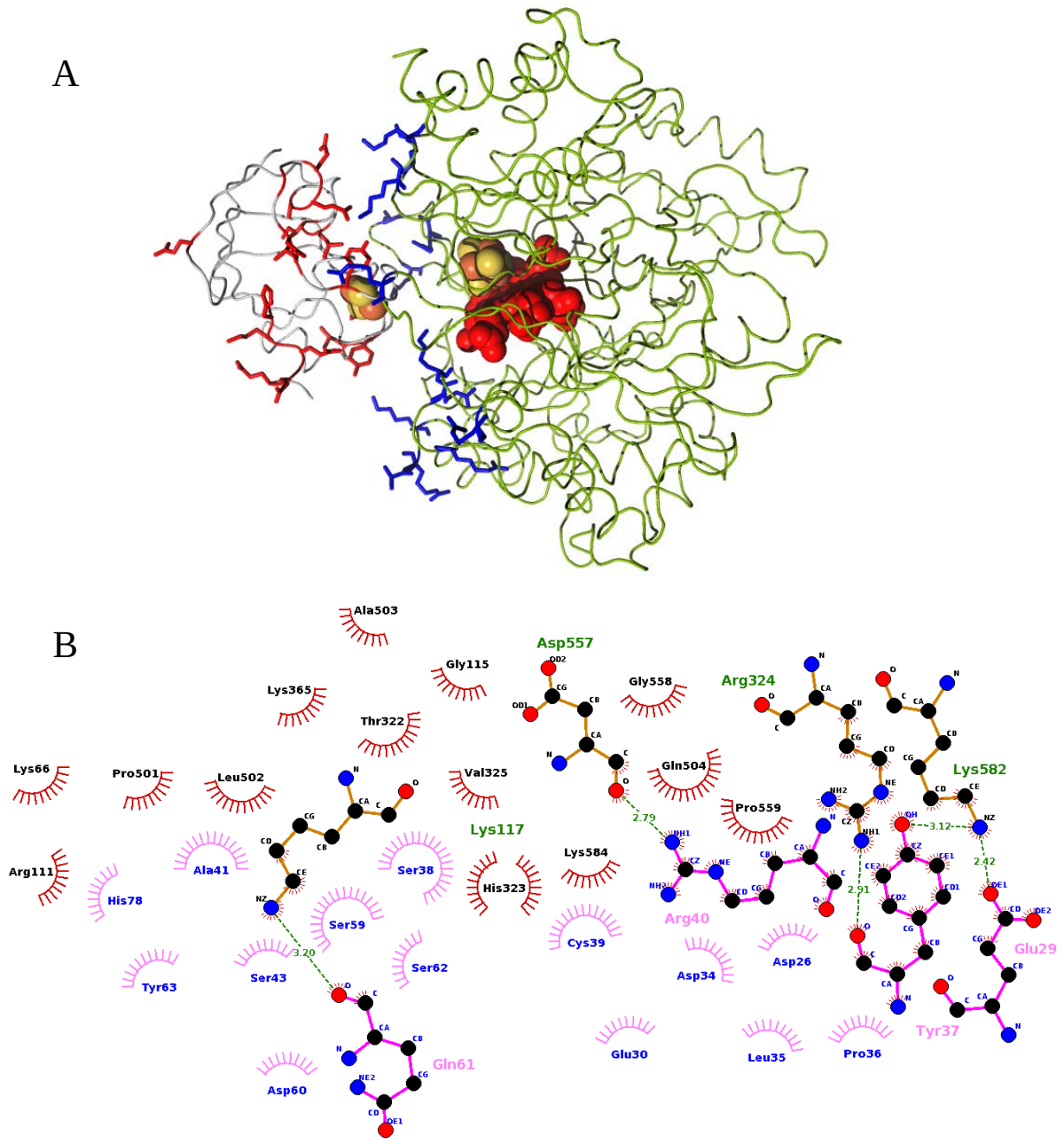

Fig. 2-12. Representative scheme of interfaces in the Fd:SiR complex (complex AC).
(A) Negatively charged residues of Fd (gray) and positively charged residues of SiR (green) are shown with red and blue sticks, respectively. (B) A part of interfaces in the complex which shows electrostatic and non-electrostatic interactions.

Discussion

It has been suggested that electrostatic and van der Waals interactions both function in a binding mechanism (39,43-47). Long-range electrostatic interactions first steer intermolecular recognitions then short-range van der Waals interactions act on effective packing in contact regions. Therefore, for the deeper understanding intermolecular these intermolecular interactions, determination of a stereo-structure of a protein complex is a straightforward approach.

In this regard, complex formation of Fd and SiR is an excellent model system for investigating contributions of intermolecular electrostatic interactions to complexation and to electron transfer as following reasons. First, Fd is an acidic protein and has many acidic residues. SiR has a basic patch with positively charged residues which is considered to be at the interface when it forms complex with Fd for electron transfer (3,4,25). However, there is no available direct information at the atomic levels probably due to difficulty in obtaining and handling SiR from higher plants. Second, there are several available biochemical and biophysical data to be used for interpreting contributions of intermolecular electrostatic interactions. Third, Fd interacts with a lot of redox partners (25). Therefore, the detailed study and systematic comparison can be expected by obtaining information based on a number of case studies. SiR is one of the challenging redox partners to be examined.

We successfully determined 3D structures of Fd:SiR complex together with free Fd and SiR (Fig. 2-4). Fd and SiR were made up of combinations of α-helices and β-strands with loops. The two redox centers, the [4Fe-4S] cluster and sirohaem, were stabilized in SiR and the distance between intraredox centers (4-5 Å) was appropriate enough for electrons to flow (1,5) (3,6).

We obtained the three complex structures which showed similar binding sites but distinct binding modes (i.e., configuration) depending on the distinct condition of crystallization (Fig. 2-5). In addition, interacting sites of Fd for SiR detected by solution-state NMR spectroscopy (4) were well located to interfaces of Fd determined by current crystal structures (Fig. 2-6). These findings indicated that three complex structures obtained in this study are possible, and that overall binding sites of Fd for SiR are similar in both crystal and solution and subtle differences in binding modes are susceptible to ambient conditions.

There were no significant changes of conformations (judged from RMSD, data not shown) and flexibility (judged from *B*-factors, data not shown) of Fd and SiR upon forming a

complex, indicating rigid binding between the two proteins. It was found that one Fd bound to one SiR and binding sites were composed of several of basic and acidic residues from SiR and Fd, respectively (Fig. 2-4 - 2-6 and 2-9). The oppositely charged residues formed electrostatic networks including the ion pairs and a lot of hydrogen bonds, clearly illustrating essential contributions of electrostatic interactions to stabilizing Fd:SiR complex (Fig. 2-12). SiR and Fd made a complex in a proper orientation facing its redox center each other and distance of around 12-13 Å between redox centers (Fig. 2-5), which can allow intermolecular electron transfers.

Based on intermolecular binding interfaces of stereo-structures of the Fd:SiR complex, I prepared a series of SiR mutants by neutralizing basic residues on biding sites, R111Q, R114Q, R117Q, R324Q, K582Q, K584Q, and K582QK584Q (Fig. 2-7), to further examine consequences of intermolecular electrostatic interactions. Then, the affinity of mutant SiRs for Fd was analyzed by Fd-dependent assay in the presence of increasing concentrations of Fd as shown in Fig. 2-9. Double mutants, R111Q/R114Q and K582Q/K584Q, and single mutants, R111Q and R324Q, exhibited extremely low activity. K582Q and K584Q decreased activity to some extent compared to wild type. These kinetical data suggested that the decreased ability of mutant SiRs in the Fd-dependent activity was due to weakened affinity of mutant SiRs for Fd.

In this context, therefore, physical complex formation between wild type and mutant SiRs with Fd was investigated using a size exclusion chromatography as described previously (Fig. 2-10 and 2-11). When a mixture of Fd and wild-type SiR in a molar ratio of 1:1 was loaded, SiR and Fd were eluted as a single major peak (Fig. 2-10A), and further addition of Fd over the 1:1 ratio was resulted in an elution of the excess Fd as a separate peak (data not shown), confirming the stoichiometric formation of the complex of SiR and Fd. The equivalent gel filtration of K582Q/K584Q (Fig. 2-10D) and R324Q with Fd (Fig. 2-11A) showed that these mutants abolished the ability to form the complex with Fd.

In the meantime, no remarkable changes in Fd- and MV-dependent SiR activity of non-electrostatic mutants implicated direct electron transfer in a through-space mechanism.

Based on these combined data, I suggest that almost all of the basic amino acid residues of SiR at the interface of the complexes of SiR and Fd are generally contributed to the protein-protein interaction which governs an efficient acceptance of reducing equivalents from reduced Fd.

Chapter III

Interfacial mutagenesis of sulfite reductase influences its activity and interaction with ferredoxin and substrates

Abstract

Sulfite reductase (SiR) conducts the reductive conversion of sulfite to sulfide using reducing power of electron transferred from ferredoxin (Fd). I previously showed that interprotein electrostatic interactions between SiR and Fd are essential for SiR activity by forming the productive electron transfer complex (chapter II): however, the contribution of interfacial residues to the complex formation and SiR activity still remains to be elucidated.

Here, we examined mutagenic effects of SiR on activity of SiR and its binding ability for Fd using site-directed mutagenic analysis in combination to the types of SiR activity assays with three types of substrates, solution-state NMR spectroscopy, and isothermal titration calorimetry (ITC). Two types of SiR activity assays revealed that disruption of interprotein electrostatic interactions by neutralizing positive charges of SiR influences mostly SiR activity without remarkable changes in substrate preference. ITC and NMR results showed abolishment of binding ability of a K582Q/K584Q double mutant of SiR for Fd. A unique electrostatic network on large patches of positive charges of SiR which complements the loss of a single positive charge of SiR for Fd interaction by mutation was also observed.

Meanwhile, SiR mutants, which hydrophobicity decreased, showed distinct changes in SiR activity depending on the type of substrates. ITC results showed that thermodynamic parameters of the complex formation of Q504G SiR with Fd were similar to those of wild type SiR. Similar but distinct binding sites of ^{15}N-labeled Fd for wild type SiR and Q504G SiR were revealed by the chemical shift difference and distinct direction of NMR peak shifts.

These findings demonstrate that intermolecular electrostatic interactions are fundamental for SiR activity by forming the productive electron transfer complex and hydrophobic interactions play an important role for substrate preference using subtle differences in configuration of the Fd:SiR complex. I suggest that enzymes may evolve to use skillfully these non-covalent interprotein forces for biological efficiency.

Introduction

Plant sulfite reductase (SiR) is an indispensable enzyme for the reductive sulfur assimilation in plants, algae, and cyanobacteria by catalyzing the six-electron reduction of sulfite to sulfide (2-4). SiR is a soluble monomeric enzyme with a single domain. SiR is a relatively large with a molecular mass of approximately 65 kDa and contains a single siroheme and a single [4Fe-4S] cluster as prosthetic groups for intra- and intermolecular electron transfer, respectively. Plant-type ferredoxin (Fd) is a small acidic protein with a molecular mass of approximately 11 kDa (4,11). Fd carries one electron using a single [2Fe-2S] cluster and serves as a physiological electron donor for several enzymes including SiR, ferredoxin $NADP^+$ reductase, and nitrite reductase (2-4,11). The midpoint redox potential (E_m) of the [4Fe-4S] cluster and siroheme in maize SiR are -415 and -285 mV, respectively (3). Therefore, electron flow thermodynamically to SiR from the reduced Fd, which has E_m of -423 mV.

In order to understand the interplay among interprotein electron flow, SiR activity, and the formation of the Fd:SiR complex, we recently determined the X-ray crystal structures of the Fd:SiR complex (chapter II). The binding interfaces showed the electrostatic network mainly from positive charges of SiR and negative charges of Fd. The central regions in front of the [4Fe-4S] cluster of SiR were mostly hydrophobic in nature and were well matched with the hydrophobic regions in front of the [2Fe-2S] cluster of Fd for an efficient intermolecular electron transfer.

Our previous mutagenic studies and biochemical investigation (2,4) demonstrated that deletion of negative charges of Fd at interfaces or near interfaces revealed in crystal structures dropped SiR activity with weakened binding affinity for SiR. Similarly, neutralizing positive charges of SiR at interfaces greatly decreased SiR activity and binding affinity for Fd (chapter II). All these results suggest that intermolecular electrostatic interactions between Fd and SiR are important for the complex formation which is prerequisite for SiR activity. Meanwhile, decreasing hydrophobicity of SiR at interfaces did not affect SiR activity and interprotein interactions with Fd as shown by the chromatographic analysis (chapter II).

In order to obtain deeper insights into the contribution of electrostatic and hydrophobic interactions to the complex formation and its relation to SiR activity, we herein performed in-depth biochemical and biophysical studies using mutagenesis, SiR activity measurements for

the three types of substrates (sulfite, nitrite, and hydroxyl amine), isothermal titration calorimetry (ITC), and solution-state NMR spectroscopy.

Two types of SiR activity assays demonstrated that disruption of interprotein electrostatic interactions, stabilized by both enthalpy and entropy changes, by neutralizing basic residues of SiR decreases mostly SiR activity without no remarkable substrate preference and binding ability for Fd as shown by the ITC and NMR analyses. On the other hand, activity of SiR mutants with decreased hydrophobicity depended on the type of substrates. Although ITC results showed no appreciable differences in thermodynamic parameters of formation of the Fd:SiR complex, residue-based NMR results of ^{15}N-labeled Fd revealed distinct binding modes of mutant SiR for Fd compared to wild type SiR.

Our findings clearly elucidate that intermolecular electrostatic interactions are fundamental for SiR activity to form the electron transfer-competent complex and hydrophobic interactions play an important role for substrate preference using subtle different binding modes although they do not contribute largely to the complex formation. Finally I propose that enzymes may evolve to use properly non-covalent interprotein forces for biological efficiency.

Materials and Methods

Analysis of substrate preference using Fd-dependent SiR activity assay

SiR activity was measured using NADPH/FNR/Fd redox cascade (2,3) to compare substrate preference in the presence of sulfite (SO_3), nitrite (NO_2), or hydroxyl amine (NH_2OH). The reaction mixture for Na_2SO_3 and $NaNO_2$-dependent activity consisted of 3 μM FNR, 4 μM SiR, 1 mM Na_2SO_3, 1 mM $NaNO_2$ and 20 μM Fd in 50 mM Tris-HCl, pH 7.5 containing 100 mM NaCl. That for NH_4OH-dependent activity consisted of the same components except for 2 mM NH_2OH. The reaction was initiated by adding NADPH at a concentration of 1 mM at 30 ℃. Oxidation of NADPH was directly measured spectrophotometrically its decrease in A_{340} for sixty seconds. Enzymatic reaction rate was extrapolated from derivation of measurements.

Measurements of isothermal titration calorimetry

Isothermal calorimetric titration (ITC) of Fd to wild type and mutant SiRs in 50 mM Tris-HCl buffer (pH 7.5) at 100 mM NaCl was performed by using a VP-ITC instrument (GE-Healthcare, USA) at 30 °C. Binding reactions were initiated with the addition of Fd (1.49 mM) in the syringe to SiR (40 μM) in the cell. Titration of Fd was comprised of 38 injections with the spacing time of 300 s and the stirring speed of 307 rpm. The injection volume was 2 or 7 μL for each. The corresponding heat of dilution of Fd titrated to the buffer was used to correct data. Binding isotherms were analyzed with the theoretical curve of equation 1,

$$Q = \frac{n[\mathrm{SiR}]_t \Delta H V_0}{2}\left[1+\frac{[\mathrm{Fd}]_t}{n[\mathrm{SiR}]_t}+\frac{K_d}{n[\mathrm{SiR}]_t}-\sqrt{\left(1+\frac{[\mathrm{Fd}]_t}{n[\mathrm{SiR}]_t}+\frac{K_d}{n[\mathrm{SiR}]_t}\right)^2-\frac{4[\mathrm{Fd}]_t}{n[\mathrm{SiR}]_t}}\right]$$

Equation 1

where Q and n are the change in heat and the binding stoichiometry of Fd per a binding site on SiR, respectively. ΔH indicates the change in enthalpy and V_0 is the effective volume of the calorimeter cell (~1.43 ml). The total concentration of SiR in the cell and Fd in the syringe are shown with $[\mathrm{SiR}]_t$ and $[\mathrm{Fd}]_t$, respectively, at any given point during titrations. K_d indicates the dissociation constant. Based on non-linear fitting to equation 1, the values of n, ΔH_{bind}, and K_d were obtained.

By using the known values of ΔH_{bind} and K_d and the following thermodynamic relationships, equations 2 and 3, the change in Gibbs free energy (ΔG_{bind}) and entropy (ΔS_{bind}) was calculated.

$$\Delta G_{bind} = RT \ln K_d \quad \text{Equation 2}$$

$$\Delta G_{bind} = \Delta H_{bind} - T\Delta S_{bind} \quad \text{Equation 3}$$

NMR measurements

Two dimensional ^{1}H-^{15}N heteronuclear single-quantum coherence correlation (HSQC) spectra of ^{15}N uniformly-labeled Fd in the absence and presence of wild type and mutant SiRs were obtained by using an AVANCE II-800 spectrometer equipped with a cryogenic probe (Bruker, Germany) in 50 mM Tris-HCl buffer (pH 7.4) containing 10% D_2O and 100 mM NaCl at 25 °C. The protein concentrations for NMR measurements were 100 μM for Fd and 50 μM for SiR. Data were processed and analyzed with NMRPipe (48) and Sparky (49), respectively.

Chemical shift perturbation (CSP) of NMR cross peaks in the absence and presence of SiR were calculated by using equation 4:

$$\text{CSP } (\Delta\delta_{ave}) = [(\Delta\delta_{HN})^2 + (\Delta\delta_N \times 0.158)^2]^{0.5} \quad \text{Equation 4}$$

where $\Delta\delta_{HN}$ and $\Delta\delta_N$ are changes in ^{1}H and ^{15}N chemical shifts in ppm, respectively. The weighting factor of 0.158 was used to adjust the relative magnitudes of the amide nitrogen chemical shift range and the amide proton chemical shift range.

Results

Fd-dependent SiR activity with site-directed mutagenesis

In order to examine effects of physicochemical effects of interfacial residues of SiR on enzymatic activity, site-directed mutagenic analyses in combination with SiR activity assay were performed (Fig. 3-1). We first classified interfacial residues to the two groups, electrostatic and non-electrostatic residues, for mutating SiR. Representatively, R111, R324, K582 and K584 were selected to eliminate positive charges and L499, P501, and Q504 were chosen to change polar and/or hydrophobic natures. As a consequence, we prepared K582Q/K584Q which were designated as electrostatic mutant hereafter and Q504G which termed non-electrostatic mutant.

Fd-dependent assay showed the elevation of enzymatic activity of wild type SiR with increases in Fd concentrations, indicating increases in the turnover numbers (Fig. 3-1). Most of the electrostatic mutants showed decreases in activity compared to that of wild type although the degree of changes in activity were different.

A single mutant of K584Q exhibited activity comparable to wild type and activity of K582Q was marginally lower than that of wild type. However, R111Q and R324Q showed drastic dropping in activity, suggesting that SiR activity was subjected to location of positive charges on SiR surfaces. It should be noted that a double mutant of K582Q/K584Q displayed significant decreases in activity in spite of low decreases in activity of each single mutant, raising a possibility of cooperative synergetic effects of neutralization of (Fig. 3-1A) positive charges on activity.

Meanwhile, a series of non-electrostatic mutants, L499G, P501G, A503G, and Q504G, showed less disruption of activity than electrostatic mutants (Fig. 3-1B). Although some mutants, e.g., Q504G and P501G, showed higher turnover numbers than wild type, apparent interprotein affinity of all non-electrostatic mutants were relatively similar to wild type based on K_m values (approximately 10 μM), suggesting that these non-charged, hydrophobic and polar residues were not predominantly involved in the strong affinity for Fd.

Interprotein affinity and binding energetics between Fd and SiRs examined by isothermal titration calorimetry

In order to examine thermodynamically roles of electrostatic and non-electrostatic interactions in forming the Fd:SiR complex at the molecular level, we conducted ITC measurements using wild type SiR and two types of SiR mutants (K582Q/K584Q and Q504G) (Fig. 3-2).

On titrating of Fd to wild type SiR, successive negative ITC peaks in thermograms were observed (Fig. 3-2, upper panels), which indicated formation of the Fd:SiR complex with large exothermic heat. The analyses of the binding isotherm (Fig. 3-2, lower panels) showed negative enthalpy change for binding (ΔH_{bind}) of -4.4 kcal/mol and positive entropy change for binding (ΔS_{bind}), $-T\Delta S_{bind}$ of -4.9 kcal/mol (Table 1). Negative ΔH_{bind} and positive ΔS_{bind} indicated typical positive contribution of electrostatic interactions and hydrophobic effects, respectively. Combination of energetic gains from both driving forces resulted in the Gibbs free energy change for binding (ΔG_{bind}) of -6.3 kcal/mol. The dissociation constant (K_d) was 29 μM.

K582Q/K584Q mutant which showed the significant decrease in activity was selected among electrostatic mutants. Titration of Fd to K582Q/K584Q SiR showed drastic changes. There was no observable heat, which indicated no appreciable binding reaction due to the considerable decrease in the interprotein affinity Next, in order to investigate thermodynamically non-electrostatic contribution, the ITC measurement of Fd binding to Q504G mutant was performed. The similar ITC thermogram and binding isotherm to those of wild type without remarkable altering of binding thermodynamic parameters were obtained (Fig. 3-2 and Table 3-1).

Residue-based solution-state NMR investigation on interprotein interactions between ferredoxin and sulfite reductase

In order to explore the binding interface and mode between the two proteins at the residue level in solution, we performed a series of ^{1}H-^{15}N HSQC measurements (Fig. 3-3). The detailed NMR study of SiR in solution is still difficult due to its large size (~65 kDa) which causes the severe peak broadening and overlapping. Therefore, the solution-state NMR spectroscopy of ^{1}H-^{15}N HSQC was performed on uniformly labeled ^{15}N Fd in the absence and presence of SiR at 100 mM NaCl.

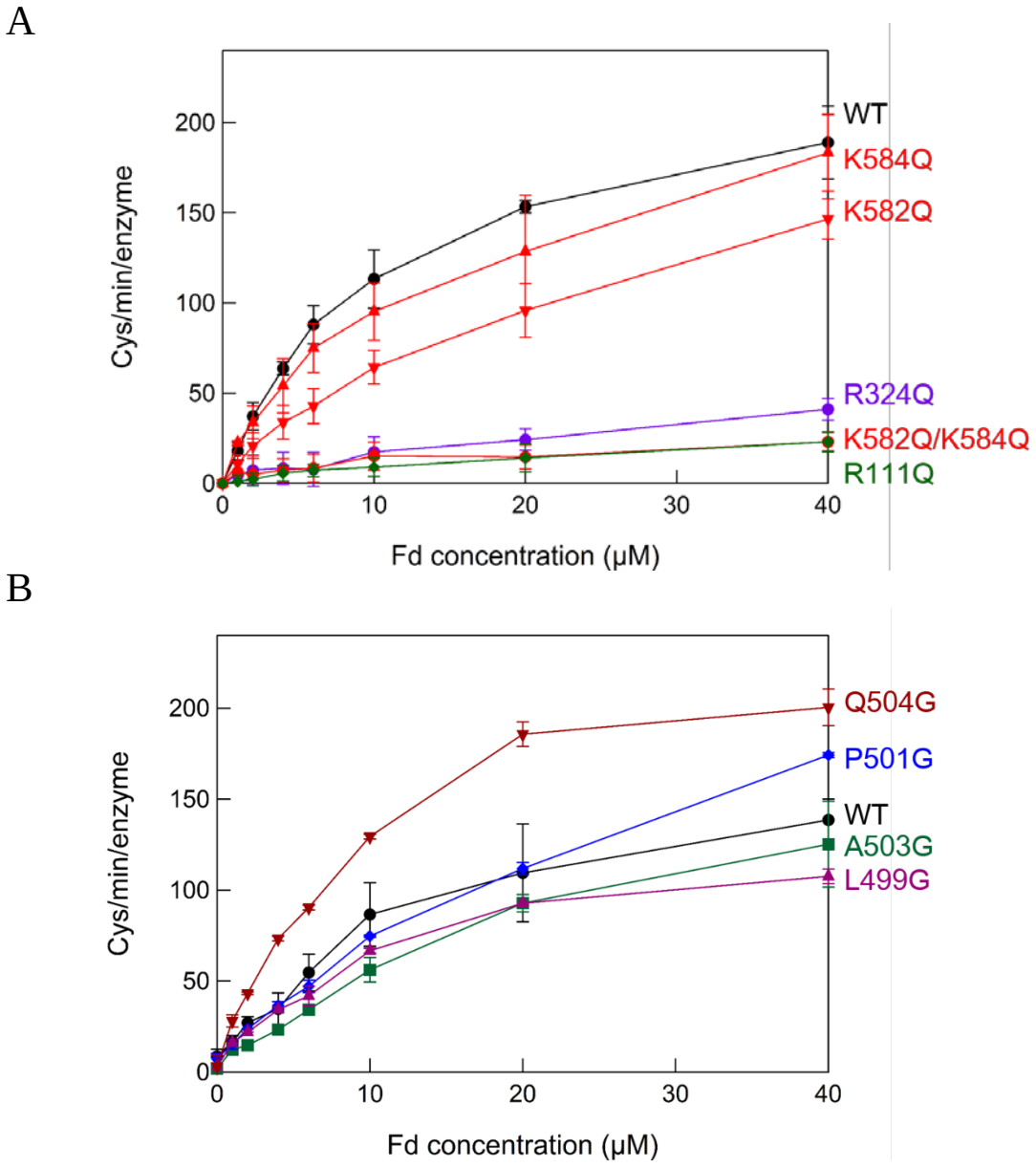

Fig. 3-1. Enzymatic activity of wild type and mutant SiRs measured by Fd-dependent assays.

Activity of each SiR is plotted against the concentration of Fd and represented by the color code.

We first recorded the ^{1}H-^{15}N HSQC spectra of Fd in the presence of wild type SiR without NaCl. Considering the peaking broadening of Fd on binding to SiR, we carefully chose the molar ratio of Fd/SiR to two based on K_d obtained by ITC. In addition, this allowed us to observe promptly mutation-dependent changes in interprotein affinity without severe peak broadening due to excess amounts of SiR by determining differences in chemical shifts (see below). The spectrum displayed shifts in position of a lot of NMR peaks, which indicated the formation of the Fd:SiR complex (Fig. 3-3).

To obtain detailed quantitative and qualitative information, we calculated the chemical shift difference (CSD) and mapped the residues onto the structure of SiR-bound Fd depending on the degree of CSD (Fig. 3-4A). Largely, the three parts of Fd were involved in forming a complex with SiR: A28, E29, D34 and Y37 in the N-terminal parts, G49, Q61, and L64 around the [2Fe-2S] cluster, and K91, E92, and E93 in the C-terminal part, which were in good agreements of our X-ray crystal structures (Fig. 2-4) and previous NMR studies (4). It should be noted that the residues around the [2Fe-2S] cluster due to the paramagnetic relaxation enhancement (PRE) effect were not available. Most importantly, the charged residues of Fd were mostly perturbed and the polar and apolar residues also showed perturbation.

However, the addition of K582Q/K584Q SiR showed no changes in the peak position and intensity of Fd (Fig. 3-4B). This suggested no detectable interactions between K582Q/K584Q SiR and Fd, which coincided with ITC results. On the one hand, the NMR peaks of Fd in the presence of Q504G SiR, which showed a lot of the peak shift. The pattern of the peak shift and the number of peak which showed perturbation were similar to those with wild type (Fig. 3-4C). The degree of CSD in the central and C-terminal parts including D60, Y63, D65, A79, and Y80 (Fig. 3-5) and the direction of peak shifts (Fig. 3-6) were obviously distinct from those with wild type.

Substrate type-dependent SiR activity monitored by NADPH oxidation

In order to obtain deeper insights into properties of enzymatic activity of SiR, I introduced alternative enzymatic assay which monitored the oxidation of NADPH by using the three distinct substrates, sulfite (SO_3^{2-}), nitrite (NO_2^-), and hydroxylamine (NH_2OH) (Fig. 3-7).

I first monitored kinetics of reduction of each substrate by using wild type SiR (Fig. 3-7). The exponential decreases in absorbance at 340 nm corresponding to NADPH oxidation

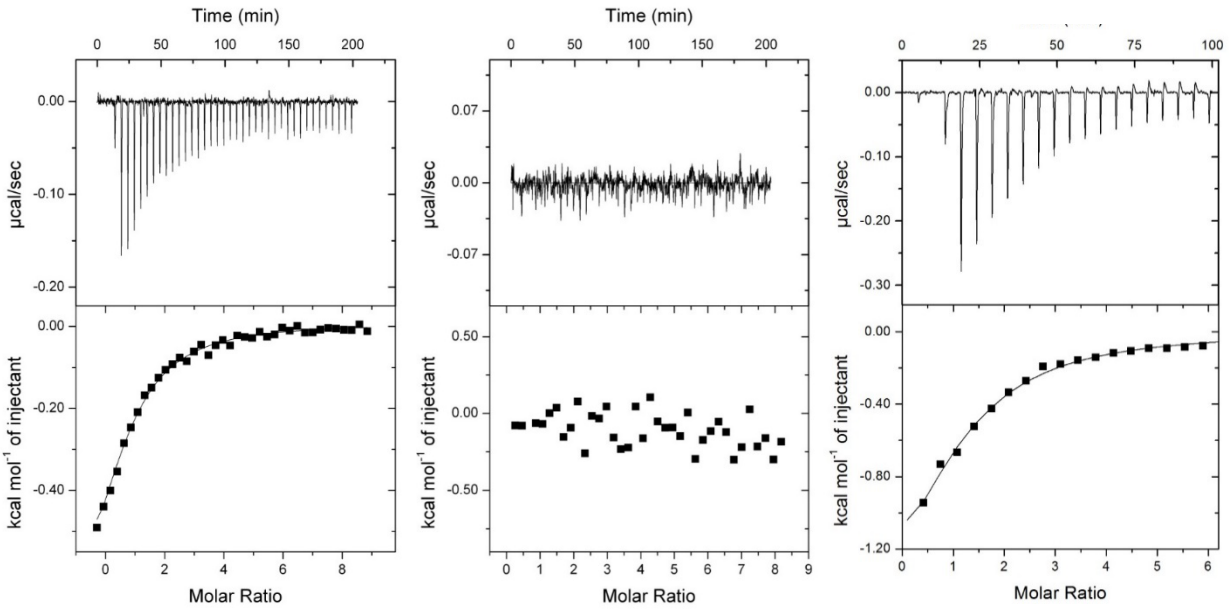

Fig. 3-2. Isothermal titration of Fd to wild type and mutant SiRs.

Consecutive titration of Fd to wild type SiR (left), K582Q/K584Q (middle), and Q504G (right), is shown, respectively. Each binding thermogram (upper panel) and isotherm (lower panel) is also shown. Solid lines in binding isotherms indicate fitted curves.

Table 3-1. Summary of thermodynamic parameters for the Fd:SiR complex formation.

[a]the number of Fd which binds to a binding site of SiR.

[b]wild type SiR

[c]best fit with a one-site binding model.

[d]KK: a mutant of SiR, K582Q/K584Q

[e] N.D. indicates ″not determined″.

[f]Q: a mutant of SiR, Q504G

SiR	NaCl (mM)	n^a	K_d (μM)	ΔH_{bind} (kcal/mol)	$-T\Delta S_{bind}$ (kcal/mol)	ΔG_{bind} (kcal/mol)
W.T.[b]	100[c]	~1	23	-0.9	-5.6	-6.5
KK[d]	100[c]	N.D.[e]	N.D.[e]	N.D.[e]	N.D.[e]	N.D.[e]
Q[f]	100[c]	~1	16	-2.0	-4.6	-6.6

were observed in all reaction mixtures of substrates and ensured substrate-dependent activity assay.

I specially focused SiR variants which did not show large changes in SiR activity revealed by Fd- and MV-dependent assays and in physical interactions with Fd compared to those of wild type so as to uncover a hidden role for SiR activity. Hence, a series of non-electrostatic mutants of SiR (L499G, P501G, A503G, and Q504G) were selected and their enzymatic activity was measured at distinct concentrations of individual substrates.

Regardless of the type of substrates, increases in activity were obtained in a substrate concentration-dependent manner (Fig. 3-8). Activity of a non-electrostatic mutant was different depending on substrates. Activity of Q504G for hydroxylamine was similar to that of wild type, but activity for nitrite obviously decreased and activity for sulfite is even higher at lower concentration. By contrast, A503G showed the decrease in activity for sulfite and no changes for nitrite and hydroxylamine in activity (Fig. 3-8).

In addition, at the same substrate, activity of each non-electrostatic mutant depended on types of mutation (Fig. 3-8). Although activity for sulfite of wild type, L499G, was all similar, activity of P501G, Q504G and A503G increased and decreased, respectively. When nitrite was used for a substrate, L499G, P501G, and Q504G showed large decreases in activity. L499G also showed decreases in activity for hydroxylamine.

Distinct activity changes suggested the contribution of non-electrostatic interaction between the two proteins to SiR activity by sensing different substrates.

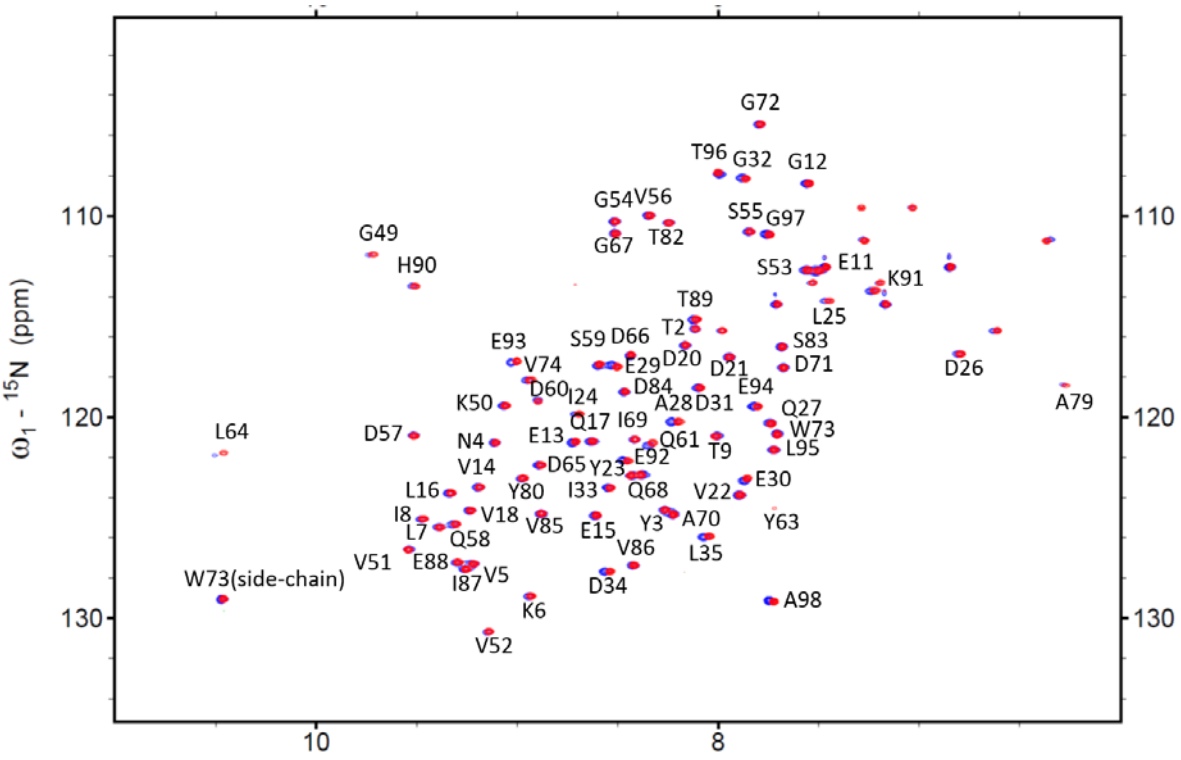

Fig. 3-3. Solution-state NMR measurements of Fd with and without wild type SiR.
Two-dimensional ^{1}H-^{15}N HSQC spectra of ^{15}N-labeled Fd (100 μM) in the absence (red) and presence of 50 μM SiR (blue) at 100 mM NaCl.

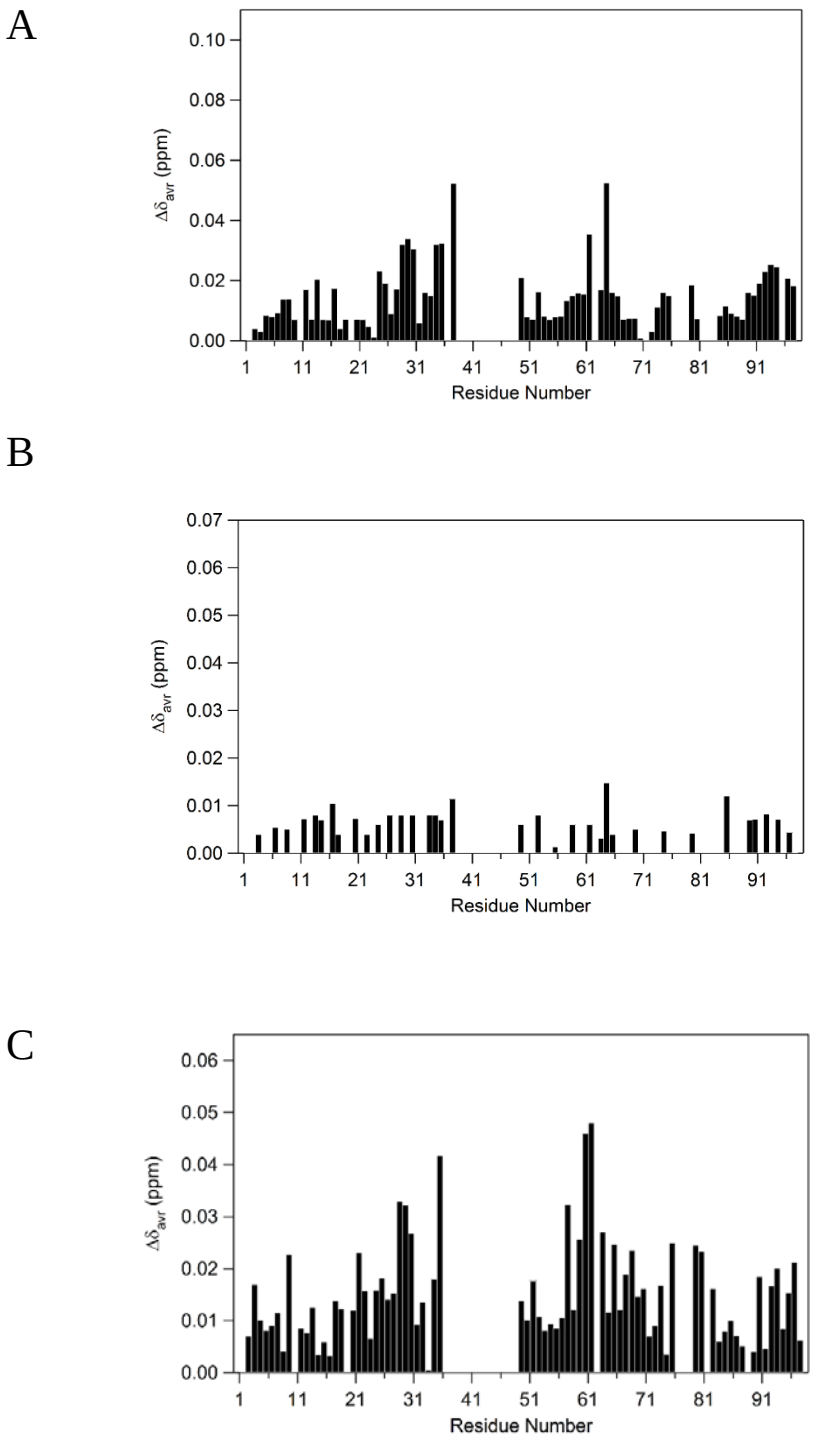

Fig. 3-4. Chemical shift perturbations of Fd in the presence SiRs.

Differences in chemical shift of Fd in the presence of wild type (A), K582Q/K584Q (B), and Q504G SiRs (C) at 100 mM NaCl were plotted against the residue number.

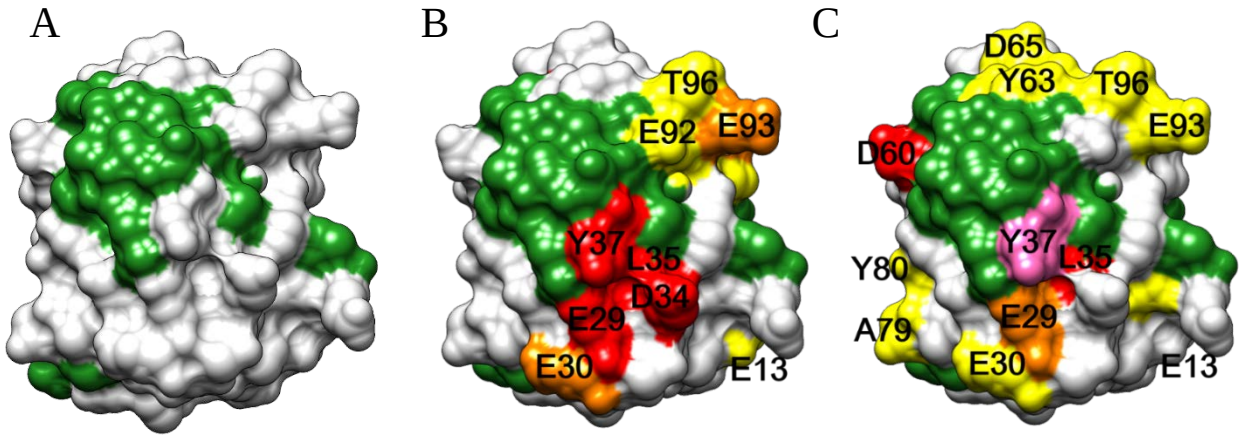

Fig. 3-5. Mapping of interacting residues of Fd for SiR onto the crystal structure of Fd. (A-C) The degree of the chemical shift difference (CSD) was mapped onto the crystal structure of Fd (PDB ID: 1GAQ) (11) in the presence of wild type SiR (A), K582Q/K584Q SiR (B), and Q504G SiR. The color code for the finite CSD analysis is as follows: Red, CSD > 0.04; orange, 0.04 > CSD > 0.03; yellow, 0.03 > CSD > 0.02. The NMR invisible peaks (due to paramagnetic relaxation enhancement) are shown by green. Pink color represents invisible residue upon binding with Fd.

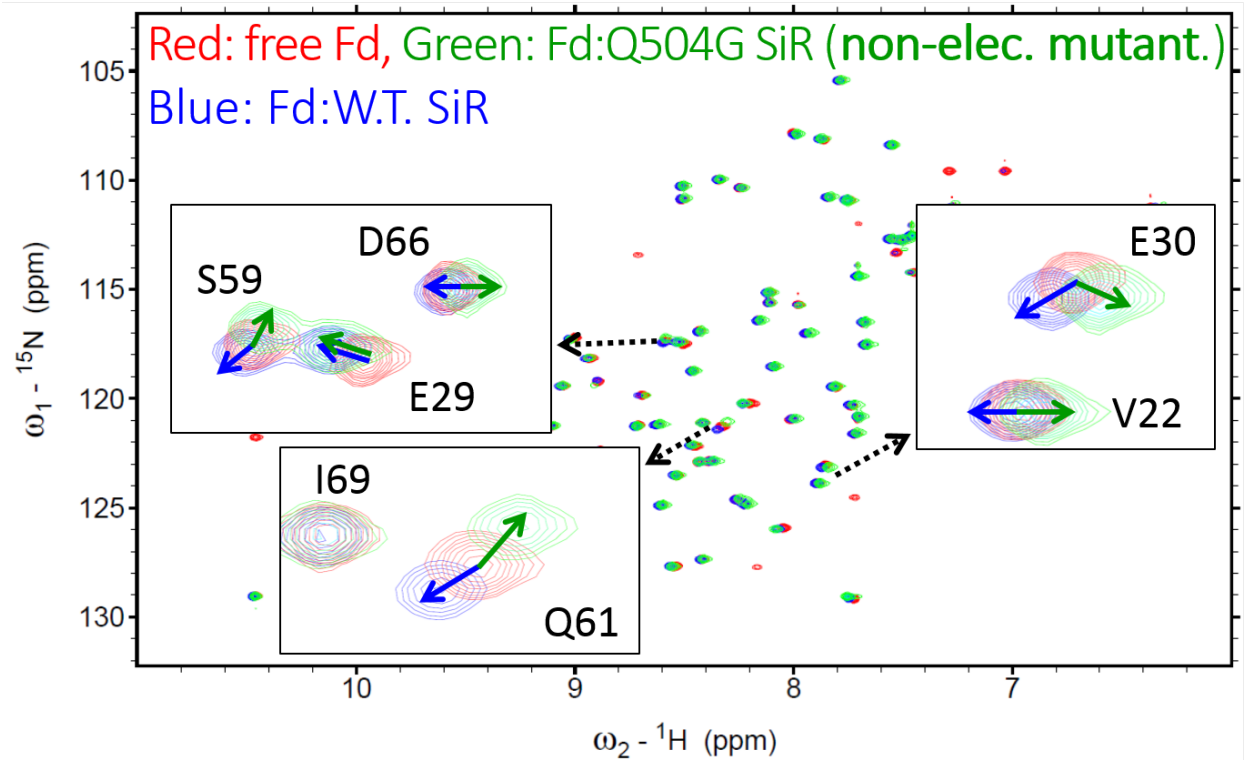

Fig. 3-6. Direction of the peak shift of Fd upon binding with wild type SiR and Q504G SiR.

The direction of the peak shift of Fd was represented by blue arrows for binding of wild type SiR and green arrows for binding of Q504G SiR mutant. The peak position of free Fd is shown in red.

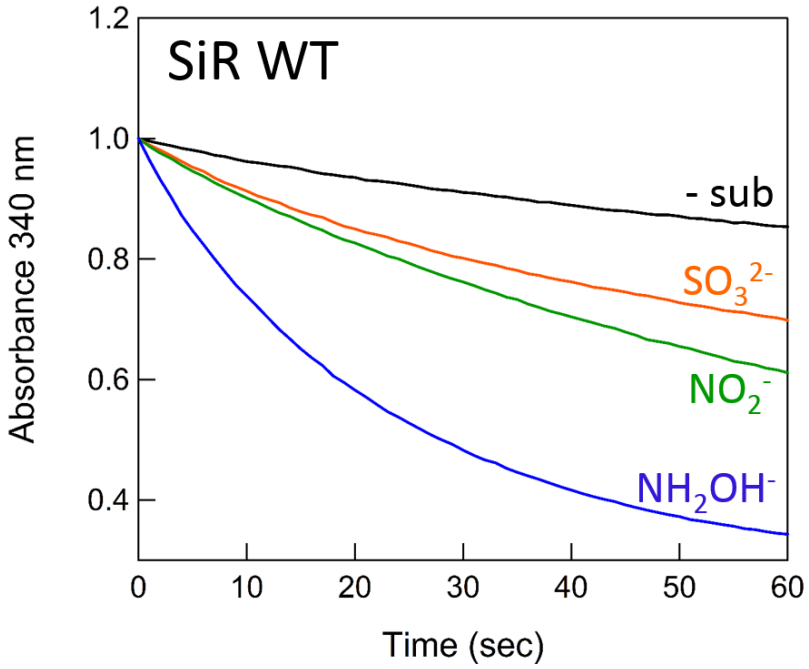

Fig. 3-7. Monitoring of NADPH oxidation by SiR with three types of substrates.

A redox cascade of NADPH/FNR/Fd/SiR was traced by monitoring the decrease in absorbance at 340 nm. Kinetic traces for sulfite, nitrite, and hydroxylamine reduction are shown with orange, green, and blue curves, respectively.

A

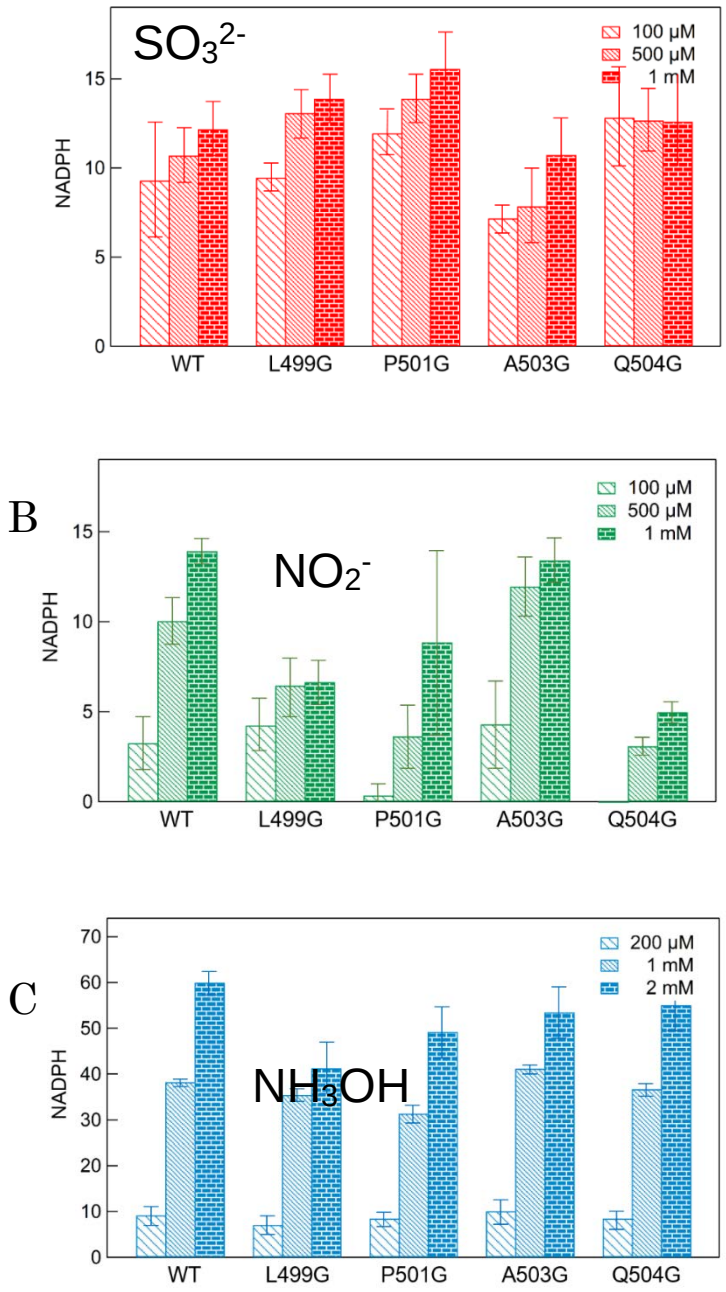

Fig. 3-8. SiR activities monitored by NADPH oxidation.

(A-C) Bar representation of NADPH oxidation by wild type and mutant SiRs is shown for three types of substrates: sulfite (SO_3^{2-}) (A), nitrite (NO_2^-) (B), and hydroxylamine (NH_3OH) (C). The concentration of each substrate used was 100 μM, 500 μM, and 1 mM (for hydroxylamine, 200 μM, 1 mM, and 2 mM).

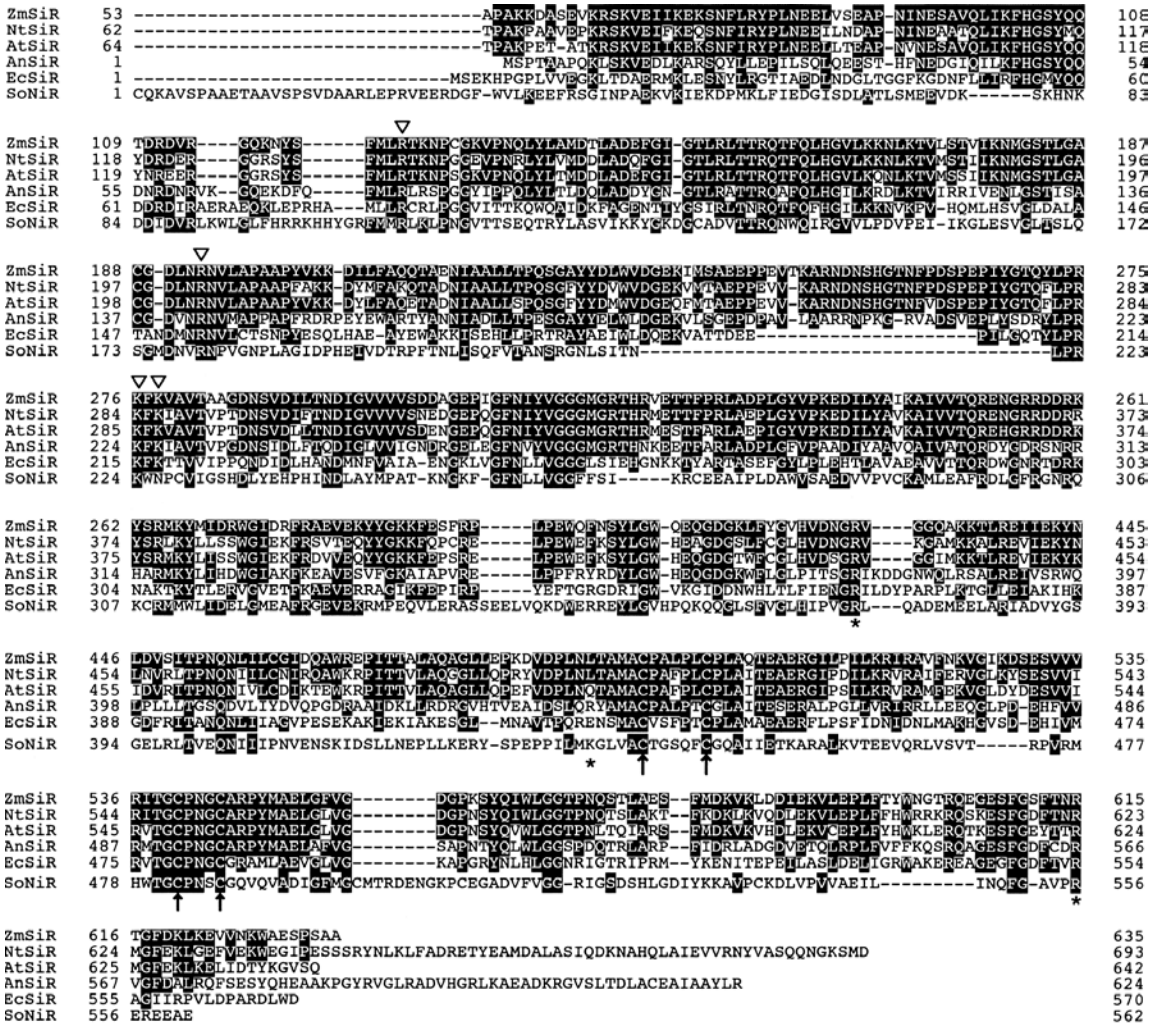

Fig. 3-9. Comparison of amino acid sequences of SiRs.

The sequence of SiR from plant, cyanobacterium, and *E. coli* is shown with the sequence of plant NiR. Amino acid sequences of Fd-SiRs from maize (ZmSiR), tobacco (NtSiR), *Arabidopsis* (AtSiR) and *Synechococcus* PCC7942 (AnSiR), the hemoprotein subunit of *E. coli* of NADPH-SiR (EcSiR) and Fd-NiR from spinach (SoNiR) are aligned with gaps inserted to obtain the maximum homology. The mature regions are presented. Four conserved cysteine residues (Cys-434, Cys-440, Cys-479 and Cys-483 in *E. coli* enzyme) ligating the [4Fe–4S] cluster and the siroheme are shown by arrows, and four basic residues involved in the hydrogen-bonding network (Arg-83, Arg-153, Lys-215 and Lys-217 in *E. coli* enzyme) by triangles.

Discussion

The crystal structures of the Fd:SiR complex showed well-organized electrostatic interactions at interfaces with non-electrostatic interactions including polar and hydrophobic contacts. The net energetic contribution of these intermolecular contacts was found to be negative ΔH_{bind} (Fig. 3-2 and Table 3-1), which prefers the formation of the Fd:SiR complex. Positive ΔS_{bind}, resulting from indirect molecular contacts such as dehydration and/or increased flexibility (i.e., conformational entropy), (Table 3-1) also drove favorably complex formation.

Disruption of electrostatic interactions by mutation of SiR (R111Q, R324Q, and K582Q/K584Q) caused the loss of binding capability of SiR for Fd as shown by the ITC and NMR analyses (Fig. 3-2, 3-3 - 3-6), thereby decreasing largely Fd-dependent SiR activity (Fig. 3-1). Decreased binding affinity of [Fe-Fe] hydrogenase for Fd and activity by neutralization of positive charges of [Fe-Fe] hydrogenase were also interpreted by weakened intermolecular electrostatic interactions (50). In addition, we previously showed that deletion of negative charges of Fd decreased affinity for SiR and SiR activity (4).

Interestingly, a unique electrostatic network for SiR activity was detected. A single SiR mutant of K582Q and K584Q retained activity comparable to that of wild type; activity of a double mutant, K582Q/K584, decreased remarkably. Recovery of activity could be possible with an aid of neighboring positive residues by complementing a loss of a favorable single positive charge for activity, which is a complementary system within large patches of positive charges on SiR. Considering conservation of K582 and K584 in plants (Fig. 3-9), this self-repair system may be tailored to cope with the damage by mutation.

On the one hand, decreasing hydrophobicity of Fd at the center of interfaces by mutation did not affect Fd-dependent SiR activity for reducing sulfite (Fig. 3-1), implying the direct electron transfer from Fd to SiR. However, SiR activity for reducing nitrite or hydroxyl amine varied depending on the types of non-electrostatic SiR mutants. Q504G SiR, as a representative non-electrostatic SiR mutant, showed no remarkable differences in thermodynamic properties for forming the complex with Fd (Fig. 3-2 and Table 3-1).

However, close investigation of multi-dimensional NMR spectroscopy revealed the differences in binding modes (i.e, configuration) between the Fd:wild type SiR complex and the Fd:Q504G SiR complex. Differences in CSD (Fig. 3-4 and 3-5) and direction of the peak

shift (Fig. 3-6) were observed in the center and C-terminal part as well as the N-terminal and central part, respectively (Fig. 3-5), suggesting that these regions surrounding the center active site on Fd are responsible for subtle tuning of complex conformations.

Therefore, it is conceivable that disruption of hydrophobic interactions may result in subtle differences in the fine structures of each individual Fd:SiR complex which influence direct electron flow, thereby producing the substrate-dependent change in SiR activity. Short-range interactions such as hydrophobic and van der Waals contacts tune configuration of the complex as observed in fixing of an encounter complex to a final complex (35,43).

Distinct configuration of the Fd:FNR complex and its relation to FNR activity was also observed by the direction of NMR peak shifts when physicochemical properties at the center of interfaces of Fd for FNR were changed (22). Increasing hydrophobicity of Fd increased FNR activity and binding affinity with slight changes in configuration compared to wild type complex. However, increasing attractive electrostatic interactions by the addition of a negative charge to Fd decreased unexpectedly FNR activity and binding affinity with relatively large different orientation.

Accordingly, I here demonstrated that total SiR activity is governed by interprotein interactions with Fd for efficient interprotein electron transfer from Fd to SiR without perturbing capability of intramolecular activity of SiR. Furthermore, these findings elucidate that the electrostatic interaction at the interface is a more critical factor for the stability of the Fd:SiR complex than the non-electrostatic interaction. However, the non-electrostatic interaction serves as fine-tuning of complex conformations which might be beneficial for the recognition of various substrates. Lastly, I propose that enzymes may evolve to use appropriately these non-covalent interprotein interactions for biological efficiency under various ambient conditions.

Chapter IV

Noncovalent forces finely tune the electron transfer complex between ferredoxin and sulfite reductase to optimize enzymatic activity

Abstract

Plant sulfite reductase (SiR) forms an electron-transfer complex with ferredoxin (Fd) for the reductive conversion of sulfite to sulfide. Although previous studies have predominantly highlighted electrostatic interactions between negatively-charged Fd and positively-charged SiR, the nature of intermolecular forces involved in complex formation and their relationship to SiR activity remain unclear.

I examined Fd:SiR complex formation and SiR activity over NaCl concentrations between 0 and 400 mM with considering physiological conditions. Fd-dependent SiR activity assays and Michaelis-Menten kinetics revealed a bell-shaped activity curve with a maximum around 40-70 mM NaCl and a reverse bell-shaped dependence of affinity (Michaelis constant). Meanwhile, intrinsic SiR activity, as measured in a methyl viologen-dependent assay, exhibited saturation above 100 mM NaCl. Thus, two assays suggested that interprotein interaction is crucial in controlling Fd-dependent SiR activity.

Calorimetric analyses showed the monotonic increase in the dissociation constant on increasing NaCl concentrations, distinguished from the biphasic change in the Michaelis constant. The results further revealed that Fd:SiR complex formation and interprotein affinity were thermodynamically adjusted by both enthalpy and entropy through electrostatic and non-electrostatic interactions. A residue-based NMR investigation on addition of SiR to ^{15}N-labeled Fd also demonstrated that a combination of both non-covalent forces stabilized the complex with similar interfaces and modulated binding affinity and mode depending on NaCl concentrations.

These findings elucidate that non-electrostatic forces are also essential for complex formation and modulation. I suggest that a complex configuration optimized for maximum enzymatic activity near physiological conditions is achieved by structural rearrangement through controlled non-covalent interprotein interactions.

Introduction

The intermolecular interactions between proteins and various partner molecules such as biomolecules including other proteins, nucleic acids and small ligands or metal ions play essential roles in numerous cellular and biological processes, such as electron transfer, signal transduction, and protein homeostasis. (13,19,20,46,51-58)

Native-state proteins function with their unique three dimensional structures, achieved by folding reactions, whereas intrinsically disordered proteins function without specific conformations (59,60). The physicochemical and structural properties of the surfaces and active sites of folded proteins are the result of protein evolution with a high interior packing density and local functional flexibility (61-63). These characteristics are important physical and chemical determinants that effectively control enzymatic activity in a given environment. The properties of protein surfaces are a critical factor in ensuring appropriate interprotein contacts for function. A statistical study previously showed that the interfaces of protein-protein complexes consisted of 57% apolar residues, 19% charged residues, and 24% polar residues (23). This finding suggests that proteins utilize these surface properties and that non-covalent interactions, electrostatic and non-electrostatic interactions, are indispensable in intermolecular forces.

Non-electrostatic interactions including polar and hydrophobic interactions have been shown to contribute to complex formation of proteins with other molecules. Proteins that accommodate hydrophobic cavities form complexes with hydrophobic molecules. Examples include the binding of GroEL with unfolded proteins for cellular homeostasis (64) and that of LPGDS to lipophilic compounds for cell differentiation (58). The molecular recognition of proline residues of partner proteins by the SH3 domain has also been attributed to non-electrostatic forces (65). Interactions between DNA-binding proteins and the minor grooves of DNA are also known to be mostly hydrophobic in nature (20).

One of the most well-known electrostatic interactions is the attractive charge-charge interaction between positively-charged proteins and the negatively-charged major grooves of DNA (20). The repulsive interprotein electrostatic interactions between the same charges play a role in suppressing protein aggregation, which often leads to the deactivation of enzymes and disruption of homeostasis, due to decreases in protein solubility (66).

Biochemical data obtained from site-directed mutagenesis, rates of electron transfer or enzymatic activity, and biophysical approaches including X-ray crystallography and NMR spectroscopy suggested that most redox proteins involved in electron transfer reactions show localized surface charged patches and utilize predominantly attractive electrostatic interactions to form an electron transfer complex formation. Cytochrome *c* (cyt*c*), which possesses a localized patch of positively-charged residues on its surface, forms a complex with the negatively-charged surface of subunit II of cytochrome *c* oxidase (31,67,68) or cytochrome *c* peroxidase (C*c*P) in order for intermolecular electron transport to occur (69). Cytochrome *f* also interacts with plastocyanin (PC) for electron flux by means of the oppositely-charged residues of individual proteins (43,70). Nitrite reductase (NiR) (14,56) and [Fe-Fe] hydrogenase (50), which possess positively-charged surface patches, form complexes with ferredoxin (Fd), which possesses corresponding negatively-charged patches. I previously showed that the negative surfaces of Fd also show complementary electrostatic networks with the positively-charged surfaces of ferredoxin-NADP($^+$) reductase (FNR) in the crystal structure of their complex (11). Disruption in intermolecular electrostatic interactions, due to the change in ionic strength or deletion of charges by mutation, often affects electron transfer rate, enzymatic activity, and binding affinity (4,14,43,44,46,47,50,70,71), clearly indicating that electrostatic interactions are important in forming redox protein complexes.

On the other hand, distinct patterns of the electron transfer rate have been observed on increasing ionic strength. For instances, while the overall electron transfer rate from cyt*c-555* (72) or cyt*c* to PC decreases monophasically (73), that from cyt*c* to C*c*P (73) or from Cytochrome *f* to PC shows decreases in the electron transfer rate following increases in the rate (43,72-74). The similar biphasic change was also observed in the electron transfer between *Anabaena* Fd, flavodoxin, FNR, and PSI (27,28,30,32,67). Changes in hydrophobicity on the interfaces of FNR influenced the rate of electron transfers from Fd or flavodoxin (28,32). Remarkably, I have recently revealed that enhancement of Fd interfacial hydrophobicity increased and decreased the electron transfer rate to FNR and sulfite reductase (SiR), respectively (22). Hydrophobic interactions at interfaces of encounter complexes have shown to play a central role in searching a final active complex conformation for electron transfer (38,39,75).

These findings have suggested that the electrostatic interaction alone is not enough to

explain all these changes (27,28,30,32,38,39,43,46,63,74-76) and raise many key questions about the relative contribution of non-covalent forces such as electrostatic and hydrophobic interactions during formation of different productive electron transfer complexes. Furthermore, information regarding the relationship between complex formation and enzymatic activity remains limited. Therefore, in order to address these issues in detail, I selected model redox proteins, the enzyme SiR and its physiological electron donor protein Fd, both derived from the maize leaf.

SiR sequentially receives six electrons from the one electron carrier Fd through the repeated formation and dissociation of the Fd:SiR complex, using these electrons to reduce sulfite to sulfide. I previously demonstrated the importance of electrostatic interactions between negatively-charged side chains on Fd and positively-charged side chains on SiR for complex formation and SiR activity (2-4). Mutagenic neutralization of negative charges of Fd on the putative interfaces of complex formation with SiR decreased binding ability of Fd, and SiR activity (2,4).

I herein performed in-depth biochemical and biophysical studies on the role of electrostatic and non-electrostatic forces in interprotein interactions between SiR and Fd, and how both non-covalent forces controlled SiR activity. I performed the two distinct SiR activity assays to differentiate influence of interprotein interactions of Fd on SiR activity from intrinsic SiR intramolecular activity, thermodynamic characterization of complex formation by calorimetry at the molecular level, and residue-based NMR spectroscopy of ^{15}N-labeled Fd to examine the binding site and mode at various NaCl concentrations.

The results obtained demonstrated that SiR activity was controlled by interprotein interactions with Fd and that both electrostatic and non-electrostatic interactions were thermodynamically and mechanically important for the formation and modulation of the Fd:SiR complex. I propose that an optimized productive complex for maximum SiR activity near physiological conditions is dependent on fine-tuning of non-covalent forces for conformational gating of electron transfer. I further show the concise schematic model on how SiR interacts with Fd and modulates its activity against saline perturbations by distinguishing non-productive physical binding.

Materials and methods

Enzymatic activity assay

Fd- and methyl viologen (MV)-dependent SiR activities were assayed using a reconstituted electron transfer system that resulted in the production of cysteine. The reaction mixture containing Fd (0-40 μM) or MV (1 mM), SiR (200 nM), sodium sulfite (2 mM), O-acetyl serine (10 mM), and cysteine synthase (0.4 U) in 50 mM Tris-HCl buffer (pH 7.5) was prepared at various NaCl concentrations from 0 to 400 mM at 30 ℃.

SiR reduction was initiated by an intermolecular electron transfer from Fd, which was reduced by $Na_2S_2O_4$. Reduced SiR sequentially converted sulfite to sulfide. Cysteine synthase, in the presence of O-acetyl serine, produced cysteine from sulfide. The reaction was stopped in 3 min after reducing SiR by the addition of trichloroacetic acid at a final concentration of 20% (volume/volume). The solution was promptly centrifuged at 15,000 rpm for 3 min and 150 μl of the supernatant was collected. After adding 150 μl acetic acid and 150 μl acid-ninhydrin reagent to the supernatant, the solution was heated at 95 ℃ for 10 min. The further addition of 450 μl ethanol to the solution allowed the production of cysteine to be monitored by increases in absorption intensity at 546 nm.

In order to calculate the Michaelis constant (K_m) and turnover number (k_{cat}), data obtained at the various concentration of Fd (0, 1, 2, 4, 6, 10, 20, and 40 μM) and NaCl (0, 25, 50, 75, 100, 200, 300, and 400 mM) were fit to the following Michaelis-Menten equation:

$$v = \frac{k_{cat}[\mathrm{SiR}]_0[\mathrm{Fd}]}{[\mathrm{Fd}] + K_m} \qquad \text{Equation 5}$$

where v indicates the initial velocity of the catalytic reaction of SiR, and $[SiR]_0$ and [Fd] indicate the concentrations of total SiR and free Fd in the reaction mixture, respectively.

Isothermal titration calorimetry

The isothermal calorimetric titration of Fd to SiR in 50 mM Tris-HCl buffer (pH 7.5) containing NaCl in the range of 0-400 mM (0, 25, 50, 75, 100, and 400 mM) was conducted using a VP-ITC instrument (Malvern, UK) at 30 ℃ or 25 ℃ and 27.5 ℃ at 100 mM NaCl. Binding reactions were initiated by adding Fd (0.85-2 mM) in a syringe to SiR (15-70 μM) in

the cell at each NaCl concentration. The titration of Fd comprised 38 injections with a spacing time of 300 s and stirring speed of 307 rpm. The injection volume was 2 or 7 μL for each injection. The corresponding heat of the dilution of Fd titrated to the buffer was used to correct data. Binding isotherms were analyzed with the theoretical curve (equation 1 in chapter III). Based on non-linear fitting to equation 1 (chapter III), the values of n, ΔH_{bind}, and K_d were obtained. Changes in Gibbs free energy (ΔG_{bind}) and entropy (ΔS_{bind}) of binding were calculated by using the known values of H_{bind}, and K_d and the thermodynamic relationships in equations 2 and 3.

Circular dichroism measurements

Far-UV circular dichroism (CD) measurements of 3 μM (0.2 mg ml^{-1}) were carried out in 50 mM Tris-HCl buffer (pH 7.5) containing NaCl ranging from 0 to 400 mM at 25 °C. Heat scanning of SiR from 20 to 90 °C was also performed under the same solvent condition to the wavelength scanning by monitoring CD signals at 220 nm at a rate of 1 °C per minute. The apparent melting temperature (T_m) was determined by a regression analysis using a nonlinear least squares fitting of data to the sigmoidal equation under the assumption of a two-state transition between folded and unfolded states. It should be noted that I performed the thermodynamic analysis although thermal unfolding of SiR was irreversible.

$$S = ((S_F + m_F T) + (S_U + m_U T)\, e^{-(\Delta H\text{global}(1 - T/T\text{m}) - \Delta C\text{p,global}((T\text{m} - T) + T\ln(T/T\text{m})))/RT}) / (1 + e^{-(\Delta H\text{global}(1 - T/T\text{m}) - \Delta C\text{p,global}((T\text{m} - T) + T\ln(T/T\text{m})))/RT}) \quad \text{Equation 6}$$

where S is the signal intensity monitored by CD, S_F and S_U are intensities of folded and unfolded SiRs, respectively. T, T_m, and R indicate temperature, the midpoint temperature of denaturation, and gas constant, respectively. The change in enthalpy for global unfolding of SiR is represented by ΔH_{global} and the change in heat capacity is shown with $\Delta C_{p,global}$. The initial and final baseline was described by $S_F + m_F T$ and $S_U + m_U T$, respectively. CD measurements were performed with a J-720 spectropolarimeter (Jasco, Japan) using a cell with a light path of 1 mm. CD signals between 195 and 250 nm were expressed as the mean residue ellipticity [θ] (deg cm^2 $dmol^{-1}$). Temperature was regulated using a PTC-423L Peltier-unit (Jasco, Japan).

NMR measurements

Two-dimensional ^{1}H-^{15}N heteronuclear single-quantum coherence correlation (HSQC) spectra of ^{15}N uniformly-labeled Fd with and without SiR were obtained using an AVANCE II-800 spectrometer equipped with a cryogenic probe (Bruker, Germany) in 50 mM Tris-HCl buffer (pH 7.4) containing 10% D_2O and the desired concentrations of NaCl at 25 °C. The protein concentrations for NMR measurements were 100 μM for Fd and 50 μM for SiR. Data were processed by NMRPipe (48) and analyzed by Sparky (49).

Chemical shift differences (CSD) in NMR peaks in the absence and presence of SiR were calculated for finite CSD analysis using equation 4 (chapter III). In order to calculate the chemical shift values of Fd, which was saturated by SiR, and to perform infinite CSD analysis, I used the relationship in equation 7 (77),

$$\delta_{obs} - \delta_{free} = ((\delta_{com} - \delta_{free})/[Fd]_t)\ ((K_d + [Fd]_t + [SiR]_t)/2) - ((\delta_{com} - \delta_{free})/[Fd]_t)\ (((K_d + [Fd]_t + [SiR]_t)^2 - 4[Fd]_t[SiR]_t)^{1/2}/2) \quad \text{Equation 7}$$

where δ_{free} and δ_{obs} indicate the chemical shifts of Fd in the free form and in the presence of SiR, respectively. δ_{com} represents the chemical shifts of Fd in the presence of an infinite amount of SiR. The total concentrations of Fd and SiR are represented by $[Fd]_t$ and $[SiR]_t$, respectively.

Principal component analysis of chemical shift perturbation

Principal component analysis (PCA) was performed using the change in chemical shifts obtained from the infinity CSD analysis at each NaCl concentration. The CSD data were represented as a single-row vector. Then, the vectors were used to build a two-dimensional matrix, in which the rows were the infinite CSD data and the columns were the variables of the NaCl concentration. The matrix size was 78 traceable residues and 5 different NaCl concentrations (0, 25, 50, 75, and 100 mM). The CSD data of each residue were normalized using the mean-centering and variance-scaling. PCA was carried out using the R statistics platform (R Foundation for Statistical Computing, http://www.r-project.org). The obtained eigenvalues were expressed as contribution ratios for individual principal components (PC1 and PC2).

Results

NaCl concentration-dependent changes in SiR activity

SiR activity in the range of NaCl concentrations from 0 to 400 mM (0, 25, 50, 75, 100, 200, 300, and 400 mM) was measured with two distinct assays, which differed in the electron donor to SiR: either Fd or MV, i.e., Fd- and MV-dependent SiR activity assays (Fig. 4-1A, B).

SiR activity was first examined using the Fd-dependent assay with a fixed concentration of SiR and Fd (Fig. 4-1A). SiR showed relatively high activity even in the absence of NaCl, and increased in activity with rising NaCl concentrations up to 50 mM. Further elevation of NaCl concentration decreased SiR activity. The activity at 100 mM NaCl was roughly similar to that at 0 mM NaCl. Further increase to higher NaCl concentrations significantly decreased activity. At 400 mM NaCl, 10-fold lower activity than that at 50 mM NaCl was observed. For more detailed information, I performed a fit using a Gaussian function, demonstrated a NaCl concentration for maximum activity and symmetric dependence of activity to the NaCl concentration. The best-fit result indicated that the NaCl concentration at which SiR has maximum activity is approximately 40 mM (Table 4-1).

Next, the MV-dependent SiR activity assay was performed at the same NaCl concentrations (Fig. 4-1B). SiR showed appreciable activity at all of the NaCl concentrations examined. By increasing NaCl concentrations from 0 to 400 mM, SiR activity increased progressively and was saturated at approximately 100 mM NaCl. Saturated SiR activity was more than two-fold higher than in the absence of NaCl.

Michaelis-Menten kinetics were investigated by varying the concentration of Fd with a fixed SiR concentration (Fig. 4-1C). Regardless of the NaCl concentration, increased Fd concentrations increased the v value of SiR. However, maximum v increased then decreased with increasing NaCl concentration, as shown in the v_{max} value (Table 4-1). The NaCl concentration with highest v_{max} was best fit to approximately 63 mM. Similarly, k_{cat} increased with increasing NaCl concentration to 50-75 mM NaCl, while further increase in NaCl resulted in decreased k_{cat} (Fig. 4-1D). Fitting results revealed that k_{cat} was maximal at approximately 66 mM NaCl (Table 4-1). K_m of SiR for Fd also showed NaCl concentration dependence. The value of K_m decreased from 0 to 100 mM NaCl and increased as NaCl concentrations rose

above 100 mM (Fig. 4-1D). A minimum K_m value was best fit to approximately 76 mM NaCl. The catalytic efficiency, k_{cat}/K_m, also showed a similar salt concentration dependent profile to that of v_{max} and k_{cat}, with a maximum at approximately 63 mM NaCl (Table 4-1).

Thermodynamic investigation of interprotein interactions between Fd and SiR by isothermal titration calorimetry

To obtain information on underlying thermodynamic contribution to binding between Fd and SiR, I carried out an energetic investigation using isothermal titration calorimetry (ITC) at various NaCl concentrations (0, 25, 50, 75, 100, and 400 mM) and 30 °C (Fig. 4-2).

During titration of increasing Fd to SiR, exothermic ITC peaks in thermograms, derived from formation of the Fd:SiR complex, were observed at NaCl concentrations between 0 and 100 mM (Fig. 4-2A, upper panels). ITC thermograms at each NaCl concentration except 400 mM showed the decreased magnitude in the negative ITC peaks with consecutive titration of Fd. At the higher molar ratio of Fd to SiR, the ITC peak intensity reached the level of dilution and mixing heat, which indicated the completion of binding reactions. At 400 mM NaCl, the apparent heat of binding was too small to be observed.

Analysis of the ITC thermogram and isotherm using the fit and theoretical equations (Fig. 4-2A, lower panels) revealed the underlying thermodynamic parameters for Fd:SiR complex formation: change in enthalpy (ΔH_{bind}), entropy (ΔS_{bind}), and free energy (ΔG_{bind}) as well as the dissociation constant (K_d) with binding stoichiometry (n) (Table 2). The biphasic binding isotherm in the absence of NaCl was best fit by a model with two interacting sites which have different binding affinity, revealing the distinct thermodynamic parameters (Fig. 2A, left upper).

ΔH_{bind} values obtained at the other NaCl concentrations were all negative and their magnitudes decreased from -4.2 to -0.8 kcal mol^{-1} with increasing the NaCl concentration (Fig. 2*B*). On the other hand, all ΔS_{bind} values were positive with relatively small differences (-0.7 kcal mol^{-1}) being observed. The binding affinity between Fd and SiR gradually became weaker with increases in the concentration of NaCl because K_d exponentially increased (Fig. 4-1D) and, accordingly, ΔG_{bind} decreased monotonically in magnitude from -8.3 to -6.6 kcal mol^{-1} (Fig. 4-2B).

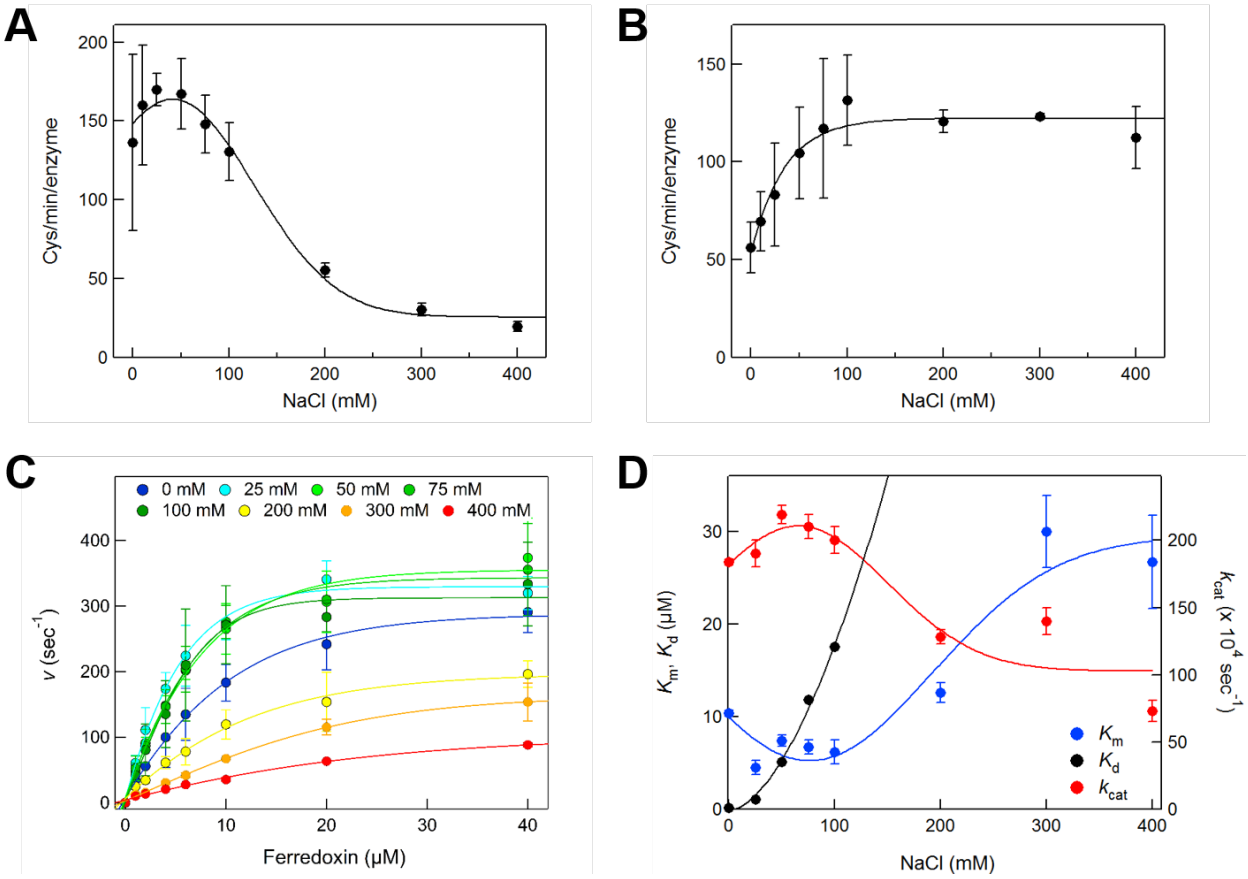

Fig 4-1. NaCl-concentration dependent SiR activity monitored by distinct activity assays. (A, B) SiR activity obtained by Fd- (A) and MV-dependent activity assay (B) was plotted against the NaCl concentration. The continuous curves were obtained by fitting to Gaussian (A) and single exponential equations (B) to show symmetric and saturating profiles, respectively. (C) The steady-state kinetics of SiR activity obtained at the various NaCl concentrations were plotted as a function of the concentration of Fd. The continuous lines show the curves fitted based on the Michaelis-Menten equation. The error bars were averaged values of the three independent measurements. (D) K_m in the left axis (red) and k_{cat} in the right axis (blue) respectively were obtained from Michaelis-Menten kinetics and plotted against the concentration of NaCl. The continuous curves were obtained by fitting to the Gaussian equation. K_d values (black) obtained from ITC measurements in the left axis were also plotted. The solid line for K_d is drawn as a visual aid. E, v_{max} in the left axis (red) and k_{cat}/K_m in the right axis (blue) were plotted against the concentration of NaCl, respectively. The continuous curves were obtained by fitting to the Gaussian equation.

Table 4-1. Summary of SiR activity obtained by Michaelis-Menten kinetics.

NaCl (mM)	v_{max}[a] (μM sec^{-1})	k_{cat}[a] ($\times 10^4$ sec^{-1})	K_m[a] (μM)	k_{cat}/K_m ($\times 10^4$ sec^{-1} μM^{-1})
0	368 ± 5	184 ± 2	10.4 ± 0.3	17.6 ± 0.6
25	390 ± 20	190 ± 10	4.5 ± 0.8	43 ± 8
50	440 ± 10	219 ± 7	7.4 ± 0.6	30 ± 3
75	420 ± 20	210 ± 9	6.7 ± 0.8	32 ± 4
100	390 ± 30	200 ± 10	6.2 ± 1.3	32 ± 7
200	260 ± 10	128 ± 5	12.6 ± 1.1	10 ± 1
300	270 ± 20	140 ± 10	29.9 ± 3.9	4.6 ± 0.7
400	150 ± 20	73 ± 8	26.7 ± 5.0	2.7 ± 0.6
Maximum concentration[b]	62.5 mM (41.3 mM[c])	65.6 mM	76.1 mM	62.5 mM

[a] v_{max}, k_{cat}, and K_m were calculated by fitting the averaged values of the three independent measurements to the equation 5 (see Materials and Methods).

[b] The NaCl concentration at which a value was maximum with a Gaussian fitting.

[c] The NaCl concentration at which Fd-dependent SiR activity was maximum.

Although I cannot exclude the possibility that variation between K_d and K_m was caused by technical differences between ITC and enzyme assays, it is more likely that these differences arise from the fact that K_d values obtained from ITC report all physical binding reactions, including productive and non-productive complex formation, while K_m values obtained from Michaelis-Menten kinetics reflect the affinity of the only productive complex resulting in enzyme activity.

ITC measurements at distinct temperatures (25 and 27.5 °C) were further performed in the presence of 100 mM NaCl (Fig. 4-3). A series of negative ITC peaks representing exothermic reactions were observed at both temperatures (Fig. 4-3A, B). Decreasing the temperature from 30 to 27.5 and 25 °C, resulted in slight increases and decreases respectively in the negative values for ΔH_{bind} and $-T\Delta S_{bind}$ (Fig. 4-3C and Table 4-2). Thus, the temperature dependence of ΔH_{bind} and $-T\Delta S_{bind}$ weakened interprotein affinity on decreasing temperature by showing the decrease in the magnitude of ΔG_{bind} from -6.6 kcal mol^{-1} at 30 °C to -6.0 kcal mol^{-1} at 25 °C.

At all NaCl concentrations and temperatures, except for 0 mM NaCl at 30 °C, the *n* value was approximately 1, which suggested a 1-to-1 binding stoichiometry between Fd and SiR in solution. However, in the absence of NaCl, the high binding affinity site at a molar ratio ([Fd]/[SiR]) lower than ~2 showed an *n* value of approximately 1 and the low binding affinity site at higher molar ratios from ~2 to ~8 indicated an *n* value of ~4.

Changes in static structures and global dynamics of SiR at various NaCl concentrations examined by far-UV CD spectroscopy

In order to investigate changes in the static and dynamic structures of SiR in the presence of NaCl, far-UV CD measurements were performed at various NaCl concentrations (Fig. 4-4). Static conformations of SiR were first investigated at the level of secondary structure. The results obtained in the far-UV region without NaCl show the characteristic spectra of a mixture of α-helical and β-strand structures with minima at 210 and 220 nm (Fig. 4-4A). A series of far-UV CD spectra of SiR were obtained at various NaCl concentrations to further characterize the change in the structure of SiR. No change was observed in the pattern of CD spectra, indicating that NaCl does not perturb the secondary structure of SiR.

Sub-global and global dynamics between folded and unfolded conformations without

NaCl were examined by observing CD spectra with increasing temperature from 20 to 90 °C (Fig. 4-4B, C). The magnitude of whole CD signals decreased with increases in the temperature from approximately 35 °C and were saturated from approximately 70 °C (Fig. 4-4B) indicating cooperative global unfolding (Fig. 4C). The CD spectrum at 90 °C exhibited no characteristic profile with low CD intensity even in the presence of NaCl (Fig. 4-4A, B), indicating the thermally-unfolded state of SiR. The conformational transition was best fit by a two-state transition model of the global dynamics of SiR, without recognizable sub-global dynamics, producing a melting temperature (T_m) of 55.1 °C and an enthalpy change for global unfolding (ΔH_{global}) of approximately 290 kcal mol^{-1} (Table 4-3). The addition of NaCl increased cooperativity of the two-state thermal transition which increased the magnitude of ΔH_{global} (Table 4-3) and the transition curve was gradually shifted to a higher temperature with increases in the concentration of NaCl (Fig. 4-4C).

Residue-based investigation of NaCl concentration-dependent interprotein interactions by solution-state NMR spectroscopy

A detailed NMR study of SiR in solution remains difficult due to its large size (~65 kDa), which causes severe peak broadening and overlapping. Therefore, solution-state NMR spectroscopy of the ^{1}H-^{15}N HSQC was performed on the smaller Fd protein (~10.5 kDa) in the absence and presence of SiR at various NaCl concentrations (Fig. 4-5). To maximize detection level, concentrations above 100 mM NaCl were not used, as this decreases sensitivity when using a cryogenic probe. The most dynamic changes in SiR activity were observed in the range of 0-100 mM NaCl as shown in SiR activity assays (Fig. 4-1). Thus, I selected NaCl concentrations ranging from 0 to 100 mM (0, 25, 50, 75, and 100 mM NaCl).

Sharp NMR signals of ^{15}N-labeled Fd alone were well distributed in ^{1}H-^{15}N HSQC spectra at all NaCl concentrations examined (Fig. 4-5A) indicating that NaCl does not disturb the structural integrity of native Fd. I then recorded the ^{1}H-^{15}N HSQC spectra of ^{15}N-labeled Fd in the presence of SiR at each NaCl concentration. I selected a molar ratio between Fd/SiR of 2:1. This allowed me to promptly detect NaCl concentration-dependent changes in interprotein affinity at the residue level by escaping severe peak broadening as would be observed in the presence of excess amounts of SiR. Large molecular weights such as that of the Fd:SiR complex, decrease the sensitivity and resolution of NMR peaks. Many Fd peaks

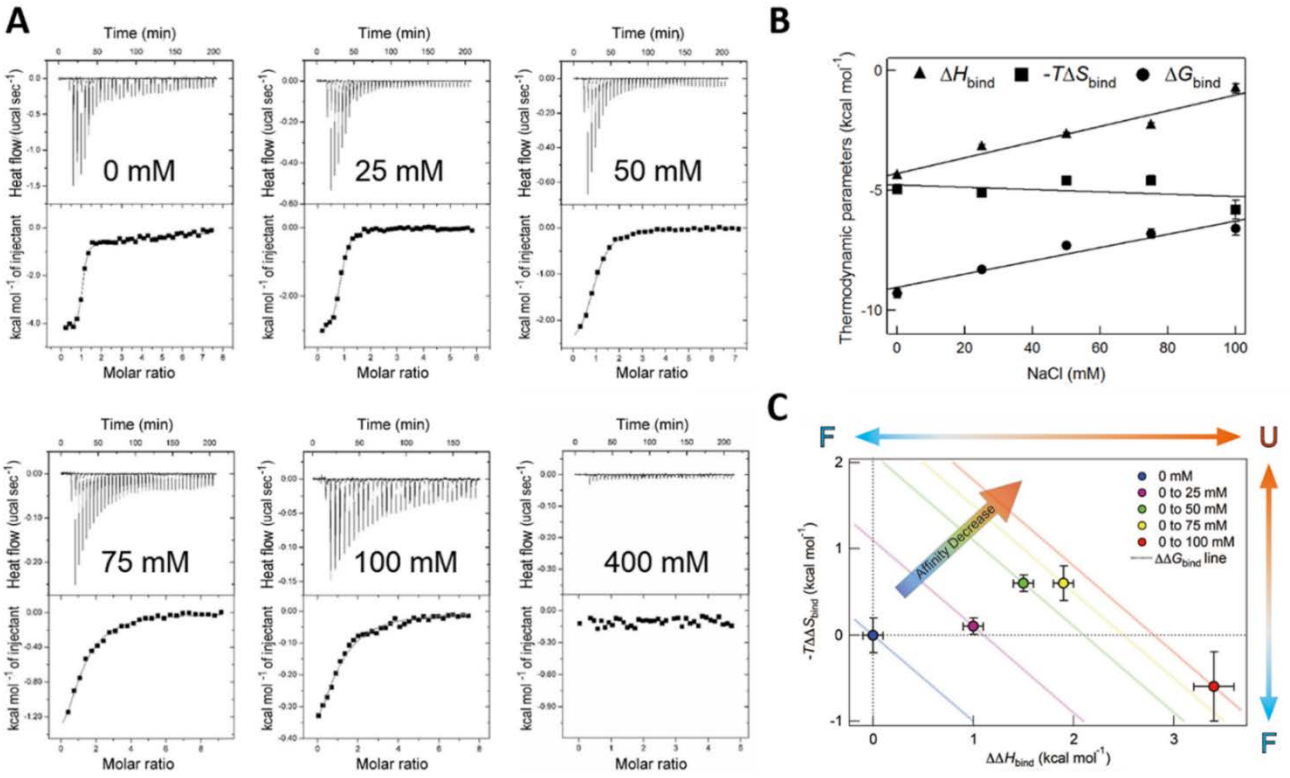

Fig 4-2. Thermodynamic characterization of binding reactions between Fd and SiR using ITC analysis and driving force plot.

(A) ITC thermograms of the titration of Fd to SiR at 0, 25, 50, 75, 100, and 400 mM NaCl at 30 °C are shown in the upper panel. Normalized heat values were plotted against the molar ratio ([Fd]/[SiR]) in the lower panel. Fitted curves are exhibited using continuous lines. (B, C) The values of ΔH_{bind} (triangle), $-T\Delta S_{bind}$ (rectangle), and ΔG_{bind} (sphere) were plotted as a function of the NaCl concentration (B) and temperature C, All of the solid lines indicate the fitting curve with the straight line. *D*, The driving force plot which describes the change in the driving force (ΔH_{bind} and $-T\Delta S_{bind}$) and ΔG_{bind} value following complex formation at each NaCl concentration are shown. The dotted diagonal lines with various colors signify the $\Delta\Delta G_{bind}$ lines of 0 kcal mol^{-1} for 0 mM NaCl (blue), 1.1 kcal mol^{-1} for 25 mM NaCl (magenta), 2.1 kcal mol^{-1} for 50 mM NaCl (green), 2.5 kcal mol^{-1} for 75 mM NaCl (yellow), and 2.8 kcal mol^{-1} for 100 mM NaCl (red). Thermodynamically favorable (F) and unfavorable (U) directions following change in NaCl concentration are indicated by blue arrows and red arrows, respectively, outside the panel. The colored arrow in the panel indicates decreases in affinity.

Table 4-2. Summary of thermodynamic parameters of the Fd:SiR complex formation obtained by ITC.

Temperature	NaCl (mM)	ΔH_{bind} (kcal mol^{-1})	$-T\Delta S_{bind}$ (kcal mol^{-1})	ΔG_{bind} (kcal mol^{-1})	K_d (μM)	n
30 °C	0	-4.2 ± 0.1[a]	-5.2 ± 0.2[a]	-9.4 ± 0.2[a]	0.2 ± 0.1[a]	1.0[a]
		-1.2[b]	-4.4[b]	-5.6[b]	106[b]	4.2[b]
	25	-3.2 ± 0.1	-5.1 ± 0.1	-8.3 ± 0.1	1.1 ± 0.1	0.9
	50	-2.7 ± 0.1	-4.6 ± 0.1	-7.3 ± 0.1	5.1 ± 0.1	0.9
	75	-2.3 ± 0.1	-4.6 ± 0.2	-6.8 ± 0.2	11.8 ± 0.2	1.0
	100	-0.8 ± 0.2	-5.8 ± 0.4	-6.6 ± 0.3	17.6 ± 0.2	1.0
	400	n.d.[c]	n.d.[c]	n.d.[c]	n.d.[c]	n.d.[c]
27.5 °C	100	-0.7 ± 0.1	-5.8 ± 0.2	-6.5 ± 0.2	19.4 ± 0.1	1.0
25 °C	100	-0.7 ± 0.0	-5.4 ± 0.4	-6.1 ± 0.4	42.9 ± 0.0	0.9

[a]Thermodynamic parameters for a high affinity binding site. [b]Thermodynamic parameters for a low affinity binding site. [c]"n.d." is shown in cases, in which heat is too small to be detected.

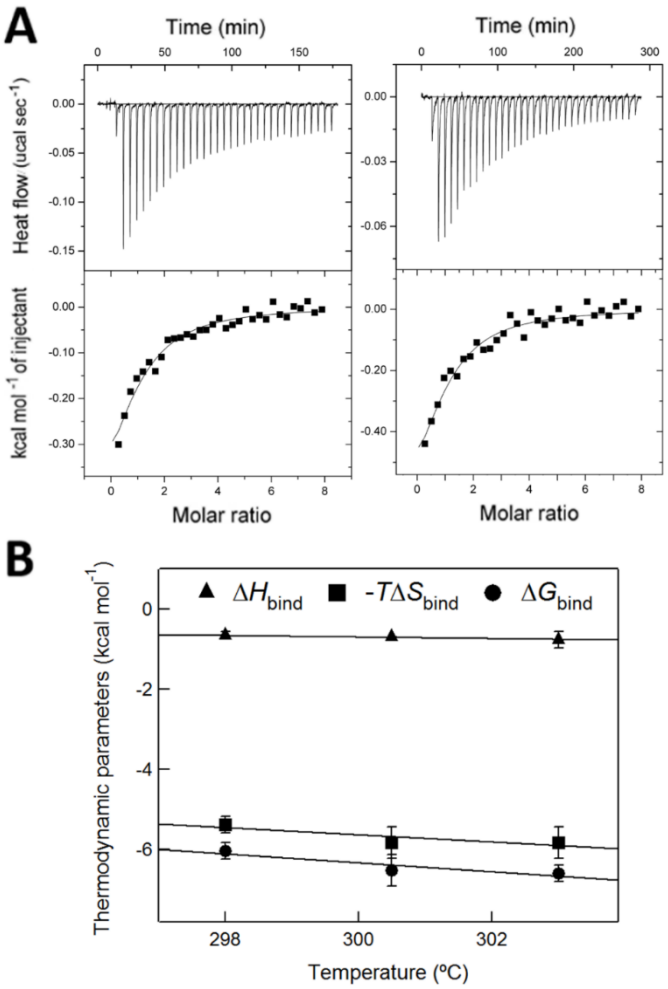

Fig 4-3. ITC measurements of Fd binding with SiR at distinct temperature.

(A) ITC thermograms of the titration of Fd to SiR in the presence of 100 mM NaCl at 25 (left) and 27.5 °C (right) are shown in the upper panel. Normalized heat values were plotted against the molar ratio ([Fd]/[SiR]) in the lower panel. Fitted curves are exhibited using continuous lines. (B) Thermodynamic parameters obtained are plotted against temperature.

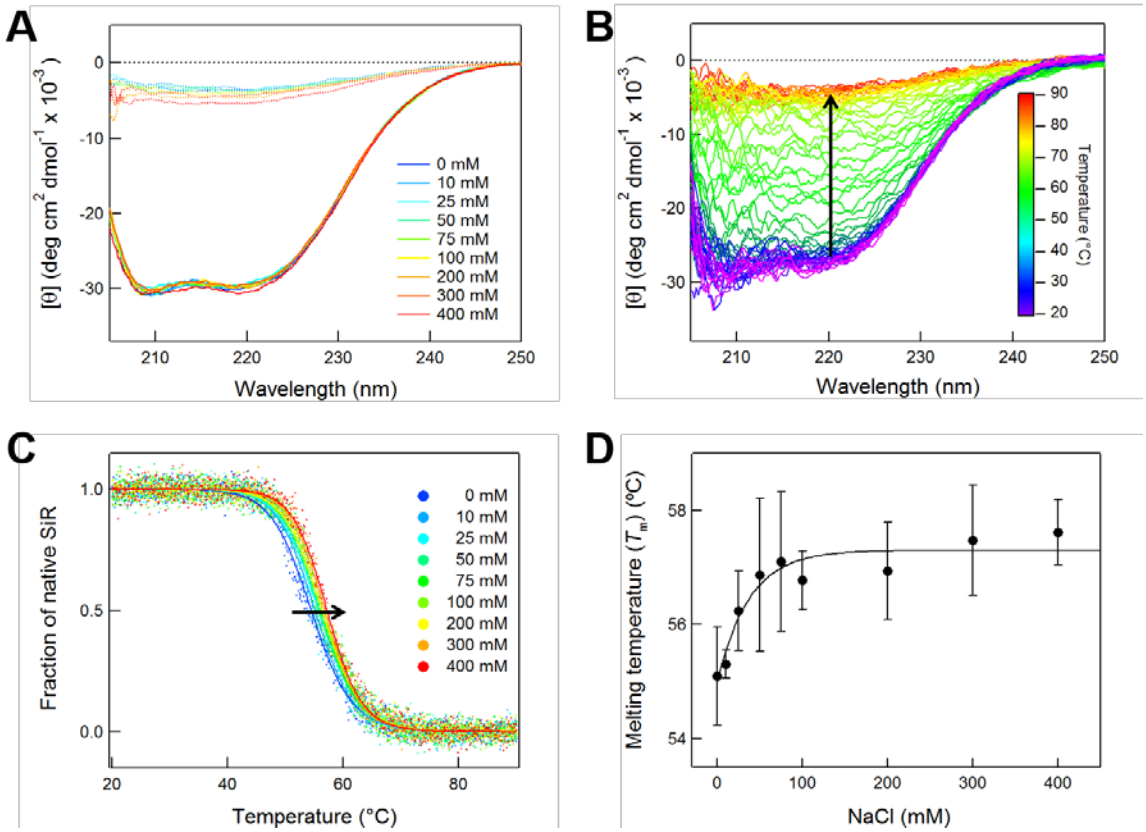

Fig 4-4. Global dynamics of SiR observed by the far-UV CD spectroscopy.

(A) The far-UV CD spectra obtained at 20 (solid line) and 90 °C (dotted line) are obtained with increasing NaCl concentrations from 0 to 400 mM. (B) The far-UV CD spectra of SiR without NaCl at various temperatures are shown with distinct colors. The increase in temperature from 20 to 90 °C is indicated by the arrow and changing color from magenta to red. (C) Thermal scanning of SiR represented by the fraction of folded native SiR using CD intensity at 222 nm is shown. The continuous curves indicate the fitted curve based on the theoretical equation (see Materials and Methods). The increase in the NaCl concentration was also guided by the arrow. D, The melting temperature (T_m) was plotted against the NaCl concentration. The continuous curve was obtained by fitting to single exponential equations giving a saturating profile.

Table 4-3. Summary of thermodynamic parameters for global dynamics of SiR observed by CD spectroscopy.

NaCl (mM)	T_m[a] (°C)	ΔH_{global}[b] (kcal mol^{-1})
0	55.1 ± 0.9	294 ± 38
10	55.3 ± 0.3	303 ± 31
25	56.2 ± 0.7	306 ± 43
50	56.9 ± 1.4	314 ± 40
75	57.1 ± 1.2	316 ± 38
100	56.8 ± 0.5	312 ± 44
200	57.0 ± 0.9	317 ± 37
300	57.5 ± 1.0	328 ± 30
400	57.6 ± 0.6	340 ± 40

[a]The averaged value with [b]standard deviation from two independent measurements are shown.

were shifted with the addition of SiR at 50 mM NaCl (Fig. 4-5A-C), which indicates perturbation of electromagnetic environments induced by the formation of a Fd:SiR complex. On decreasing the NaCl concentration from 100 to 0 mM, the degree of peak shifts decreased (Fig. 4-5A, inset), which suggests a decrease in the population of the Fd:FNR complex.

To obtain detailed quantitative and qualitative information, I calculated the chemical shift difference (CSD) (Fig. 4-5D, E) and mapped the residues onto a previously determined crystal structure of Fd (Fig. 4-6) (11). I used two CSD analyses: CSD of Fd in the presence of a half molar amount of SiR (Fig. 4-5D), here designated finite CSD analysis, and analysis with an infinite amount of SiR (Fig. 4-5*E*), designated infinite CSD analysis (see Materials and Methods). Finite CSD analysis provides easy evaluation of the Fd:SiR complex population and allows identification of key Fd residues for formation and regulation of a complex with SiR. On the other hand, infinite CSD analysis allows identification of the accurate binding interface of Fd, which is fully occupied with SiR, thereby revealing subtle differences in the binding modes.

Finite CSD analysis showed that both the number of residues with high CSD (over 0.02) and overall CSD values decreased with increasing NaCl concentrations, indicating weakened interprotein affinity. However, despite the decrease in amplitude of CSD, the identity of Fd residues showing CSD stayed basically the same (Fig. 4-5D). The binding interfaces for SiR were comparable to our previous studies (4). Residues showed a variety of changes in the degree of CSD depending on the NaCl concentration.

Mapping results from finite CSD analysis clarified that many negatively-charged Fd residues were perturbed in the presence of SiR and clustered as expected; however, polar and apolar residues also showed perturbations regardless of the NaCl concentration (Fig. 4-6A). The residues showing greatest CSD were mostly in the three parts of Fd, both terminal parts and the central part, along the Fd sequence, indicating that these regions of Fd are involved in complex formation with SiR: representatively E11 and E13 in the N-terminal parts, A28, E29, D34, L35, Y37, D60, and Y63 around the [2Fe-2S] cluster, and K91, E92-94, and T96 in the C-terminal part. Infinite CSD analysis (Fig. 4-5E) and mapping results (Fig. 4-6B) showed a similar pattern to that obtained with finite CSD analysis and binding interfaces with a higher degree of CSD compared to finite CSD analysis.

In order to obtain more information on the change in the binding interface between Fd

and SiR depending on the NaCl concentration, principal component analysis (PCA) was performed on the infinite CSD results since PCA is a useful statistical method and reduces a complex dataset to lower dimension to reveal hidden interrelationships among many objects. The two-dimensional PCA plot (PC1 vs. PC2) accounted for 77.1% of total variance (Fig. 4-5F), which indicated a high information content for the PCA plot. PC1 scores at 0, 25, 50, and 100 mM NaCl were clustered on the negative region around -2.5. However, the PC1 score of 75 mM NaCl was approximately 11 and positively contributed to the difference, indicating variance between 75 mM NaCl and all other NaCl concentrations (0, 25, 50, and 100 mM NaCl). On the one hand, the PC2 axis predominantly contained the variance information between either 50 mM or 100 mM NaCl and the other NaCl concentrations (0, 25, and 75 mM). PC2 scores at 0, 25, and 75 mM NaCl were clustered around zero whereas PC2 scores at 50 and 100 mM were around -8 (negative contribution) and 6 (positive contribution), respectively. Thus, the PCA plot reveals NaCl concentration-dependent changes in variance which provide NMR-based information on some differences at the binding interface of Fd and SiR.

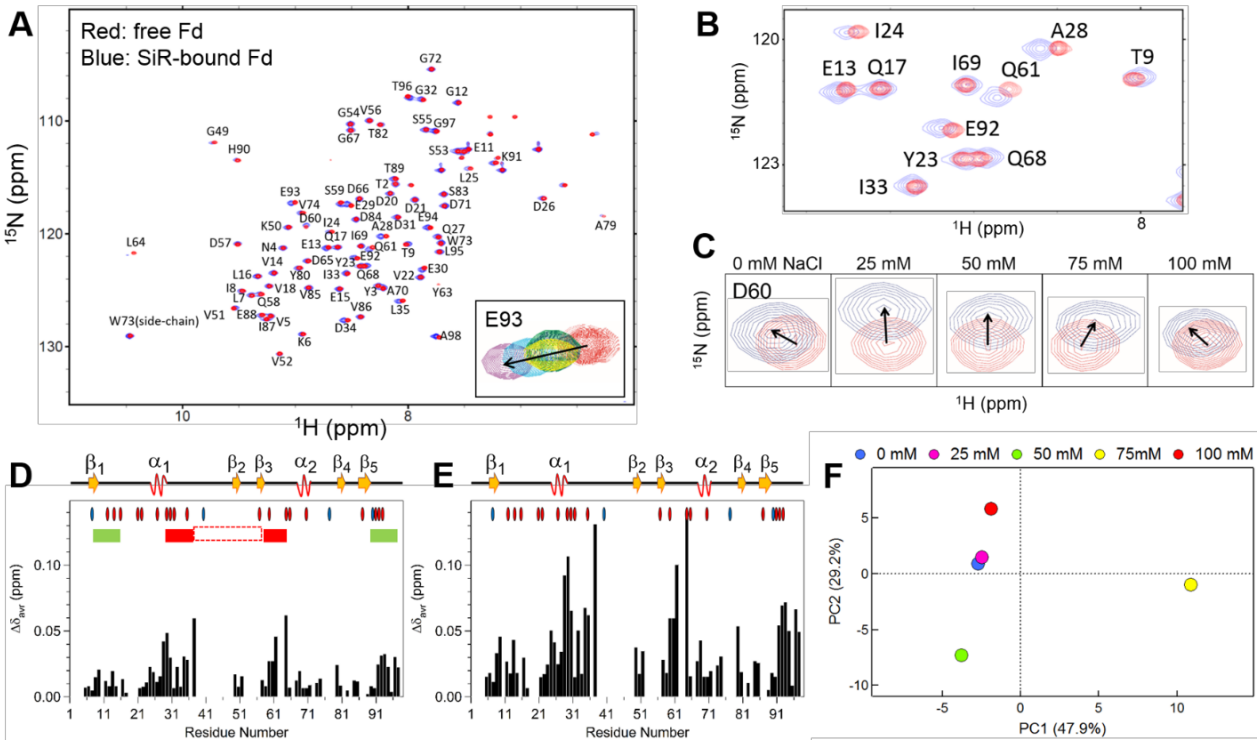

Fig 4-5. NMR spectroscopy of ^{15}N-labeled Fd with SiR and chemical shift perturbation analyses.

(A) The superposition of ^{1}H-^{15}N HSQC spectra of Fd with (blue) and without SiR (red) at 50 mM NaCl is shown. The peak shift of E93 of SiR-bound Fd depending on the NaCl concentration is shown in the inset: 0 (magenta), 25 (cyan), 50 (blue), 75 (yellow), and 100 mM (green). The increasing concentration of NaCl is indicated by the arrow. (B) Magnified central region of the spectra with dramatic perturbations. (C) Peak shifts of D60, which shows variable direction of NMR peak shift of Fd with (blue) and without SiR (red) depending on the concentration of NaCl. The concentration of NaCl is shown and the direction of the peak shift is indicated by black arrows. (D, E) Chemical shift difference (CSD) of Fd in the presence of SiR at 50 mM NaCl calculated by finite (D) and infinite CSD analyses (E) was plotted against the residue number. The secondary structure elements determined from the X-ray structure (PDB/1GAQ) (11) are displayed with labelling in the top part. α-helices (red coils) and β-

strands (yellow arrows) are shown. Negatively- and positively-charged residues are represented by red and blue ellipses, respectively. In D stabilizing and regulating regions are also shown with red and green bars, respectively. The red dotted rectangle indicates a putative stabilizing region, which is mostly invisible in NMR spectra due to paramagnetic relaxation enhancement. (F) Two-dimensional plot of principal component analysis (PCA) on the basis of the infinite CSD results obtained at 0 (blue), 25 (magenta), 50 (green), 75 (yellow), and 100 mM NaCl (red) is shown.

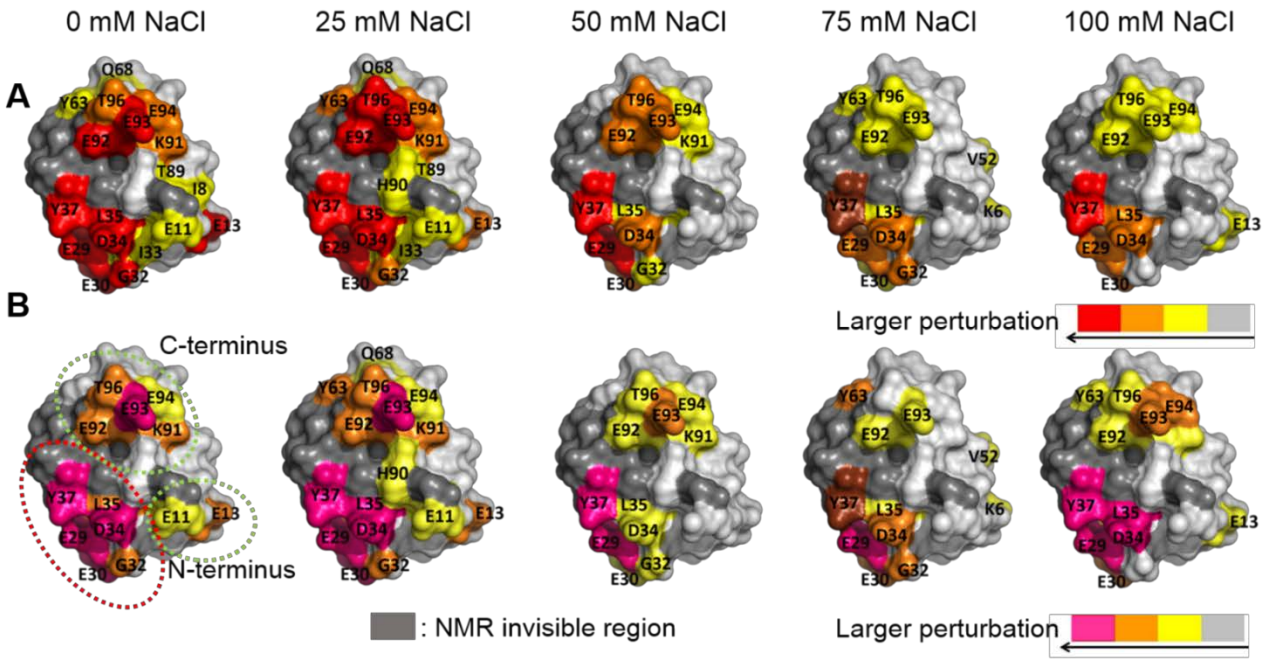

Fig 4-6. Mapping of interacting residues of Fd for SiR onto the crystal structure of Fd.
(A, B) The degree of the chemical shift difference (CSD) by means of finite (A) and infinite CSD analyses (B) at each NaCl concentration was mapped onto the crystal structure of Fd (PDB ID: 1GAQ) (11). The color code for the finite CSD analysis is as follows: Red, CSD > 0.04; orange, 0.04 > CSD > 0.03; yellow, 0.03 > CSD > 0.02. The color code for the infinite CSD analysis is as follows: Pink, CSD > 0.08; orange, 0.08 > CSD > 0.06; yellow, 0.06 > CSD > 0.04. The NMR invisible peaks (due to paramagnetic relaxation enhancement) are shown by dark gray. Stabilizing and regulating regions are shown with red and green dotted lines, respectively. The stabilizing region includes putative stabilizing residues which are not visible in NMR.

Discussion

Interprotein interaction-governed Fd-dependent SiR activity over the intrinsic activity power of SiR

Enzymatic activity is largely controlled by intermolecular interactions between binding partners and the intramolecular catalytic capacity of the enzyme itself. I dissected these two contributions to understand overall activity of SiR by using two types of SiR activity assays: the Fd-dependent assay, which can evaluate the effects of interprotein interactions between the SiR and its physiological electron donor Fd, and the MV-dependent assay, which reflects the intrinsic catalytic capability of SiR since electron transfer to SiR by excessive amounts of MV is not limited by intermolecular interactions.

The shape of electron-transferring rate curves plotted against ionic strength has been used to interpret the degree of control exerted on catalytic rate by interprotien interaction (27,28,30,32,43,67,71-74). A bell-shaped curve suggested rearrangement of electron-transfer protein complexes, from an initial complex including the encounter complex to final configuration (i.e., conformational gating for the electron transfer thorough two-step binding), while a monotonically-decreasing curve indicated the absence of the conformational rearrangement of complexes. Thus, a bell-shaped Fd-dependent SiR activity profile over NaCl concentrations (Fig. 4-1A, D) demonstrated that the contribution of interprotein interactions between Fd and SiR to overall SiR activity is considerable.

The impact of SiR structural dynamics on its intrinsic enzymatic capacity at various NaCl concentration was characterized. A saturating curve of SiR activity, obtained by the MV-dependent assay, was consistent with a NaCl concentration dependence of T_m (Fig. 4-4D). This indicated that the increase in the intrinsic activity of SiR may be related to the suppression of global dynamics, possibly due to NaCl-induced molecular compaction without an overall change in secondary structure (Fig. 4-4A), by increasing T_m and the magnitude of negative ΔH_{global} (Table 4-3). Although we consider it unlikely, I cannot exclude the possibility that NaCl also influenced the redox potentials of the [4Fe-4S] cluster and/or the siroheme due to the reorganization of microscopic structures.

Comparison of the detailed activity profiles obtained with the two distinct assays further conferred insight into the factors regulating total SiR activity. At 0-100 mM NaCl, while

in the Fd-dependent assay SiR exhibited dynamic activity changes, with maximal activity and catalytic efficiency around 40-70 mM NaCl and decreased activity at higher concentrations, activity in the MV-based assay increased in SiR activity before reaching a plateau (Fig. 4-1B). For example, a higher Fd-dependent SiR activity was measured at 50 mM NaCl than that at 100 mM NaCl despite intrinsic SiR activity at 50 mM NaCl actually being lower than at 100 mM NaCl. Moreover, although MV-based SiR activity retained maximum activity at higher NaCl concentrations over the saturation point of 100 mM NaCl, the Fd-based assay showed minimum activity due to significantly low interprotein affinity (Table 4-2) resulting from the attenuation of electrostatic interactions.

These findings indicated that maximum SiR activity at moderate concentrations of NaCl is achievable through optimum interactions between Fd and SiR and that intermolecular interaction is a more decisive factor in controlling SiR activity than intrinsic SiR catalytic capacity under physiological conditions (see the final section of **DISCUSSION**).

Intermolecular non-covalent forces thermodynamically control Fd:SiR complex formation

Interprotein interactions are under thermodynamic control, which tends to have a lower ΔG_{bind} by balancing the two driving forces, ΔH_{bind} and $(-T)\Delta S_{bind}$ (13,22,78). Therefore, I herein thermodynamically examined complex formation between Fd and SiR using ITC over variable NaCl because ITC reports driving forces which reflect electrostatic and non-electrostatic forces (13,16-18,22,44,45,78,79), which will be altered as NaCl influences the relative strength of interprotein attraction and interaction. Higher salt concentrations dampen electrostatic and polar interactions, but reinforce hydrophobic interactions.

I performed ITC measurements on addition of Fd to SiR at variable NaCl concentrations, which is a largely-used neutral salt that partly mimics local conditions in cells and chloroplasts (80-82). Energetically-favourable negative enthalpy changes were observed at all NaCl concentrations (Fig. 4-2A, B and Table 4-2); however, the plot of the driving forces (referred to hereafter as the driving force plot) showed that increasing the amount of NaCl attenuated interprotein affinity by decreasing the magnitude of enthalpy changes (Fig. 4-2C). These results suggest that attractive charge-charge and polar interactions as well as hydrophobic interactions positively contributed to complex formation with enthalpy as a driving force, and that weakened charge and polar interactions due to the disturbance of counter

ions or electrostatic screening were compensated by increased hydrophobic interactions.

Consequently, enthalpic gains from electrostatic and polar interactions were dominant over interactions among hydrophobic side chains under higher NaCl concentrations. On the other hand, electrostatic interactions enhance the molecular association rate through long-range electrostatic steering (43,46); therefore decreased affinity at high salt concentrations accounts for the decreased association rate (Fig. 4-7), stemming from the attenuation of electrostatic interactions.

As with NaCl concentration, increased temperature is generally followed by decreases and increases in electrostatic and hydrophobic forces, respectively (22,66). Thus, the heat capacity change for binding ($\Delta C_{p,bind}$), which is a temperature-dependent enthalpy change ($\Delta C_{p,bind} = \partial \Delta H_{bind}/\partial T$), is also an indicator for the contribution of non-covalent forces to complex formation based on the sign and magnitude of $\Delta C_{p,bind}$ (13,16,17,44,45,78,83,84). Most protein complex formation studied by ITC show a negative $\Delta C_{p,bind}$, indicating that the enthalpic contribution of hydrophobic interactions prevailed over electrostatic and/or polar interactions, even when interactions between oppositely-charged proteins appeared more obvious candidates, such as formation of the Fd:FNR complex ($\Delta C_{p,bind}$ = -100.4 cal mol^{-1} K^{-1}) (13), the Putidaredoxin (Pdx):putidaredoxin reductase (PdR) complex ($\Delta C_{p,bind}$ = -296.4 cal mol^{-1} K^{-1}) (40), and the P450cam:Pdx complex ($\Delta C_{p,bind}$ = -308.3 cal mol^{-1} K^{-1}) (40). Therefore, a negative $\Delta C_{p,bind}$ (-19.7 cal mol^{-1} K^{-1}) for formation of the Fd:SiR complex (Fig. 4-3B and Table 4-2) also demonstrated contributions from hydrophobic interactions. The small magnitude of $\Delta C_{p,bind}$ in the Fd:SiR complex compared to formation of other electron transfer complexes suggests a large contribution of charge-charge interactions, which increase $\Delta C_{p,bind}$ (13,44,78,83). These findings clearly demonstrate that non-electrostatic interactions were also important for Fd:SiR complex formation and that non-covalent forces thermodynamically withstand changes in salt concentration and temperature through energetic adaptation.

Entropy changes also drove complex formation, giving positive values at all NaCl concentrations (Fig. 4-2*B*), although entropy was not significantly affected by the NaCl concentration as shown in the driving force plot (Fig.4-2*C*). This indicates that entropy plays a key role in stabilizing the Fd:SiR complex as observed in forming the Fd:FNR complex (13) and that enthalpy is a more decisive factor than entropy in controlling the stability of the complex (i.e., affinity). Considering the surface areas buried on formation of the Fd:SiR

complex are similar regardless of the NaCl concentration, as elucidated by NMR (Fig. 6*B*), the energetic contribution of dehydration might be similar in formation of all Fd:SiR complexes although I cannot exclude the possibility of trapped water and salt ions in interface (44,85).

Accordingly, the physical binding reactions between oppositely-charged Fd and SiR are favored by both electrostatic and non-electrostatic interactions. Although other factors, including the behavior of water, ions, protons, and protein dynamics, probably also contribute, the thermodynamic balance for complex formation between enzymes and electron transfer partners, depending on conditions, can be explained through the general thermodynamic concept of enthalpy-entropy compensation.

Optimization of SiR activity by fine-tuning of the interprotein interaction with Fd under physiological conditions

Information about weak and strong intermolecular interactions obtained by NMR spectroscopy is extremely useful in evaluating the interacting site and binding mode of proteins in solution, which are otherwise difficult to detect at the residue level (22,60,86). The NMR-based infinite CSD analysis revealed no marked differences in the overall binding interfaces of Fd for SiR over the range of 0 to 100 mM NaCl; however, the relative contributions of each binding region and interacting residue to complex formation and modulation were different (Fig. 4-6B). The central regions in the primary sequence of Fd, centered on the [2Fe-2S] cluster, such as A28, E29, G32, D34, L35, Y37, and Y63, generally showed the strongest perturbation, regardless of the NaCl concentration, and high sequence conservation (Fig. 4-8), suggesting that these residues (hereafter called stabilizing residues) were the most fundamental residues for maintaining the complex state.

The decrease in the magnitude of CSD on both terminal parts such as E11 and E13 in the N-terminal part and K91, E92-E94, and T96 in the C-terminal part (designated regulating residues) correlated well with the decrease in affinity at higher NaCl concentrations. This reveals that the regulating residues play a more significant role in determining the interprotein affinity and binding mode. Negatively-charged residues in the C-terminal part were conserved in higher plants (Fig. 4-8). Stabilizing and regulating residues, which may be hot spot residues, were both composed of charged and non-charged residues, demonstrating that electrostatic and non-electrostatic interactions were essential for stabilizing complex and adjusting interprotein affinity, in good agreement with the thermodynamic analysis of ITC.

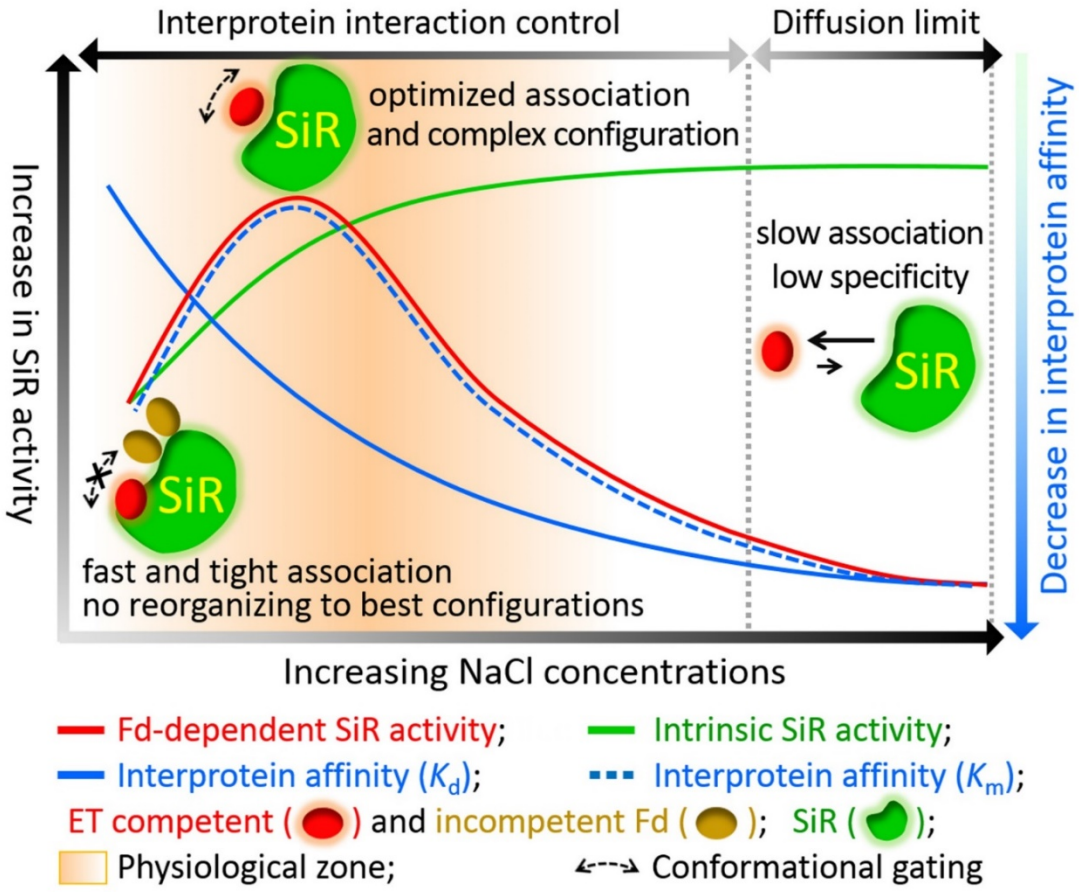

Fig 4-7. Overall scheme of relations between SiR activity and Fd:SiR interactions depending on variation in salt concentration.

Fd-dependent overall (red curve) and intrinsic SiR activity (green curve) are represented. The continuous and dotted blue curves indicate trends of the change in interprotein affinity revealed by ITC (K_d) and Michaelis-Menten kinetics (K_m), respectively. Electron transfer (ET) competent and incompetent Fds are represented by red and deep yellow objects, respectively. SiR is schematically shown in green. While conformational gating (dotted curve with double arrows) for efficient electron transfer with structural rearrangement to best configuration is allowable at the moderate NaCl concentration, gating is blocked by strong intramolecular forces in the complex.

Interestingly, the direction of peak shift for S59 and D60 (Fig. 4-5C) in the presence of SiR varied with NaCl concentration, while the other peaks, such as E92, were shifted to the same direction (Fig. 4-5A, inset). This indicates that a region including S59 and D60 is involved in distinct binding modes depending on the NaCl concentration. Thus, the bell-shaped activity curve of SiR can be also mechanically explained by a change in the binding mode between Fd and SiR (i.e., structural rearrangement), which was further supported by PCA (Fig. 4-5F).

Taken together, a bell-shaped profile of Fd-dependent SiR activity was demonstrated, based on the affinity and binding mode (Fig. 4-7). At low and moderate NaCl concentrations which are near physiological conditions in plant chloroplasts (ionic strength of ~0.1-0.15 M) (Fig. 4-7, middle), delicate interprotein regulation optimizes SiR activity. Stabilizing residues form initial complexes, followed by tuning into a productive complex with the best configuration for conformational gating (53) by regulating residues with non-covalent interactions. This fine tuning model rationalizes the discrepancy among the apparently continuous increases in K_d observed in the ITC results, the bell-shaped activity curves with a maximum at around 40-70 mM NaCl in 50 mM Tris-HCl buffer, and a reverse bell-shaped dependence of the Michaelis constant. At higher NaCl concentrations (Fig. 4-7, right), collision and diffusion may limit the formation of the stable electron-transfer competent complex and decrease the possibility of formation of productive complexes due to geometric constraints of the binding sites (46). In the absence of NaCl, relatively efficient-complexes can form at the high affinity binding sites on SiR, but also non-productive complex can form at the low affinity binding sites (Table 4-2), preventing maximum activity (Fig. 4-7, left).

Thus, increasing and decreasing affinity beyond well-controlled interprotein forces may not allow maximum enzymatic activity in terms of kinetics and thermodynamics. Too strong an affinity due to the fast association of reduced Fd and/or the slow dissociation of oxidized Fd in the absence of salts may decrease turnover numbers, and block diffusion from non- or moderately-productive complex to the best configuration (43,46). Meanwhile, too weak an affinity is also not adequate for enzymatic function. Although the roles of water molecules are not addressed herein, interfacial water plays a marked thermodynamic and kinetic role in stabilizing the protein complex and in controlling configuration (84,85,87).

Changing physiological electron donor or acceptor proteins to proteins of distinct species or other redox proteins abolishes a bell-shaped electron transfer rate as observed in the

Fd:NiR (14), Fd:FNR (71), and Cyt*c*:C*c*P/PC systems (73) possibly owing to subtle changes in binding modes. Optimized enzymatic activity near physiological conditions is ensured by the appropriate interplay between the physical, kinetic, and energetic adjustments on complex formation by evolution.

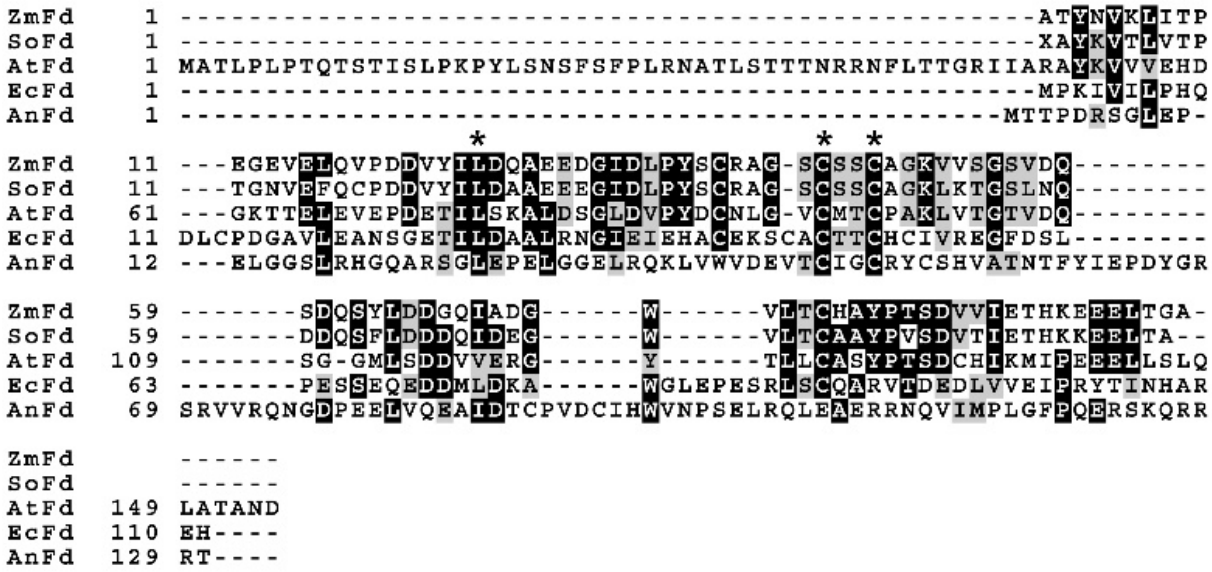

Fig 4-8. Multiple sequence alignments of Fds.

Amino acid sequences of Fds from plant, *E. coli*, and cyanobacterium are compared. The sequences of Fds from maize (ZmFd), spinach (SoFd), *Arabidopsis thaliana* (AtFd), *Synechococcus* PCC7942 (AnFd), and *E. coli* (EcFd) are aligned with gaps inserted to obtain the homology. Color codes are black for conservation and gray for semi-conservation. Asterisks indicate that the residues in that column are identical in all sequences in the alignment.

Chapter V

General conclusion

General conclusion

I have performed the in-depth study on the interprotein interactions between Fd and SiR and their relations to SiR activity by combining various biochemical and biophysical approaches. By analyzing the crystal structures of the Fd:SiR complexes, I demonstrated that interfaces of the complex consisted of electrostatic networks with non-electrostatic interactions, and that similar but different binding modes between two proteins are possible depending on different solvent conditions. Although disruption of interfacial electrostatic interactions lowered significantly SiR activity due to the loss of ability of the complex formation, that of non-electrostatic interactions such as hydrophobic interactions at interfaces showed substrate preference without affecting the formation of the Fd:SiR complex probably due to subtle changes in configuration of the complex. Changing the concentration of salts revealed that small changes in configuration of the Fd:SiR complex control thermodynamically and mechanically Fd-dependent SiR activity through non-covalent forces.

Taken all together, I suggest that overall SiR activity depends on the intermolecular interactions with Fd and both non-covalent interactions, electrostatic- and non-electrostatic interactions, play an individual roles in controlling SiR activity in response to the change in environmental changes. It may be conceivable that enzymes have been evolved to adapt themselves to ambient conditions in order to maximize biological efficiency.

For the further understanding on the relation between interprotein interactions and SiR activity, the same experiment and analyses conducted in this study could be performed in the distinct redox states. In addition, direct determination of the crystal structures of the complex of mutant SiRs with Fd as well as the assignment of isotope-labeled SiR for solution-state NMR spectroscopy will be promising. Other NMR techniques such as residual dipolar coupling measurements which provide the relative orientation of Fd and SiR in the complex can provide detailed information on the subtle changes in configuration of the Fd:SiR complex under various conditions. Examination on the intermolecular interaction between SiR and its substrates using NMR and ITC will be interesting and the measurement of the electron transfer rate using laser photolysis

with a set of SiR activity assays will be also helpful. Finally, the comparative study with the formation of the Fd:FNR complex and FNR activity will be an interesting subject.

References

1. Leustek, T., and Saito, K. (1999) Sulfate transport and assimilation in plants. *Plant physiology* **120**, 637-644
2. Akashi, T., Matsumura, T., Ideguchi, T., Iwakiri, K., Kawakatsu, T., Taniguchi, I., and Hase, T. (1999) Comparison of the electrostatic binding sites on the surface of ferredoxin for two ferredoxin-dependent enzymes, ferredoxin-NADP(+) reductase and sulfite reductase. *J Biol Chem* **274**, 29399-29405
3. Nakayama, M., Akashi, T., and Hase, T. (2000) Plant sulfite reductase: molecular structure, catalytic function and interaction with ferredoxin. *J Inorg Biochem* **82**, 27-32
4. Saitoh, T., Ikegami, T., Nakayama, M., Teshima, K., Akutsu, H., and Hase, T. (2006) NMR study of the electron transfer complex of plant ferredoxin and sulfite reductase: mapping the interaction sites of ferredoxin. *J Biol Chem* **281**, 10482-10488
5. Janick, P. A., and Siegel, L. M. (1982) Electron paramagnetic resonance and optical spectroscopic evidence for interaction between siroheme and Fe4S4 prosthetic groups in Escherichia coli sulfite reductase hemoprotein subunit. *Biochemistry* **21**, 3538-3547
6. Yonekura-Sakakibara, K., Onda, Y., Ashikari, T., Tanaka, Y., Kusumi, T., and Hase, T. (2000) Analysis of reductant supply systems for ferredoxin-dependent sulfite reductase in photosynthetic and nonphotosynthetic organs of maize. *Plant physiology* **122**, 887-894
7. Brunold, C., and Suter, M. (1989) Localization of enzymes of assimilatory sulfate reduction in pea roots. *Planta* **179**, 228-234
8. Bork, C., Schwenn, J. D., and Hell, R. (1998) Isolation and characterization of a gene for assimilatory sulfite reductase from Arabidopsis thaliana. *Gene* **212**, 147-153
9. Yonekura-Sakakibara, K., Ashikari, T., Tanaka, Y., Kusumi, T., and Hase, T. (1998) Molecular characterization of tobacco sulfite reductase: enzyme purification, gene cloning, and gene expression analysis. *J Biochem* **124**, 615-621

10. Bowsher, C. G., Hucklesby, D. P., and Emes, M. J. (1989) Nitrite reduction and carbohydrate metabolism in plastids purified from roots of Pisum sativum L. *Planta* **177**, 359-366
11. Kurisu, G., Kusunoki, M., Katoh, E., Yamazaki, T., Teshima, K., Onda, Y., Kimata-Ariga, Y., and Hase, T. (2001) Structure of the electron transfer complex between ferredoxin and ferredoxin-NADP(+) reductase. *Nat Struct Biol* **8**, 117-121
12. Lee, Y. H., Chatani, E., Sasahara, K., Naiki, H., and Goto, Y. (2009) A comprehensive model for packing and hydration for amyloid fibrils of beta2-microglobulin. *J Biol Chem* **284**, 2169-2175
13. Lee, Y. H., Ikegami, T., Standley, D. M., Sakurai, K., Hase, T., and Goto, Y. (2011) Binding energetics of ferredoxin-NADP+ reductase with ferredoxin and its relation to function. *Chembiochem* **12**, 2062-2070
14. Sakakibara, Y., Kimura, H., Iwamura, A., Saitoh, T., Ikegami, T., Kurisu, G., and Hase, T. (2012) A new structural insight into differential interaction of cyanobacterial and plant ferredoxins with nitrite reductase as revealed by NMR and X-ray crystallographic studies. *J Biochem* **151**, 483-492
15. Hirasawa, M., Nakayama, M., Kim, S. K., Hase, T., and Knaff, D. B. (2005) Chemical modification studies of tryptophan, arginine and lysine residues in maize chloroplast ferredoxin:sulfite oxidoreductase. *Photosynthesis research* **86**, 325-336
16. Jelesarov, I., and Bosshard, H. R. (1999) Isothermal titration calorimetry and differential scanning calorimetry as complementary tools to investigate the energetics of biomolecular recognition. *J Mol Recognit* **12**, 3-18
17. Pierce, M. M., Raman, C. S., and Nall, B. T. (1999) Isothermal titration calorimetry of protein-protein interactions. *Methods* **19**, 213-221
18. Velazquez Campoy, A., and Freire, E. (2005) ITC in the post-genomic era...? Priceless. *Biophys Chem* **115**, 115-124
19. Ladbury, J. E. (2007) Measurement of the formation of complexes in tyrosine kinase-mediated signal transduction. *Acta Crystallogr D Biol Crystallogr* **63**, 26-31
20. Privalov, P. L., Dragan, A. I., Crane-Robinson, C., Breslauer, K. J., Remeta, D. P., and Minetti, C. A. (2007) What drives proteins into the major or minor grooves of DNA? *J Mol Biol* **365**, 1-9

21. Ladbury, J. E. (2010) Calorimetry as a tool for understanding biomolecular interactions and an aid to drug design. *Biochem Soc Trans* **38**, 888-893
22. Kinoshita, M., Kim, J. Y., Kume, S., Sakakibara, Y., Sugiki, T., Kojima, C., Kurisu, G., Ikegami, T., Hase, T., Kimata-Ariga, Y., and Lee, Y. H. (2015) Physicochemical nature of interfaces controlling ferredoxin NADP(+) reductase activity through its interprotein interactions with ferredoxin. *Biochim Biophys Acta* **1847**, 1200-1211
23. Wodak, S. J., and Janin, J. (2002) Protein Modules and Protein-Protein Interaction. *Advances in Protein Chemistry* **61**, 21-23
24. Galperin, M. Y., and Koonin, E. V. (2012) Divergence and convergence in enzyme evolution. *J Biol Chem* **287**, 21-28
25. Knaff, D. B., and Hirasawa, M. (1991) Ferredoxin-dependent chloroplast enzymes. *Biochim Biophys Acta* **1056**, 93-125
26. Hurley, J. K., Salamon, Z., Meyer, T. E., Fitch, J. C., Cusanovich, M. A., Markley, J. L., Cheng, H., Xia, B., Chae, Y. K., Medina, M., and et al. (1993) Amino acid residues in Anabaena ferredoxin crucial to interaction with ferredoxin-NADP+ reductase: site-directed mutagenesis and laser flash photolysis. *Biochemistry* **32**, 9346-9354
27. Hurley, J. K., Faro, M., Brodie, T. B., Hazzard, J. T., Medina, M., Gomez-Moreno, C., and Tollin, G. (2000) Highly nonproductive complexes with Anabaena ferredoxin at low ionic strength are induced by nonconservative amino acid substitutions at Glu139 in Anabaena ferredoxin:NADP+ reductase. *Biochemistry* **39**, 13695-13702
28. Martinez-Julvez, M., Nogues, I., Faro, M., Hurley, J. K., Brodie, T. B., Mayoral, T., Sanz-Aparicio, J., Hermoso, J. A., Stankovich, M. T., Medina, M., Tollin, G., and Gomez-Moreno, C. (2001) Role of a cluster of hydrophobic residues near the FAD cofactor in Anabaena PCC 7119 ferredoxin-NADP+ reductase for optimal complex formation and electron transfer to ferredoxin. *J Biol Chem* **276**, 27498-27510
29. Gross, E. L., and Pearson, D. C., Jr. (2003) Brownian dynamics simulations of the interaction of Chlamydomonas cytochrome f with plastocyanin and cytochrome c6. *Biophysical journal* **85**, 2055-2068
30. Nogues, I., Martinez-Julvez, M., Navarro, J. A., Hervas, M., Armenteros, L., de la

Rosa, M. A., Brodie, T. B., Hurley, J. K., Tollin, G., Gomez-Moreno, C., and Medina, M. (2003) Role of hydrophobic interactions in the flavodoxin mediated electron transfer from photosystem I to ferredoxin-NADP+ reductase in Anabaena PCC 7119. *Biochemistry* **42**, 2036-2045

31. Maneg, O., Malatesta, F., Ludwig, B., and Drosou, V. (2004) Interaction of cytochrome c with cytochrome oxidase: two different docking scenarios. *Biochim Biophys Acta* **1655**, 274-281
32. Nogues, I., Hervas, M., Peregrina, J. R., Navarro, J. A., de la Rosa, M. A., Gomez-Moreno, C., and Medina, M. (2005) Anabaena flavodoxin as an electron carrier from photosystem I to ferredoxin-NADP+ reductase. Role of flavodoxin residues in protein-protein interaction and electron transfer. *Biochemistry* **44**, 97-104
33. Hulsker, R., Baranova, M. V., Bullerjahn, G. S., and Ubbink, M. (2008) Dynamics in the transient complex of plastocyanin-cytochrome f from Prochlorothrix hollandica. *Journal of the American Chemical Society* **130**, 1985-1991
34. Volkov, A. N., Ubbink, M., and van Nuland, N. A. (2010) Mapping the encounter state of a transient protein complex by PRE NMR spectroscopy. *J Biomol NMR* **48**, 225-236
35. Ubbink, M. (2012) Dynamics in transient complexes of redox proteins. *Biochem Soc Trans* **40**, 415-418
36. Bashir, Q., Volkov, A. N., Ullmann, G. M., and Ubbink, M. (2010) Visualization of the encounter ensemble of the transient electron transfer complex of cytochrome c and cytochrome c peroxidase. *Journal of the American Chemical Society* **132**, 241-247
37. Bashir, Q., Scanu, S., and Ubbink, M. (2011) Dynamics in electron transfer protein complexes. *FEBS J* **278**, 1391-1400
38. Scanu, S., Foerster, J. M., Timmer, M., Ullmann, G. M., and Ubbink, M. (2013) Loss of electrostatic interactions causes increase of dynamics within the plastocyanin-cytochrome f complex. *Biochemistry* **52**, 6615-6626
39. Schilder, J., and Ubbink, M. (2013) Formation of transient protein complexes. *Curr Opin Struct Biol* **23**, 911-918
40. Aoki, M., Ishimori, K., Fukada, H., Takahashi, K., and Morishima, I. (1998)

Isothermal titration calorimetric studies on the associations of putidaredoxin to NADH-putidaredoxin reductase and P450cam. *Biochim Biophys Acta* **1384**, 180-188

41. Ideguchi, T., Akashi, T., Onda, Y., and Hase, T. (1995) cDNA cloning and functional expression of ferredoxin-dependent sulfite reductase from maize in *E.coli* cells in *Photosynthesis: from light to biosphere* (Mathis, P., ed.). Vol. 2, pp. 713-716, Kluwer Academic Publishers, the Netherlands
42. Matsumura, T., Kimata-Ariga, Y., Sakakibara, H., Sugiyama, T., Murata, H., Takao, T., Shimonishi, Y., and Hase, T. (1999) Complementary DNA cloning and characterization of ferredoxin localized in bundle-sheath cells of maize leaves. *Plant physiology* **119**, 481-488
43. Hope, A. B. (2000) Electron transfers amongst cytochrome f, plastocyanin and photosystem I: kinetics and mechanisms. *Biochim Biophys Acta* **1456**, 5-26
44. Ladbury, J. E., and Williams, M. A. (2004) The extended interface: measuring non-local effects in biomolecular interactions. *Curr Opin Struct Biol* **14**, 562-569
45. Leavitt, S., and Freire, E. (2001) Direct measurement of protein binding energetics by isothermal titration calorimetry. *Curr Opin Struct Biol* **11**, 560-566
46. Schreiber, G. (2002) Kinetic studies of protein-protein interactions. *Curr Opin Struct Biol* **12**, 41-47
47. Sheinerman, F. B., Norel, R., and Honig, B. (2000) Electrostatic aspects of protein-protein interactions. *Curr Opin Struct Biol* **10**, 153-159
48. Delaglio, F., Grzesiek, S., Vuister, G. W., Zhu, G., Pfeifer, J., and Bax, A. (1995) NMRPipe: a multidimensional spectral processing system based on UNIX pipes. *J Biomol NMR* **6**, 277-293
49. Lee, W., Tonelli, M., and Markley, J. L. (2015) NMRFAM-SPARKY: enhanced software for biomolecular NMR spectroscopy. *Bioinformatics* **31**, 1325-1327
50. Winkler, M., Kuhlgert, S., Hippler, M., and Happe, T. (2009) Characterization of the key step for light-driven hydrogen evolution in green algae. *J Biol Chem* **284**, 36620-36627
51. Karplus, P. A., Daniels, M. J., and Herriott, J. R. (1991) Atomic structure of ferredoxin-NADP+ reductase: prototype for a structurally novel flavoenzyme

family. *Science* **251**, 60-66

52. Krueger, R. J., and Siegel, L. M. (1982) Spinach siroheme enzymes: Isolation and characterization of ferredoxin-sulfite reductase and comparison of properties with ferredoxin-nitrite reductase. *Biochemistry* **21**, 2892-2904
53. Jeuken, L. J. (2003) Conformational reorganisation in interfacial protein electron transfer. *Biochim Biophys Acta* **1604**, 67-76
54. Mulo, P. (2011) Chloroplast-targeted ferredoxin-NADP(+) oxidoreductase (FNR): structure, function and location. *Biochim Biophys Acta* **1807**, 927-934
55. Pey, A. L. (2013) Protein homeostasis disorders of key enzymes of amino acids metabolism: mutation-induced protein kinetic destabilization and new therapeutic strategies. *Amino Acids* **45**, 1331-1341
56. Srivastava, A. P., Hirasawa, M., Bhalla, M., Chung, J. S., Allen, J. P., Johnson, M. K., Tripathy, J. N., Rubio, L. M., Vaccaro, B., Subramanian, S., Flores, E., Zabet-Moghaddam, M., Stitle, K., and Knaff, D. B. (2013) Roles of four conserved basic amino acids in a ferredoxin-dependent cyanobacterial nitrate reductase. *Biochemistry* **52**, 4343-4353
57. Goss, T., and Hanke, G. (2014) The end of the line: can ferredoxin and ferredoxin NADP(H) oxidoreductase determine the fate of photosynthetic electrons? *Curr Protein Pept Sci* **15**, 385-393
58. Kume, S., Lee, Y. H., Nakatsuji, M., Teraoka, Y., Yamaguchi, K., Goto, Y., and Inui, T. (2014) Fine-tuned broad binding capability of human lipocalin-type prostaglandin D synthase for various small lipophilic ligands. *FEBS Lett* **588**, 962-969
59. Baldwin, R. L. (2007) Energetics of protein folding. *J Mol Biol* **371**, 283-301
60. Bah, A., Vernon, R. M., Siddiqui, Z., Krzeminski, M., Muhandiram, R., Zhao, C., Sonenberg, N., Kay, L. E., and Forman-Kay, J. D. (2015) Folding of an intrinsically disordered protein by phosphorylation as a regulatory switch. *Nature* **519**, 106-109
61. Todd, A. E., Orengo, C. A., and Thornton, J. M. (2002) Plasticity of enzyme active sites. *Trends Biochem Sci* **27**, 419-426
62. Daniel, R. M., Dunn, R. V., Finney, J. L., and Smith, J. C. (2003) The role of dynamics in enzyme activity. *Annu Rev Biophys Biomol Struct* **32**, 69-92

63. DuBay, K. H., Bowman, G. R., and Geissler, P. L. (2015) Fluctuations within folded proteins: implications for thermodynamic and allosteric regulation. *Acc Chem Res* **48**, 1098-1105
64. Lin, Z., Schwartz, F. P., and Eisenstein, E. (1995) The hydrophobic nature of GroEL-substrate binding. *J Biol Chem* **270**, 1011-1014
65. Kay, B. K., Williamson, M. P., and Sudol, M. (2000) The importance of being proline: the interaction of proline-rich motifs in signaling proteins with their cognate domains. *FASEB J* **14**, 231-241
66. Ikenoue, T., Lee, Y. H., Kardos, J., Saiki, M., Yagi, H., Kawata, Y., and Goto, Y. (2014) Cold denaturation of alpha-synuclein amyloid fibrils. *Angew Chem Int Ed Engl* **53**, 7799-7804
67. Zhen, Y., Hoganson, C. W., Babcock, G. T., and Ferguson-Miller, S. (1999) Definition of the interaction domain for cytochrome c on cytochrome c oxidase. I. Biochemical, spectral, and kinetic characterization of surface mutants in subunit ii of Rhodobacter sphaeroides cytochrome aa(3). *J Biol Chem* **274**, 38032-38041
68. Hazzard, J. T., Rong, S. Y., and Tollin, G. (1991) Ionic strength dependence of the kinetics of electron transfer from bovine mitochondrial cytochrome c to bovine cytochrome c oxidase. *Biochemistry* **30**, 213-222
69. Hirota, S., and Yamauchi, O. (2001) Weak interactions and molecular recognition in systems involving electron transfer proteins. *Chem Rec* **1**, 290-299
70. Soriano, G. M., Ponamarev, M. V., Piskorowski, R. A., and Cramer, W. A. (1998) Identification of the basic residues of cytochrome f responsible for electrostatic docking interactions with plastocyanin in vitro: relevance to the electron transfer reaction in vivo. *Biochemistry* **37**, 15120-15128
71. Hurley, J. K., Schmeits, J. L., Genzor, C., Gomez-Moreno, C., and Tollin, G. (1996) Charge reversal mutations in a conserved acidic patch in Anabaena ferredoxin can attenuate or enhance electron transfer to ferredoxin:NADP+ reductase by altering protein/protein orientation within the intermediate complex. *Arch Biochem Biophys* **333**, 243-250
72. Meyer, T. E., Zhao, Z. G., Cusanovich, M. A., and Tollin, G. (1993) Transient kinetics of electron transfer from a variety of c-type cytochromes to plastocyanin.

Biochemistry **32**, 4552-4559

73. Tollin, G., Hurley, J. K., Hazzard, J. T., and Meyer, T. E. (1993) Use of laser flash photolysis time-resolved spectrophotometry to investigate interprotein and intraprotein electron transfer mechanisms. *Biophys Chem* **48**, 259-279
74. Cruz-Gallardo, I., Diaz-Moreno, I., Diaz-Quintana, A., and De la Rosa, M. A. (2012) The cytochrome f-plastocyanin complex as a model to study transient interactions between redox proteins. *FEBS Lett* **586**, 646-652
75. Scanu, S., Foerster, J. M., Ullmann, G. M., and Ubbink, M. (2013) Role of hydrophobic interactions in the encounter complex formation of the plastocyanin and cytochrome f complex revealed by paramagnetic NMR spectroscopy. *Journal of the American Chemical Society* **135**, 7681-7692
76. Acheson, J. F., Bailey, L. J., Elsen, N. L., and Fox, B. G. (2014) Structural basis for biomolecular recognition in overlapping binding sites in a diiron enzyme system. *Nat Commun* **5**, 5009
77. Akagi, K., Watanabe, J., Hara, M., Kezuka, Y., Chikaishi, E., Yamaguchi, T., Akutsu, H., Nonaka, T., Watanabe, T., and Ikegami, T. (2006) Identification of the substrate interaction region of the chitin-binding domain of Streptomyces griseus chitinase C. *J Biochem* **139**, 483-493
78. Olsson, T. S., Williams, M. A., Pitt, W. R., and Ladbury, J. E. (2008) The thermodynamics of protein-ligand interaction and solvation: insights for ligand design. *J Mol Biol* **384**, 1002-1017
79. Ladbury, J. E., Klebe, G., and Freire, E. (2010) Adding calorimetric data to decision making in lead discovery: a hot tip. *Nat Rev Drug Discov* **9**, 23-27
80. Robinson, S. P., and Downton, W. J. (1984) Potassium, sodium, and chloride content of isolated intact chloroplasts in relation to ionic compartmentation in leaves. *Arch Biochem Biophys* **228**, 197-206
81. Schroppel-Meier, G., and Kaiser, W. M. (1988) Ion Homeostasis in Chloroplasts under Salinity and Mineral Deficiency : I. Solute Concentrations in Leaves and Chloroplasts from Spinach Plants under NaCl or NaNO(3) Salinity. *Plant physiology* **87**, 822-827
82. Soriano, G. M., Ponamarev, M. V., Tae, G. S., and Cramer, W. A. (1996) Effect of

the interdomain basic region of cytochrome f on its redox reactions in vivo. *Biochemistry* **35**, 14590-14598

83. Loladze, V. V., Ermolenko, D. N., and Makhatadze, G. I. (2001) Heat capacity changes upon burial of polar and nonpolar groups in proteins. *Protein Sci* **10**, 1343-1352
84. Nilapwar, S., Williams, E., Fu, C., Prodromou, C., Pearl, L. H., Williams, M. A., and Ladbury, J. E. (2009) Structural-thermodynamic relationships of interactions in the N-terminal ATP-binding domain of Hsp90. *J Mol Biol* **392**, 923-936
85. Bergqvist, S., Williams, M. A., O'Brien, R., and Ladbury, J. E. (2004) Heat capacity effects of water molecules and ions at a protein-DNA interface. *J Mol Biol* **336**, 829-842
86. Mizushima, R., Kim, J. Y., Suetake, I., Tanaka, H., Takai, T., Kamiya, N., Takano, Y., Mishima, Y., Tajima, S., Goto, Y., Fukui, K., and Lee, Y. H. (2014) NMR characterization of the interaction of the endonuclease domain of MutL with divalent metal ions and ATP. *PLoS One* **9**, e98554
87. Furukawa, Y., and Morishima, I. (2001) The role of water molecules in the association of cytochrome P450cam with putidaredoxin. An osmotic pressure study. *J Biol Chem* **276**, 12983-12990